GEOMETRY, KINEMATICS, EXHUMATION, AND SEDIMENTATION OF THE NORTHERN BOLIVIAN FOLD-THRUST-BELT-FORELAND BASIN SYSTEM.

by

Adam James Rak

B.S. Geology, Slippery Rock University, 2012

Submitted to the Graduate Faculty of the

Kenneth P. Dietrich School of Arts and Sciences in partial fulfillment

of the requirements for the degree of

Master of Science in Geology

University of Pittsburgh

2015

UNIVERSITY OF PITTSBURGH

KENNETH P. DIETRICH SCHOOL OF ARTS AND SCIENCES

This thesis was presented

by

Adam James Rak

It was defended on

May 28, 2015

and approved by

William Harbert, Professor, Department of Geology & Planetary Science

Josef Werne, Associate Professor, Department of Geology & Planetary Science

Thesis Advisor: Nadine McQuarrie, Assistant Professor, Department of Geology & Planetary Science

GEOMETRY, KINEMATICS, EXHUMATION, AND SEDIMENTATION OF THE NORTHERN BOLIVIAN FOLD-THRUST-BELT-FORELAND BASIN SYSTEM.

Adam James Rak, M.S.

University of Pittsburgh, 2015

Abstract

Geometry and kinematics of deformation in the northern Bolivian Andes determine geologic map patterns, thermochronometer cooling signals, and synorogenic sediment distribution within the linked fold-thrust-belt-foreland basin system. To analyze the geometry, timing and rates of deformation we present a new cross section in northern Bolivia (Copacabana cross section) and perform thermokinematic modeling on a previously published, adjacent cross section (Beni cross section). Isostasy and erosion are applied to the sequentially deformed Beni cross section in northern Bolivia (McQuarrie et al., 2008) with kinematic modeling software *Move*. Applying isostasy and erosion to sequentially deformed balanced cross sections links the growth of hinterland structures to the developing foreland basins (FB) adjacent to fold-thrust belts (FTB), adding additional geologic constraints to modeled exhumation pathways. In our model, topography evolves and basins develop for each model step as deformation, erosion, and isostasy are applied; and are a direct function of the geometry and kinematics of the cross section. The model is constrained by the depth of the foreland and hinterland basins, geology at the surface, the depth and angle of the decollement, and the shape of the modern observed topography. Topography develops as thrusting occurs and loads the crust, producing a flexural wave and creating accommodation space in adjacent basins. Erosion of material above a newly generated topographic profile unloads the section while basin space is filled. Once the model

sufficiently duplicates geologic constraints, a grid of unique points is deformed with the model and used to determine displacement vectors for each 10 km shortening step. Displacement vectors, in conjunction with a prescribed time interval for each step, determine a velocity field that can be used in a modified version of the advection diffusion modeling software *Pecube*. Thermochronometer cooling ages predicted using this method are based on deformation rates, geometry, topography, and thermal parameters, and offer insight into possible rates of deformation, erosion, and deposition throughout FTB and FB development. Incorporating erosion, deposition, and isostasy in sequentially deformed balanced cross sections highlights the spatiotemporal aspects of sedimentary wedge propagation, identifies external negative buoyancy affects, and provides additional geologic constraints to modeled exhumation pathways.

TABLE OF CONTENTS

LIST OF TABLES

LIST OF FIGURES

PREFACE

Funding for this project was provided by the National Science Foundation (NSF grant EAR-0908972 to McQuarrie). This research was made possible by the support of many people in the University of Pittsburgh, the University of Tübigingen and beyond. I thank Susan Beck, George Zandt, Nadine McQuarrie, Brian Horton, Todd Ehlers, Chris Poulsen, Carmala Garzione, Laura Wagner, and their respective lab groups for information shared at the NSF funded Central Andean Geodynamics and High Topography (CAUGHT) workshop held at Arizona State University in 2013. I would like to express my gratitude to Kevin Ward for specific cross sections through the shear velocity model (Ward et al., 2013) along the trend of the Copacabana cross section presented in this manuscript. Methods and thermal parameter for thermokinematic modeling in *Pecube* were facilitated by Todd Ehlers with essential computer services provided by Willi Keppler at the University of Tübingen, Germany. I thank Nathan Eichelberger for the explanation of the remote dip *Matlab* script and insightful discussions. I would like to express gratitude to Nicholas Perez for enlightening discussions related to southern Peruvian Andes structural and sedimentary evolution.

I would like to thank the professors and staff at Slippery Rock University of Pennsylvania, especially Patricia Campbell, for the geologic knowledge and inspiration to follow my academic aspirations. The support and tolerance shown by my friends and family, especially my daughter Lola Rak, strengthened my conviction to complete this research. I would like to

thank Hannah Smith for conversations, dinners, espresso and support throughout this process that helped me to balancing time with my family and friends with the research conducted.

I thank the University of Pittsburgh, the Kenneth P. Dietrich School of Arts and Sciences and Department of Geology and Planetary Science for the support of geologic research, teaching, and the opportunity to conduct this study. I express gratitude to the tectonics lab group members at the University of Pittsburgh for perceptive discussions and guidance, including; Michelle Gilmore, Ashley Ace, Nathaniel Bootes, and Jessica DePaolis. I would like to thank my committee, William Harbert and Joseph Werne, for insightful comments and my advisor Nadine McQuarrie for thorough reviews of this manuscript. Above all, this project would not have been possible without the knowledge, discussions, cooperation, methodologies and critiques offered by my advisor Nadine McQuarrie. I would like to personally thank everyone that made this northern Bolivian Andes research possible and hope this helps define the evolution of the orogen and push mountain belt modeling forward.

This research focuses on thermochronometry of a variety of different mineral systems. Thermochronometry is an isotopic age dating method that dates the age at which a given mineral cooled below the temperature necessary for it to record the isotopic decay of elements (He, Ar, etc). Below this temperature, the mineral preserves the decayed daughter products and the magnitude of the daughter products preserved in the sample gives us the age that the sample passed through its unique isotherm. Sediment geochronology is used to describe isotopically dated samples collected from synorogenic rocks. Regions of the mountain range are described as the hinterland, if they are located in the core of the mountain belt, or the foreland, if they are located on the continental side of the mountain belt. Thermokinematic modeling describes a method of thermal modeling that applies the unique motion of material through the modeled

space. Thermochronometric modeling refers to a modeling technique that attempts to predict cooling of thermochronometer samples to constrain the timing of events.

1.0 INTRODUCTION

1.1 TIMING AND RATES OF DEFORMATION

The Central Andean Cordillera is the modern archetype of a retroarc fold-thrust-belt-foreland basin system resulting from strain accumulated due to the westward motion of the South American plate over the subducting Nazca plate (Jordan, 1995; DeCelles, 2012; Allmendinger et al., 1997). Interest in the geodynamic evolution of fold-thrust-belt-foreland basin systems stem from their intrinsic relationships with lithospheric deformation, crustal rigidity, convergent plate margin evolution, foreland basin hydrocarbon deposits, and high topography that may influence atmospheric circulation and precipitation (Jordan, 1981; Coney and Evenchick, 1994; Stockmal et al., 2007; Banes and Ehlers, 2009; Yan et al., 2010; DeCelles, 2012; Mount, 2014). The distribution of sediment in the hinterland and foreland basins of the Bolivian Andes is controlled by the spatiotemporal evolution of deformation in the Andean fold-thrust belt (FTB) (Horton and DeCelles, 2003; McQuarrie et al., 2005). While many studies attempt to quantify the age of initiation, magnitude of deformation and rate of shortening, values are still contested (Allmendinger et al., 1997; Horton et al., 2001; McQuarrie et al., 2005; Oncken et al., 2006; Gillis et al., 2006; McQuarrie et al., 2008).

Temporal aspects of deformation have been inferred through geochronology and provenance analyses of foreland basin and wedge-top sediment, and bedrock thermochronometer cooling signals. Traditionally, synorogenic sediment geochronology has been used to interpret the initiation of deformation in the Bolivian FTB. Initial studies proposed the original pulse of deformation in the FTB occurred in the Oligocene (38-25 Ma) based on the age of synorogenic wedge-top sedimentary rocks and cooling recorded in Triassic age plutons (Farrar et al., 1988; Sempere, 1990; Allmendinger et al., 1997; Jordan et al., 1997). However, Maastrichtian through Eocene sedimentary rocks preserved in the Bolivian Altiplano have been interpreted as backbulge and forebulge deposits, and used to argue for initial deformation in westernmost Bolivia in the late Cretaceous (Coney and Evenchick, 1994; Horton and DeCelles, 2003). In addition, recent thermochronometer analysis of K-feldspar (K-Feld), zircon fission track (ZFT), and apatite fission track (AFT) systems from the Triassic age plutons indicate rapid cooling occurred in the Eocene (45-40 Ma) with a lull in cooling in the late Oligocene early Miocene (25-11 Ma) and a second phase of cooling from 11 Ma onwards (Benjamin et al., 1987; Gillis et al., 2006). These data have been use to argue for early Eocene deformation-induced exhumation (Benjamin et al., 1987; Gillis et al., 2006; McQuarrie et al., 2008; Barnes et al., 2012).

Rates of deformation are dependent upon when deformation initiates as well as shortening magnitude. Magnitudes of total shortening determined through balanced cross section analyses of the central Andean FTB range from ~200-500 km (Sheffels, 1990; Kley, 1996; Baby et al., 1997, McQuarrie, 2002; McQuarrie et al., 2008, 2005; Gotberg et al., 2010; Eichelberger and McQuarrie, 2015). Early cross sections of the Bolivian Andes indicated low amounts of total shortening (<200 km) while more recent cross sections include detailed mapping of the hinterland of the FTB and consistently interpret high (>300 km) magnitudes of shortening

(McQuarrie, 2002; McQuarrie et al., 2008; Muller et al., 2002; Eichelberger et al., 2013). While total amount of shortening and age of initial deformation provide a long term rate of shortening, it is also likely that the rate of shortening through the central Andes has varied with time (Echavarria et al., 2003; McQuarrie et al., 2005; McQuarrie et al., 2008; Oncken et al., 2006). The large discrepancies in proposed age and rate of deformation prevent the accurate characterization of the shortening history of this type-example, retroarc fold-thrust-belt-foreland basin system, or relating that shortening history to internal or external forcing factors (Hindle et al., 2002; McQuarrie, 2002; Iaffaldano et al., 2006; Meade and Conrad, 2008; DeCelles et al., 2009). We build on decades of structural studies of the region and contribute: a sequentially deformed, isostatically balanced, thermo-kinematic model of the previously published Beni balanced cross section (McQuarrie et al., 2008) from 15-17°S; and the new Copacabana balanced cross section from 14-17°S to describe the geometric, kinematic, erosional and sedimentary evolution of the northern Bolivian Andes and assess proposed deformational models of the FTB.

We evaluate permissible ranges in age of initiation and rate of deformation through a forward kinematic model of the Beni restored cross section with applied isostasy to reproduce particle paths of measured thermochronometers in the FTB in conjunction with foreland basin chronostratigraphy. Kinematics from the Beni balanced cross section (McQuarrie et al., 2008) were used as an initial starting point in our modeling. The kinematic and flexural model predicts the location of structural highs, where erosion is focused, and creates flexural basins into which synorogenic sediments are deposited. Thermokinematic modeling (*Pecube*) was used to predict thermochronometer cooling histories based on kinematics, topography, thermal parameters and shortening rates. This combined modeling technique identifies relationships between FTB thermochronometry and synorogenic sediment data sets; and illustrates the effects of structural

geometry, kinematics, erosion, isostasy and thermal controls on central Andean mountain belt formation over the past 55 Ma.

2.0 GEOLOGIC SETTING

2.1 THE CENTRAL ANDES

The Central Andes reach elevations of 4 to >6 km with crustal thicknesses up to 60-70 km and record the highest shortening magnitudes along the ~ 8000 km long Andean mountain chain that extends from Columbia to Chile (Figure 1) (Beck et al., 1996; McQuarrie, 2002; McQuarrie et al., 2005; Barnes and Ehlers, 2009). The Bolivian, southern Peruvian and northern Argentinian regions of the Central Andes are home to the Andean plateau, an internally drained, high elevation (>3 km), low-relief, region, that has collected evaporites, volcanics and synorogenic sediments since the late Cretaceous (Horton et al., 2001; Horton et al., 2002; McQuarrie et al., 2005). The Andean Plateau overlies a zone of normal (~30°), east-dipping subduction of the Nazca plate beneath the South American plate, flanked by flat-slab subduction to the north and south (Figure 1) (Barnes and Ehlers, 2009). The modern foreland basin system, east of the Central Andes has been characterized by 4-7 km of Cenozoic wedge-top sediments and 3-5.5 km of foredeep Tertiary sediments (Horton and DeCelles, 1997, Baby et al., 1995). Along-strike similarities in elevation, stratigraphy, and structural style in the Central Andean FTB have linked the evolution of the orogen to the emplacement of two large (~10 km thick) basement thrust sheets, which have fed slip to the sedimentary rocks exposed at the surface (McQuarrie and DeCelles, 2001; McQuarrie, 2002).

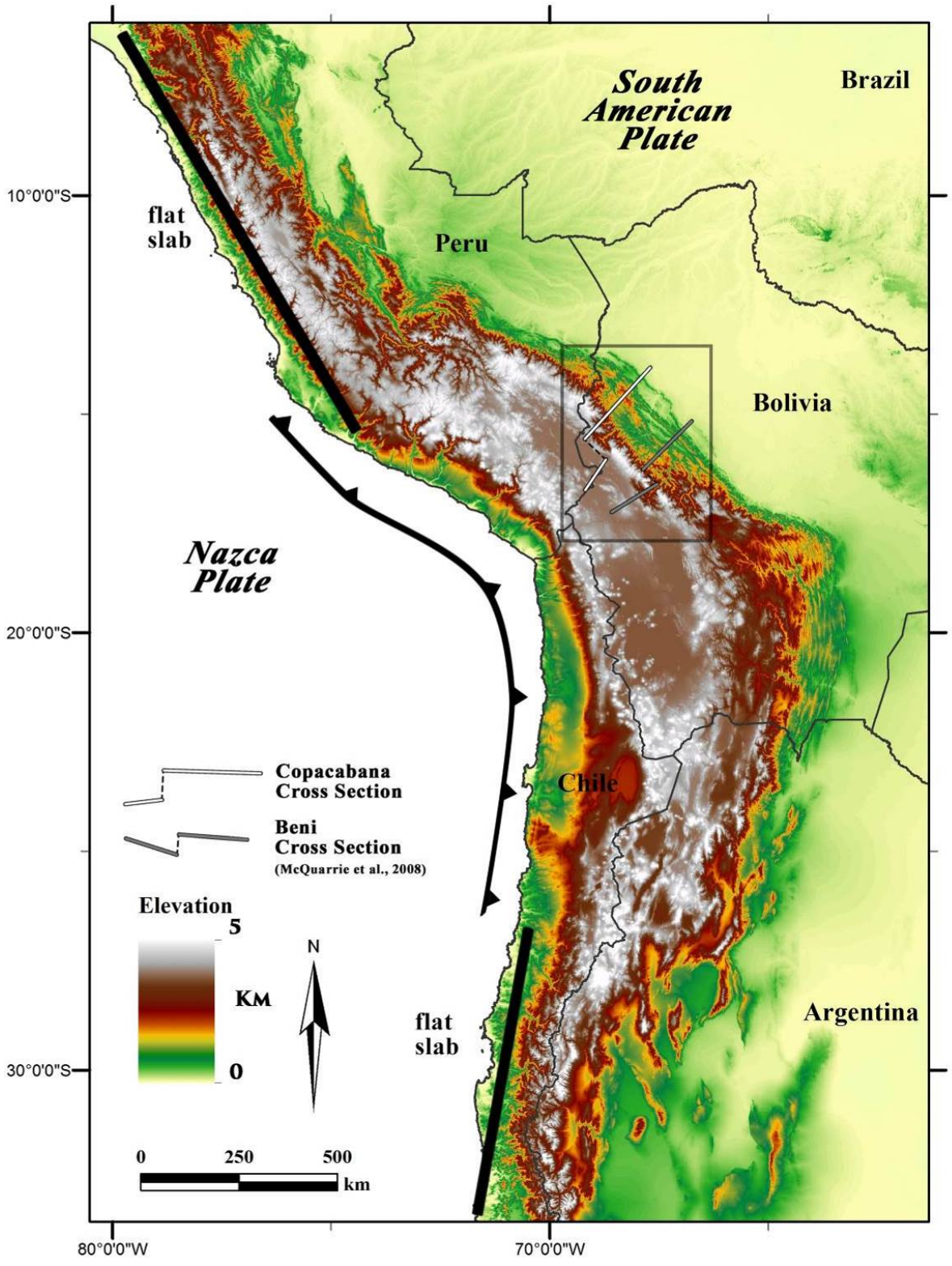

Figure 1. Regional map of the Central Andes. Color shade elevation map of the Central Andes with study location (gray box) and the location of cross section lines (gray and white lines). Thrust-fault symbol indicates subduction along the western margin of the continent with black lines signifying areas of flat-slab subduction (Barnes and Ehlers, 2009).

2.2 TECTONOMORPHIC ZONES

Based on structural, stratigraphic and topographic characteristics, the Central Andes is divided into several tectonogeomorphic zones and basins. From west to east these zones include: the Western Cordillera (WC); the Altiplano (AP); the Eastern Cordillera (EC); the Interandean zone (IA); the Subandean zone (SA); and the Beni basin (Fig. 2) (Allmendinger et al., 1997; McQuarrie and DeCelles, 2001; Leier et al., 2013). The WC is the active volcanic arc reaching elevations >6 km marking the Pacific-AP drainage divide (Isack, 1988, Allmendinger et al., 1997). The AP is a low-relief high-elevation (~3.7 km) internally-drained basin that has collected up to 12 km of Tertiary sediment (Horton et al, 2001; Horton et al., 2002). The EC is a bivergent FTB reaching elevations of 6.4 km composed dominantly of lower Paleozoic stratigraphy with minimal Mesozoic and Cenozoic sedimentary units (Fig. 3) (McQuarrie and DeCelles, 2001). The westward verging portion of the EC is referred to as the EC backthrust belt, while the eastward verging portion is referred to as the EC forethrust zone. The WC, AP and EC together comprise the Andean Plateau. The IA is a thin region of tightly folded, predominantly Paleozoic units that is characterized by a dramatic decrease in elevation coupled with an increase in structural elevation (Kley, 1996; McQuarrie, 2002). The SA is the actively deforming FTB characterized by long (10-20 km) thrust sheets of Paleozoic through recent rocks that produce synclines preserving 4-7 km of Cenozoic synorogenic sediment (Dunn et al., 1995; Baby et al., 1995). The Beni basin is the actively accumulating foreland basin with up to 4-5.5 km of Cenozoic sediment. Along-strike similarities in zones and basins indicate interconnected structural and sedimentary histories in the Central Andes of Bolivia.

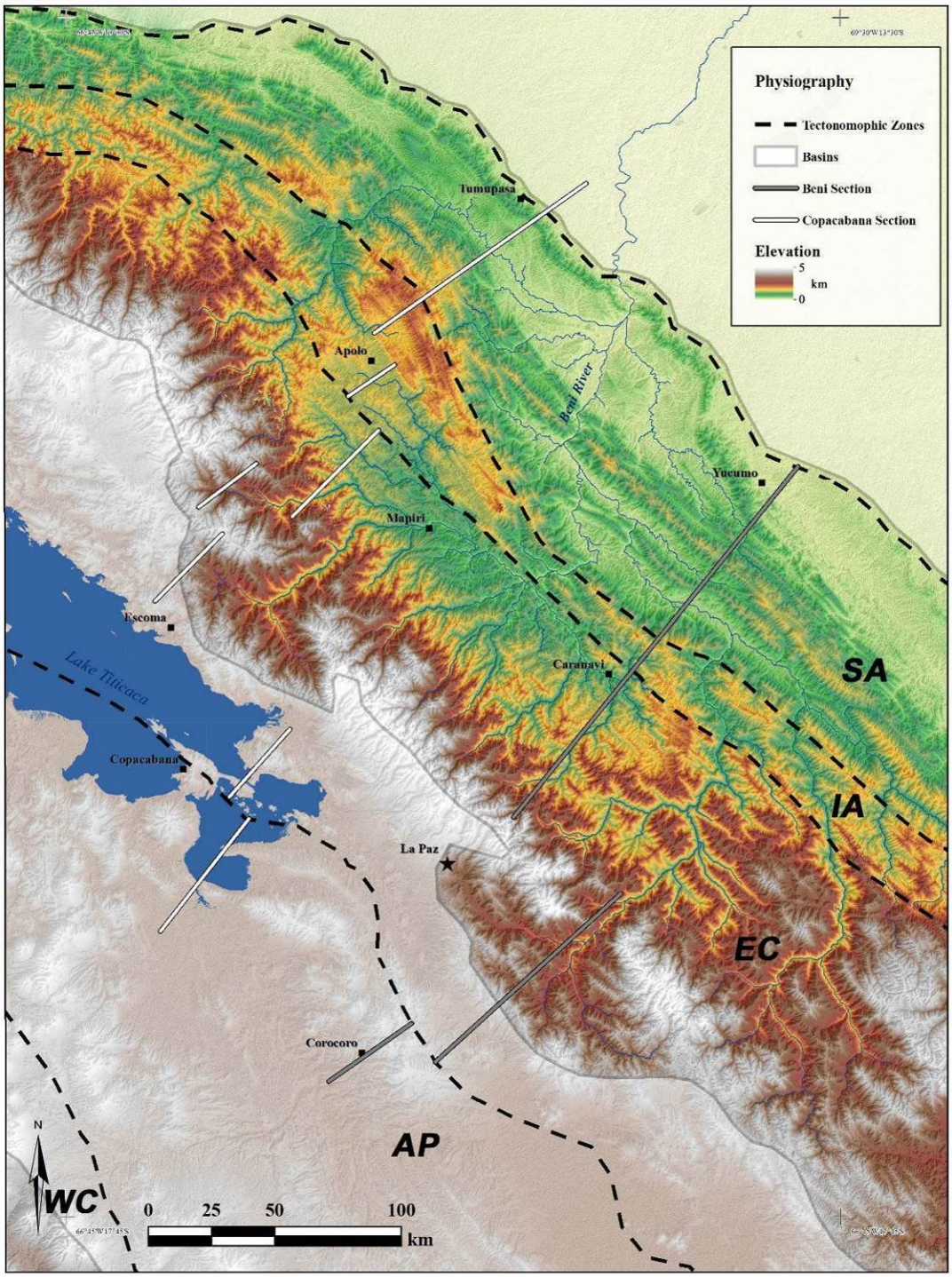

Figure 2. Map of study area showing physiographic features such as boundaries between tectonomorphic zones (dashed lines), basins (gray polygons) and rivers and lakes (blue) draped over a color shaded 30 m pixel resolution digital elevation model (DEM) in WGS 1984 Earth shape model. Tectonomorphic zones from west to east include: the Western Cordillera (WC); the Altiplano (AP); the Eastern Cordillera (EC); the Interandean Zone (IA); the Subandean Zone (SA) and the Beni foreland basin.

2.3 PALEOZOIC STRATIGRAPHY

The sedimentary strata involved in the Central Andean FTB is composed of a thick (~8-12 km), continuous Ordovician through Devonian marine siliciclastic sequence that is unconformably overlain by a thinner (2-4 km), non-marine to marine mixed carbonate and siliciclastic Carboniferous through Cretaceous package of rocks (Wilson, 1990; Sempere, 1995; Baby et al., 1995; Gonzalez et al., 1996; Grader et al., 2002; McQuarrie et al., 2008). Cenozoic synorogenic foredeep and wedge-top deposits are also incorporated in the FTB and are described in detail below. Lower Paleozoic slates, phyllites, quartzites, shales and sandstones have been determined to be thickest in the EC and gradually pinch out towards the hinterland and foreland (Baby et al., 1995; Gonzalez et al., 1996; McQuarrie and DeCelles, 2001; McQuarrie et al., 2008). Variably continuous Carboniferous through Cretaceous alternating carbonate, sandstone and shale formations reach their thickest extent in the western-EC and eastern-AP indicating a western migration of the basin depocenters through time. Upper Cretaceous shallow-marine limestone and clastic deposits are relatively continuous and similar in thickness (~200-900 m) across the orogen indicating this was the last time homogeneous deposition occurred across the region prior to FTB initiation (Horton, 2012; McQuarrie et al., 2008). Relatively minor unconformities during the late Devonian-early Carboniferous, late Permian, middle Mesozoic, and early Cenozoic are present across the region with variable spatiotemporal extents (Baby et al., 1995; McQuarrie et al., 2008). A pre-Cretaceous erosional unconformity juxtaposes Mesozoic rocks on top of upper and lower Devonian rocks in the EC back-thrust belt (Sempere, 1995). The distribution of Paleozoic and Mesozoic stratigraphy can be seen from geologic maps of the region (Fig. 3).

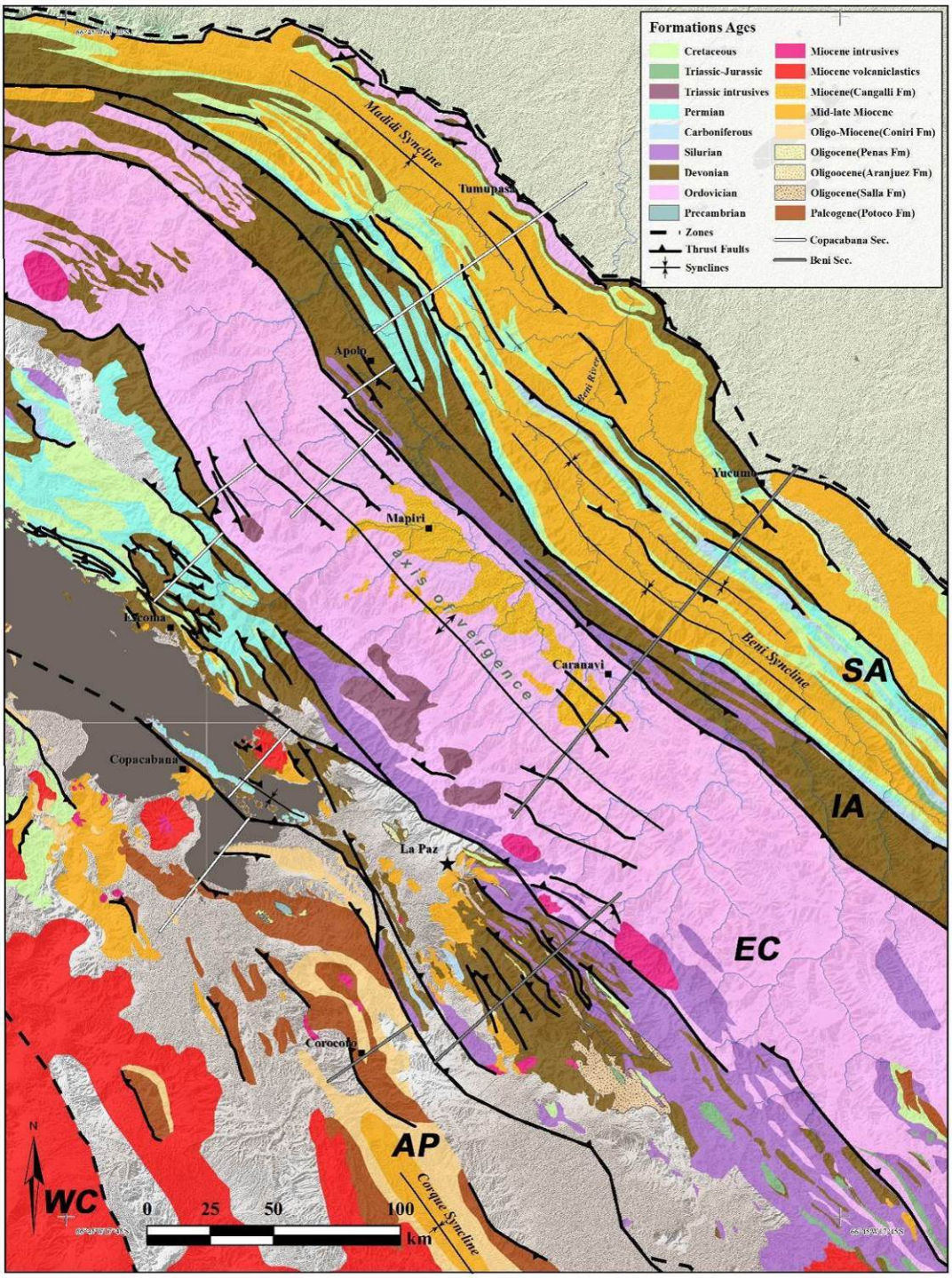

Figure 3. Geologic map of the study region with tectonomorphic zones (same as Fig. 2), prominent structural features and the location of the Beni and Copacabana cross sections (white and gray lines).

2.4 CENOZOIC FORLAND AND HINTERLAND BASIN DEPOSITS

Synorogenic sediments were deposited in the Altiplano and Beni basins throughout the Cenozoic. These basins were formed in conjunction with FTB shortening initially focused in the WC and subsequently in the EC (DeCelles and Giles, 1996; Horton et al., 2001). In the AP the Paleocene Santa Lucia sandstones and mudstones overlie the Cretaceous El Molino Formation. Westward directed paleocurrent data from the Santa Lucia (200-600 m) and the Potoco Formations (3-6 km), in conjunction with provenance data have been used to argue that these formations represent foreland basin deposits derived from the west (Horton et al., 2001; Horton, 2012; DeCelles, 2012). The FTB foreland basin system is interpreted to have propagated eastward capturing the AP, a crustal-scale piggyback basin, as deformation in the EC initiated causing middle to late Cenozoic structural-damming (Horton, 2012). The overlying Coniri Formation (~3 km) is dominated by sediments from the east, marking a time when significant sediment eroded from the EC was deposited in the AP basin (Horton et al., 2002; Horton et al., 2001). Geochronology from a single interbedded tuff sample from the AP was collected in the eastern limb of the Corque Syncline near the town of Corque (Kennan et al., 1995). The single sample yielded two biotite K-Ar ages (23.9 ± 1.3 Ma and 23.0 ± 0.8 Ma) that are projected along the Corque Syncline to the Beni modeled section (brown circle Fig. 4). These foreland and hinterland basin fill rocks in the AP are covered by (1-4 km) thick Miocene sandstones, conglomerates, and volcaniclastic rocks (Garzione et al., 2006). The entire Cenozoic package is approximately 12 km thick and represents a foreland to hinterland basin sequence that preserved sediment derived from deformed rocks on the western and eastern flanks of the AP. Initial deposition in the Beni basin and the SA is inferred to be 27-30 Ma based on vertebrate and leaf fossils in the basal, conglomeratic Bala Formation (Baby et al., 1995). Tertiary fill thicknesses

range from 4-5.5 km in the Beni basin and represent the modern retroarc foreland basin (Baby et al., 1995; DeCelles, 2012). Thick sedimentary wedge-top accumulations in SA synclines can range from 4-7 km thick and contain interbedded conglomerates from localized thrust faulting. A recent Ar/Ar interbedded tuff geochronology age of 22.1 ± 0.18 Ma (Mosolf et al., 2011) from the Beni Syncline is located between the axis of the syncline and the contact between Tertiary and Paleozoic rocks (brown square Fig. 4). Sedimentary accumulation is interpreted to have occurred in a continuous foreland basin that was subsequently partitioned by faulting facilitating structural damming and increased deposition in synclinal basins (Strub et al., 2006; Mosolf et al., 2011).

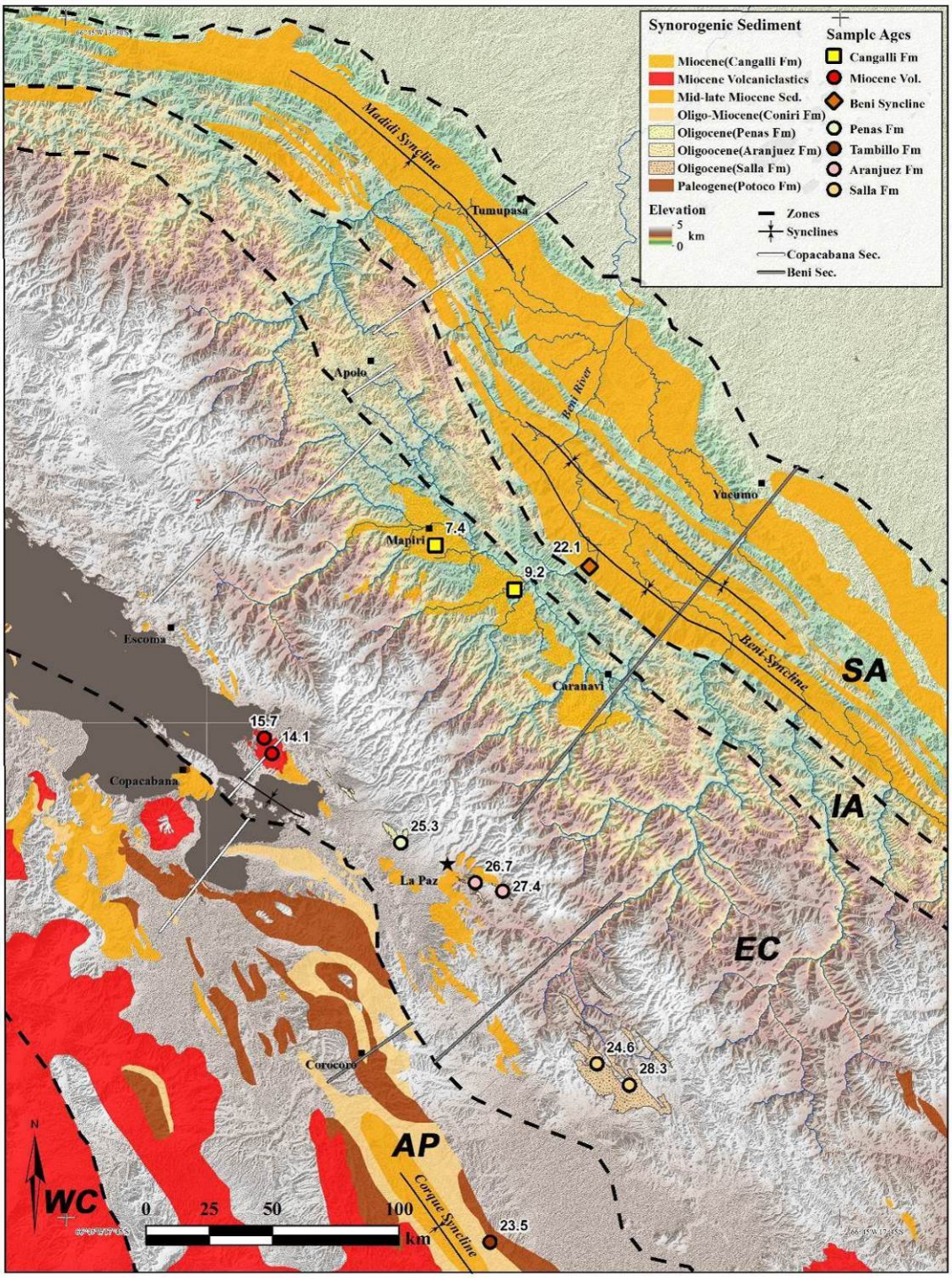

Figure 4. Synorogenic sediment map showing the locations and ages (Ma) of geochronologic samples draped over a color shaded elevation DEM of the study area with tectonomorphic zones (Kennan et al, 1995; GEOBOL 1997; Gillis et al., 2006; Murray et al., 2010; Mosolf et al., 2011).

2.5 WEDGE-TOP FORMATIONS

Wedge-top sediments, deposited on deformed and eroded Paleozoic rocks in the EC constrain the timing of deformation in the FTB. The Oligocene Peňas and Aranjuez Formations (27.41 ± 0.06-25.29 ± 0.04 Ma) unconformably overlay deformed Devonian rocks in the EC backthrust belt and are located northwest and southeast of La Paz, respectively (light green and pink circles, Fig. 4) (Murray et al., 2010). The Oligocene Salla Formation is located just south of the Beni cross section in the EC backthrust belt (McRae, 1990; Leier et al., 2010). Two interbedded tuff samples form the Salla Formation were dated to 28 ± 0.68 Ma and 24.59 ± 0.39 Ma (tan circles Fig. 4) (Gillis et al., 2006). The gently deformed Salla Formation was deposited from 29-24 Ma on top of the Luribay Conglomerate, a coarse synorogenic conglomerate which unconformably overlies deformed Devonian and Silurian strata (Leier et al., 2010). These Oligocene units constitute the oldest wedge-top sediments in the western EC and indicate deformation and erosion must have reached this region of the EC backthrust belt prior to their deposition. The late Miocene Cangalli Formation, located in the eastern EC forethrust zone, unconformably overlies Ordovician strata near the town of Mapiri (Mosolf et al., 2011). Two interbedded tuff deposits yielding ages of 9.12 ± 0.07 Ma and 7.41 ± 0.52 Ma (yellow squares Fig. 4) (Mosolf et al., 2011) were collected in conjunction with measured section, indicating deposition of this wedge-top formation was underway by ~10 Ma (Mosolf et al., 2011). Deformation and erosion of the Ordovician strata beneath the Cangalli Formation must predate the depositional age of the formation.

2.6 REGIONAL THERMOCHRONOLOGY

Previously published low-temperature thermochronometry samples from the northern Bolivia FTB record the cooling of rocks through specific closure temperatures and have been correlated to deformation-induced exhumation (Fig. 5) (Benjamin et al., 1987; Gillis et al., 2006; Barnes et al., 2006; McQuarrie et al., 2008). Early AFT and ZFT work on the Triassic plutons in the EC backthrust belt, northeast of La Paz, record 5-15 Ma AFT ages and a cluster of 30-45 Ma ZFT ages (Benjamin et al., 1987). Interpreted age elevation plots indicate cooling initiated at 45-40 Ma with a second phase of cooling starting at 25-20 Ma in conjunction with Oligocene granite emplacement (Benjamin et al., 1987). More recent thermochronometry studies of Triassic plutons, including AFT, ZFT, and K-Feld Ar/Ar revealed similar trends of initial exhumation occurring at 45-40 Ma with a deceleration in the rate of cooling from 25-11 Ma (Gillis et al., 2006). Young AFT ages (15-5 Ma) argue for rapid cooling from ~10 Ma to present (Benjamin et al., 1987; Barnes et al., 2006; Gillis et al., 2006; Safran et al., 2006; Barnes et al., 2012). Integration of these cooling ages and systems with a balanced cross section suggests a significant deceleration in the rate of deformation occurred between 25 and ~15-8 Ma (McQuarrie et al., 2008). The young pulse of rapid exhumation (*~10 Ma to present) has been linked to both active uplift in the EC (Whipple and Gaspirini, 2014) as well as enhanced orography due to the mountain range reaching a critical elevation that enhances precipitation (Barnes et al., 2012). Active deformation in the SA is confirmed by young 7-0 Ma exhumation (recorded by apatite U-Th/He (AHe)) of rocks sampled immediately above thrust faults (Lease and Ehlers, 2014). Together these thermochronometer samples provide a multi-system thermochronometric dataset across the Andean FTB that describes the cooling history of rocks across the eastern margin of the northern Bolivian Andes.

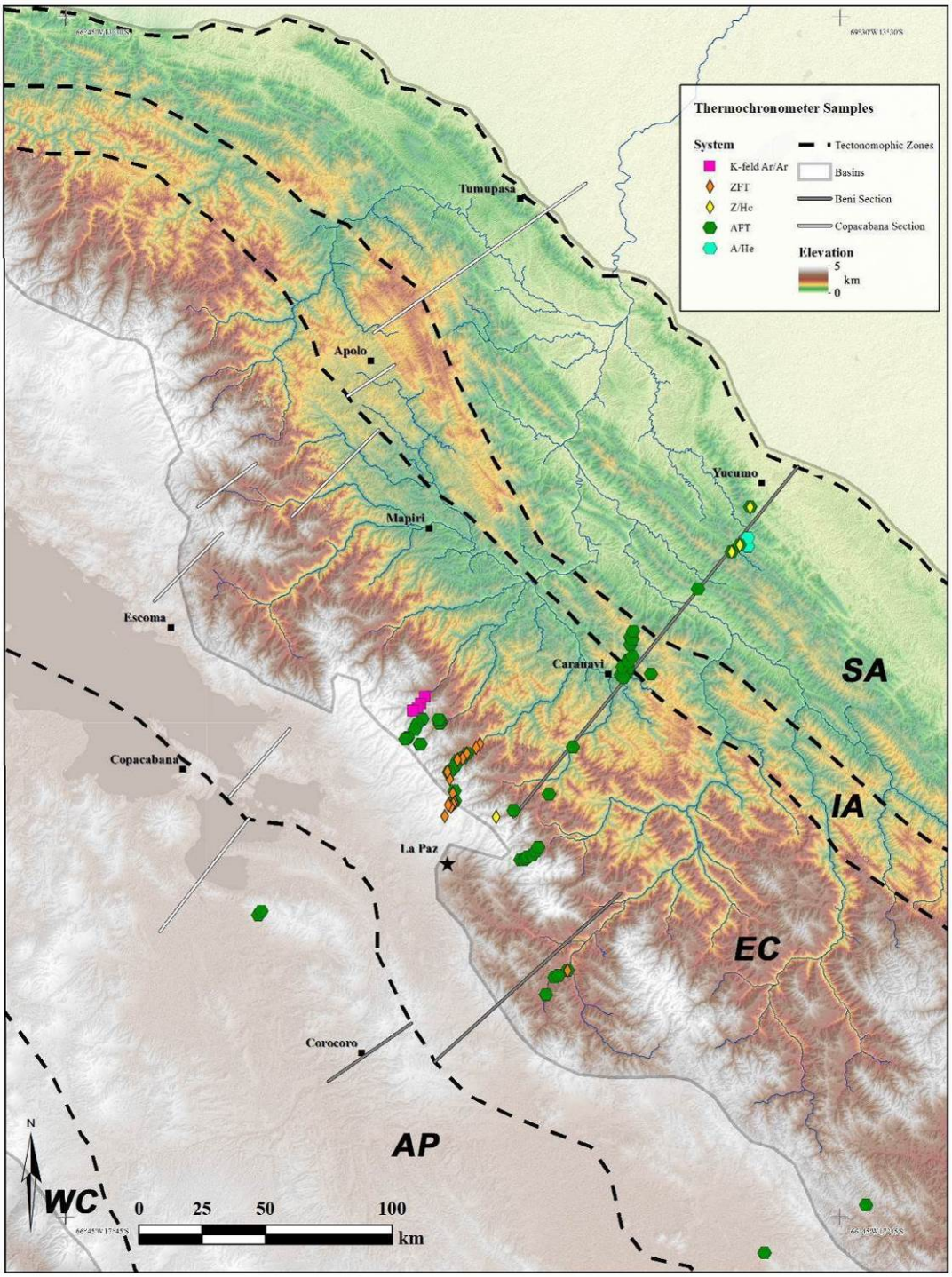

Figure 5. Color shaded elevation map showing the location of thermochronometer samples from the northern Bolivian FTB (Benjamin, 1987; Gillis et al., 2006; Barnes, 2006; Safran et al., 2006; McQuarrie, 2008; Barnes et al., 2012), with tectonomorphic zones and basins (same as Fig. 2).

2.7 GEOMOPHIC INDICIES

Geomorphic analysis of the Beni escarpments (BE Fig. 6) suggests recent uplift, erosion and exhumation has occurred to produce the high peaks of the EC. A model to produce this uplift is a crustal-scale ramp, located immediately to the east of the high topography in the Beni escarpment, which is part of the active decollement fault for the FTB (white polygon Fig. 6) (Whipple and Gasparini, 2014). Topography in the northern Bolivian Andes' eastern flank is characterized by discontinuous escarpments with 3-4 km of relief, high precipitation gradients and steep channels (Fig. 6) (Whipple and Gasparini, 2014). No correlation between cosmogenic radionuclide derived erosion rates and rock type was identified, indicating variation in uplift and precipitation are the main components controlling channel morphology (Safran et al., 2006; Gasparini and Whipple, 2014). Channel steepness index (normalized to drainage area, k_{sn}) and local relief were used to recognize differences in uplift and identify low-relief, paleo-landscapes (tan polygons Fig. 6B) from a processed digital elevation model (DEM) (Whipple and Gasparini, 2014). Numerical landscape evolution modeling identified the need for active uplift, in addition to rainfall gradients to produce topographies and drainage channels with similar k_{sn} to those observed in the Beni escarpment (Gasparini and Whipple, 2014). This region of active uplift at the western edge of the Beni escarpment was used to identify the region of uplift, which was interpreted to be a decollement ramp (Gasparini and Whipple, 2014; Whipple and Gasparini, 2014). The location of modern uplift identified through geomorphic indices is spatially coincident with young AFT ages recording rapid exhumation in the EC (Whipple and Gasparini, 2014).

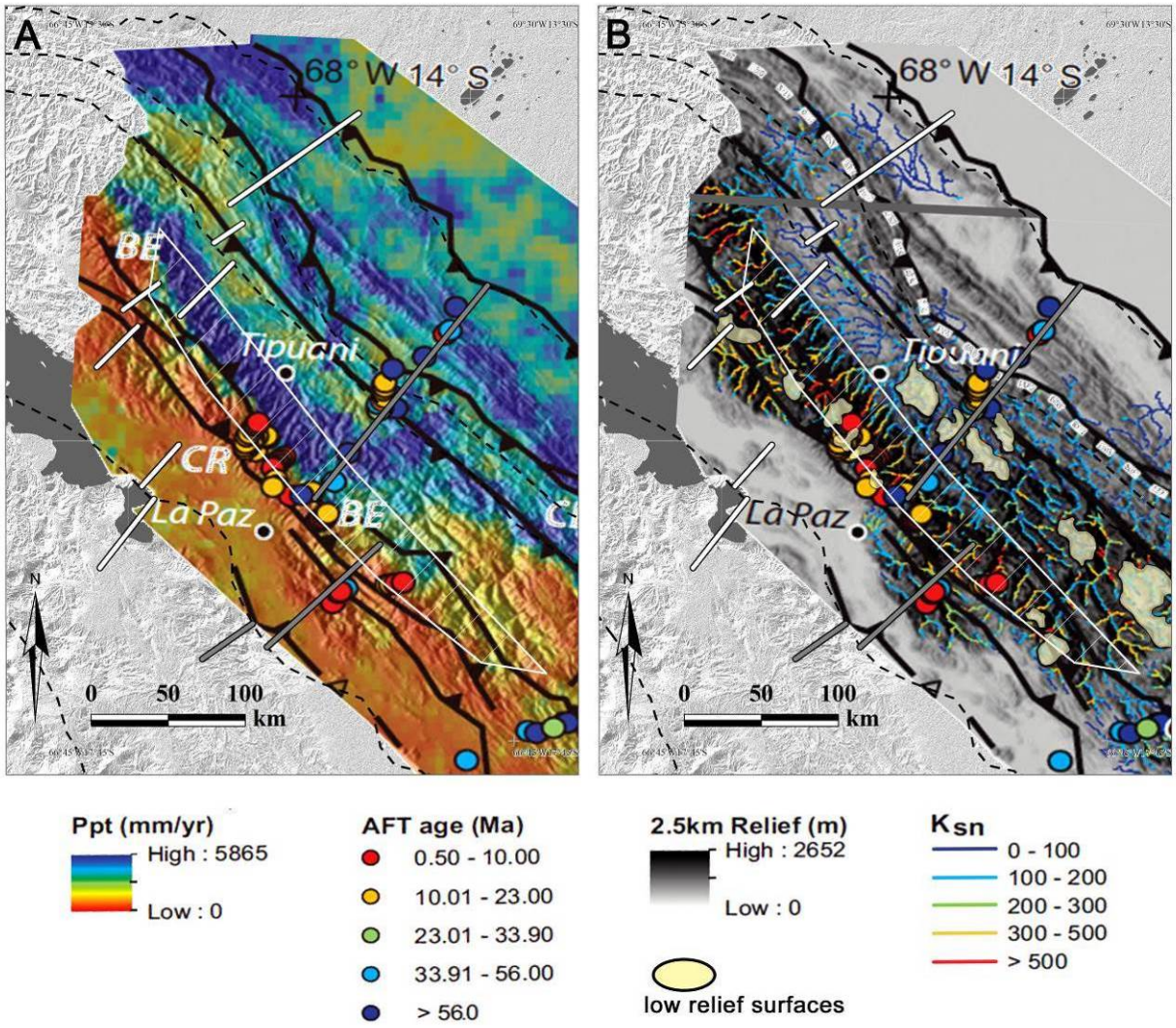

Figure 6. Maps of mean annual precipitation and geomorphic indices of northern Bolivia with the locations of the Copacabana (white lines) and Beni (grey lines) cross sections overlain on 30 m pixel resolution hillshade DEM (Whipple and Gasparini, 2014). (A) Mean annual precipitation with major faults (from McQuarrie, 2002) and published AFT ages from the region (Whipple and Gasparini, 2014). High precipitation gradients in the Beni Escarpment (BE) is correlated to the interpreted basement decollement ramp (white polygon). (B) Local Relief (measured within a 2.5 km radius of each pixel) with channel steepness (k_{sn}, $m^{0.9}$) for major channels that drain high elevations (reference concavity 0.45), low relief surfaces (tan polygons), and AFT data from the region (see Whipple and Gasparini, 2014 for full description).

2.8 GEOPHYSICAL CONSTRAINTS

Geophysical studies provide some important cross section constraints, which include: identifying the depth of the Beni basin and the Mandidi Syncline in the SA; and indicating the approximate location of basement (fast velocities) near the surface in the EC (Zubieta Rossetti et al., 1996; Gil, 2002, Ward et al., 2013). The Beni basin was determined to be ~4.0-5.5 km thick near Tumupasa by converting two-way travel-time to depth by utilizing a ~3-4 km/s seismic velocity for the Tertiary fill and extending the interpretation north (Zubieta Rossetti et al., 1996; Horton and Decelles, 1997). The angle of the foreland decollement is interpreted to be 4° based on industry seismic reflection and gravity and well data (Watts et al., 1995; Baby et al., 1995; Zubieta Rossetti et al., 1996). The depth of the Mandidi Syncline has been interpreted to be 3-4 km, as constrained by two industry seismic reflection transects which also indicate the style of deformation in the SA front (Gil, 2002). Shear wave velocity model of the northern Central Andes identify: a low-velocity zone in the AP around 15 km depth; a high-velocity perturbation near the center of the EC in the upper 15 km where basement is close to the surface; and low-velocities in the SA in the uppermost 5 km associated with large, actively deforming, piggyback basins like the Beni Syncline (Ward et al., 2013). Specific cross sections through the shear wave velocity model by Ward et al., (2013) along the Copacabana cross section show a shallow-crustal high-velocity perturbation in the EC flanked by low-velocity regions in the SA and AP (Fig. 7). Cross section constraints provided by these geophysical studies were used in conjunction with surface geology and geomorphic analyses to construct the Copacabana cross section.

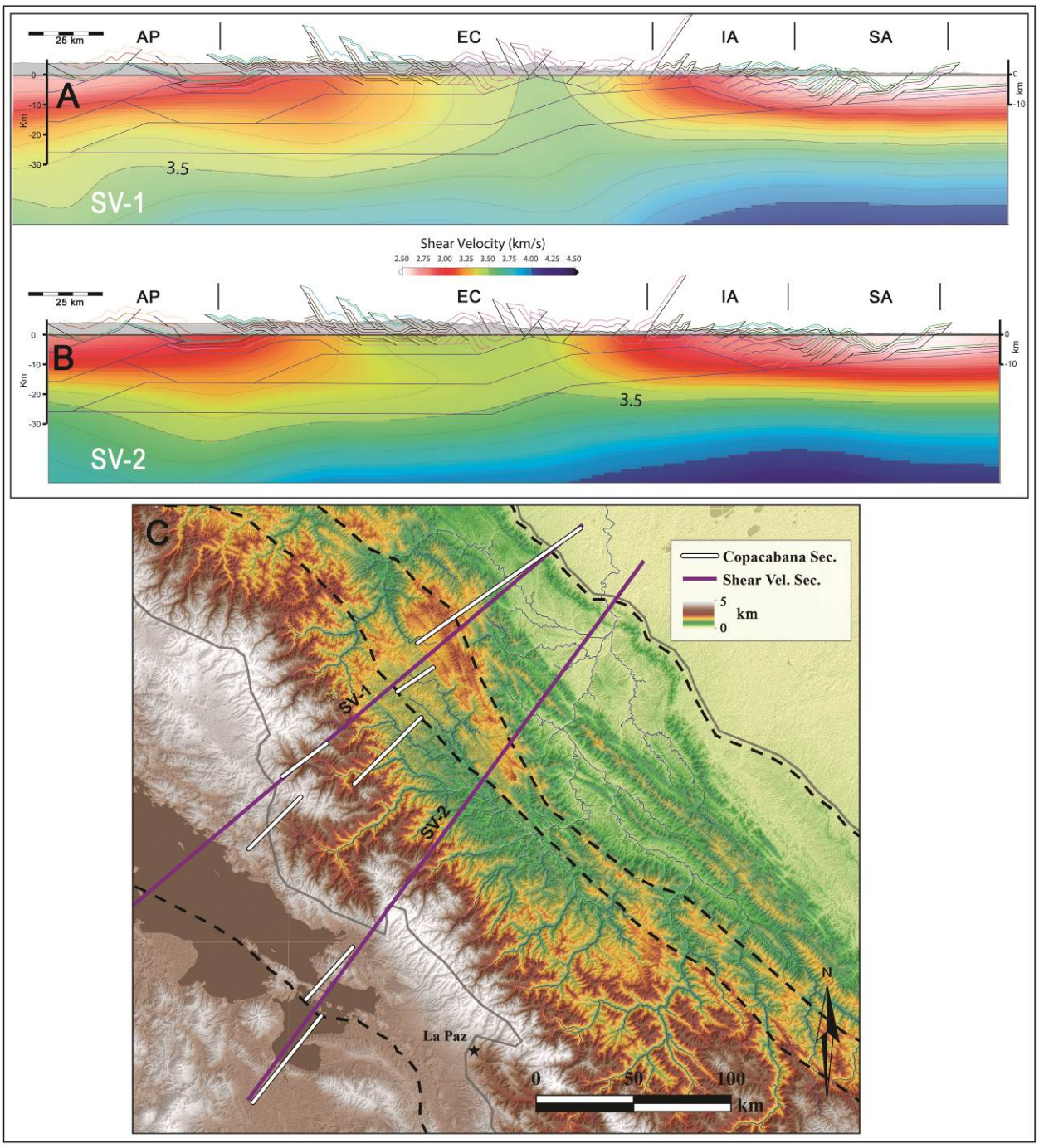

Figure 7. Cross sections through a shear velocity model (A and B; Ward et al., 2013) from an ambient noise tomography study showing upper crustal shear velocity variations. Color shaded DEM map (C) shows the location of shear velocity cross sections (purple lines) in relation to the Copacabana cross section (white lines).

3.0 METHODS

3.1 COMPONENETS

This study combines mapping and creation of a new cross section (Copacabana Cross Section) close to the Peru-Bolivia border with thermokinematic modeling of the previously published Beni Cross Section (McQuarrie et al., 2008) located 50-100 km south of the Copacabana Cross Section. Both cross sections trend northeast and extend from the Altiplano to the Beni Basin. Results from Beni cross section modeling and Copacabana balanced cross section development are correlated to present a framework describing the deformation history of the northern Bolivian Andes.

3.2 COPACABANA CROSS SECTION

The Copacabana cross section extends ~325 km northeast from the AP (60 km south of Copacabana) to the Beni Basin (25 km east of Tumupasa). The cross section is split along several prominent along-strike structures to maximize field transect data and traverse Lake Titicaca.

3.2.1 Geologic Mapping

New geologic mapping of the region builds on previous geologic maps and integrates a new transect of field data and remote sensing data. Previous geologic maps, at a variety of scales (1:100,00 to 1:1,000,000), were combined with recently published maps from journal articles at a 1:100,000 scale and smaller to produce a continuous map of the study region (Fig. 3) (Departmento Nacional De Geologia, Buletin 2, 1962; Servicio Geologico de Bolivia (GEOBOL), 1995a, 1995b, 1995c, 1996, 1997; Yacimientos Petrolíferos Fiscales Bolivianos (YPFB), Rio Suches, Ancoraimes, Puerto Acosta; Instituto Geologico Minero Y Metalurgico, Peru, [1983, 1984, 1996]; Horton et al., 2002; Gillis et al., 2006; McQuarrie et al., 2008; Murray et al., 2010; Mosolf et al., 2011). The new NE trending transect from Escoma to Apolo, traversing ~120 km of the Bolivian FTB was collected in 2011 and takes advantage of excellent exposures of the EC in the Mapiri River catchment (green triangles Fig. 8). Foreland regions of the FTB, primarily the SA, contain limited strike-and-dip information and limited field access. To populate this area with bedding data we obtained remote attitude data through a *Matlab* script that solves a three-point-problem on exposed dip-slopes (blue squares Fig. 8). Lithology band-math and spectral enhancements were applied to shortwave infrared (SWIR) and thermal infrared (TIR) Advanced Spaceborne Thermal Emission and Reflection Radiometer (ASTER) satellite imagery across the EC back thrust belt and the eastern AP to determine contacts between units with unique spectral characteristics (gray rectangle Fig. 8). Strike-and-dip data, from published geologic maps, from the EC backthrust belt and AP was integrated and used in the new geologic map compilation and cross section creation (pink circles Fig. 8). Geologic maps of the region were combined with field data and remotely sensed data to create the homogeneous map of the study area (Fig. 3).

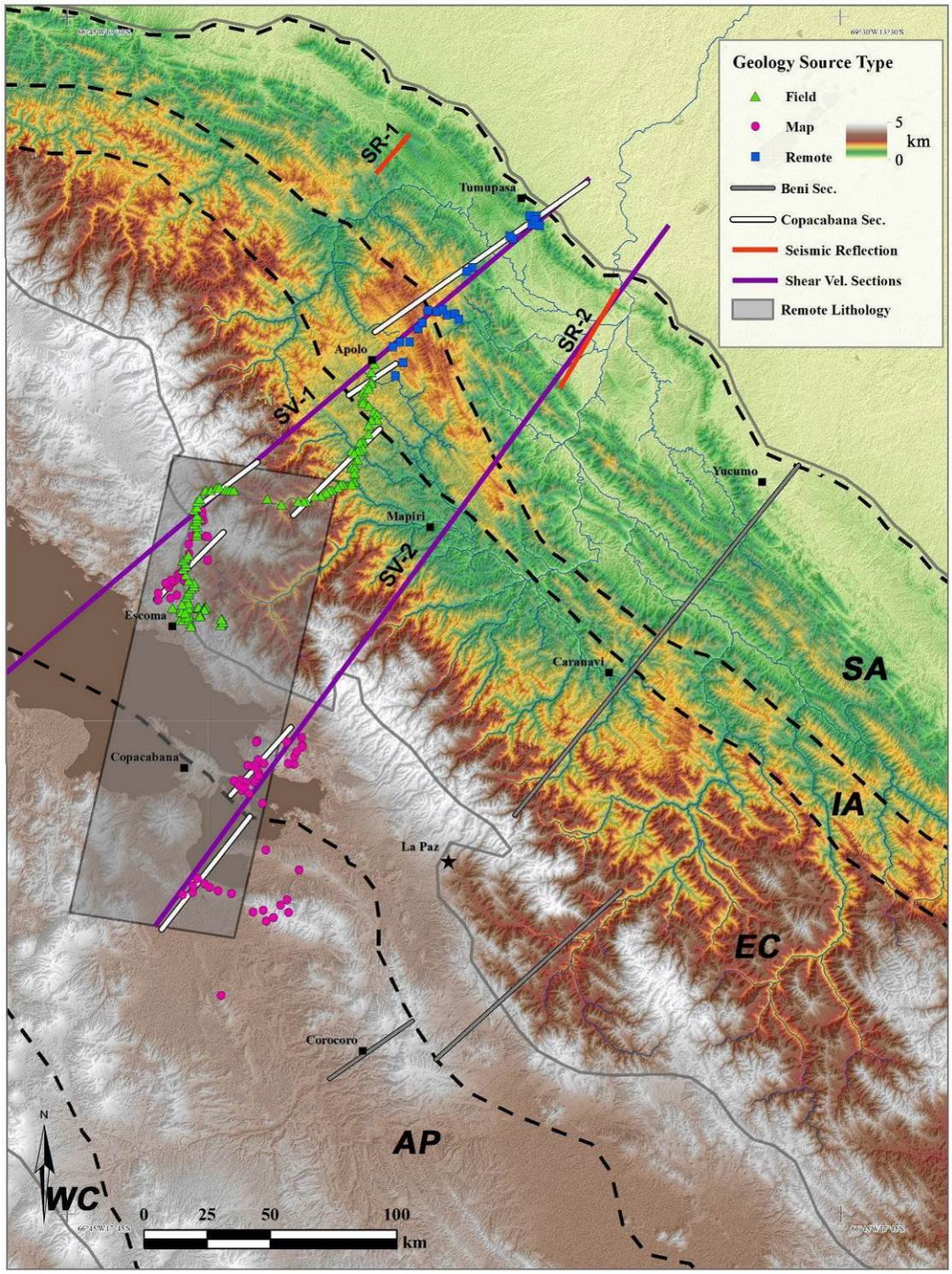

Figure 8. Geologic source type information map showing tectonomorphic zones, cross sections remote sensing area and point location sites on a color shaded DEM map.

Geologic field work was conducted from Escoma to Apolo providing geologic formation information, structural outcrop observations and strike-and-dip data for each georeferenced

location. Field sites near Escoma overlap with geologic maps (at 1:1,000,000; 1:250,000; 1:175,000; and 1:145,000 scales) and remotely-sensed lithology analysis area facilitating comparison and integration of the datasets. Spectral lithology mapping was performed on a rectangular area (60x180 km) trending perpendicular to the structural fabric of the FTB containing lower Paleozoic through upper Cenozoic siliciclastic and carbonate sedimentary rocks, volcanics and modern evaporite deposits in the EC and AP (Grey rectangle Fig. 8). Spectral analysis was conducted on three linked-pass (sequentially recorded) multispectral images collected by the ASTER sensor in the TIR and SWIR regions of the electromagnetic spectrum at 90 m and 30 m pixel resolution, respectively. Mineralogic band-ratio indices were applied to the TIR images in addition to a decorrelation stretch enhancement to highlight regions with different spectral characteristics (Rockwell et al., 2008; Ninomiya et al., 2010). A decorrelation stretch (bands 4, 6, 9 in R, G, B) and a clay band-ratio indices (See table 2 in Gozzard, 2006) were applied to the SWIR images to identify differences in spectra at a finer resolution and complement TIR analyses (Gozzard, 2006; Rajendran and Nasir, 2014). A training area, southeast of Copacabana, was used to link spectral signatures to lithologies in this well-mapped location, east of Copacabana (Wilson, 1990; Grader et al., 2003). Correlated signatures were used to interpret geology in the less-constrained area of the EC back thrust belt southeast of Escoma.

Remote strike-and-dip information was obtained through the application of a three-point-problem *Matlab* algorithm that was applied to specifically identified dip-slopes in the SA and eastern IA region of the Copacabana cross section (blue squares Fig. 8). The script was applied to 30 m pixel resolution ASTER DEM images by selecting specific location for slope analysis. Dip-slopes were identified by correlating geologic maps to DEM images and other

complementary satellite imagery (e.g. ASTER visible imagery, Google Earth imagery). Results of the analysis were filtered to identify outliers and determine accurate measurements. Remotely derived strike and dip information was compared to geologic maps, cross sections, and previously published research from the SA for quality control (Baby et al., 1995; Strub et al., 2003; Gil, 2002).

3.2.2 Balanced Cross Section Construction

The constructed cross sections were constrained by geophysical, geomorphic, and mapped geology datasets. The Copacabana cross section is line-length balanced and requires consistency in fault displacement necessary for a viable kinematic solution. Geometry used in each tectonomorphic zone correlates to geologic map patterns seen and recorded at the surface and relates to the type of deformation exhibited in these zones along strike (McQuarrie and DeCelles, 2001; McQuarrie et al., 2008; Eichelberger et al., 2013). Duplexing of lower stratigraphic units, and/ or involvement of basement rock, is necessary to account for the structural elevation of these rocks above their location identified in drill holes and seismic in the foreland basin. The proposed basement structures are correlated with long-wavelength changes in exposure of rocks at the surface (Kley, 1996; McQuarrie and DeCelles, 2001) and are required to distribute slip to faults exposed at the surface. The location of the active basement ramp strongly controls shortening estimates by dictating the amount of basement thrust sheet involvement in SA deformation (McQuarrie, 2002). The eastern edge of the basement ramp has been interpreted to be located near the western base of the Beni Escarpment (white polygon Fig. 6) based on geomorphic indices. The geomorphic expression of an active ramp agrees well with a high sheer-wave velocity region in the EC (Ward et al., 2013; Whipple and Gasparini, 2014).

In addition, the EC-AP contact mandates a vertical offset of ~12 km, which is best explained as a result of an ancestral basement footwall ramp (McQuarrie and DeCelles, 2001). Exposure of Precambrian rocks covered by Cretaceous stratigraphy west of La Paz places basement thrust sheets near the surface and necessitates the pinching out of the entire Paleozoic and lower Mesozoic package beneath Lake Titicaca. The Copacabana balanced cross section adheres to the geometric and kinematic constraints presented in section 4 and provides a viable structural model for the northern Bolivian Andes.

3.3 BENI CROSS SECTION MODELING

3.3.1 Initial Conditions

Kinematic modeling of the Beni cross section was conducted under the assumption that the deposition of the Potoco Formation predates any influence of EC sediment-source deposition (Horton et al., 2001). In *Move* (Midland Valley), a 2-4.4 km package of flexurally accommodated basin sediment is produced through 200 km of shortening in the pre-WC. The effective elastic thickness (EET) was decreased from 100-70 km as the pre-WC FTB became proximal to the AP basin. Deformation in the model was performed with the fault-parallel flow algorithm and the density of the crust was set to 2900 kg/km^3 similar to other modeling studies (Sobelev and Babeyko, 1994; Lucassen et al., 2001; Oncken et al., 2012). Topography evolves for each deformation step, inducing erosion of uplifted material, using a modified-version of critical wedge theory and applying a max elevation cut-off (described in detail below). Topographies have upper critical wedge angles of 4-6° on the east facing slope, measured from

the deformation front, and maximum elevations of 6-7 km that is tapered to the forearc. This exercise was undertaken to reproduce basin sediment preserved in the AP and is not included in the thermokinematic modeling.

3.3.2 Sequential Deformation and Isostasy

Sequential deformation of the Beni cross section was performed in *Move* with the fault-parallel flow algorithm using the kinematics proposed by McQuarrie et.al. (2008). Initially, the restored cross section is forward modeled to reproduce the deformed cross section. The deformation history is subsequently divided into ~10 km deformation steps. After each ~10 km deformation step, isostasy is applied to account for thrust loading and erosional unloading. After a thrust fault moves, the isostatic load for the model is calculated from the difference between the deformed topographic surface and the original topographic surface before deformation (fig. 9b). A new topography is created for each ~10 km deformation step by applying a modified-version of critical wedge theory implemented through a Python script. The script uses the deformed (and loaded) topographic surface to calculate where elevation has increased through motion on structures. It defines a new topographic profile based the deformed topography, a deformation front location and an angle of the new topographic surface (upper critical wedge angle) (fig. 9c). Basins are filled to 0 elevation and maximum elevation limit is also applied (~6 km) to mitigate erroneously tall mountains peaks in the hinterland of the FTB. The new topography increases at the prescribed topographic angle where uplift has occurred, and follows the previous topographic surface where it has not (Fig. 9c and 9d). Material that lies above the new topographic surface is removed and this erosion is isostatically accounted for by calculating

the difference between the isostatically loaded, deformed topography and the newly generated topography. Topographic angles on east facing slopes ranging from 1-4^0 in the EC and WC. On the eastern side of the EC, topography was limited to a max elevation of ~6 km, with isolated peaks reaching as high as 7.6 km, and tapered into the AP. As the FTB is deformed, flexural basins are created and then filled. Basins formed early in the model become incorporated into the FTB and erode while the foreland basin as a whole migrates towards the modern foreland and deepens through time. A persistent load (due to structural uplift) concentrated at the AP-EC border facilitates the continued growth of the AP basin.

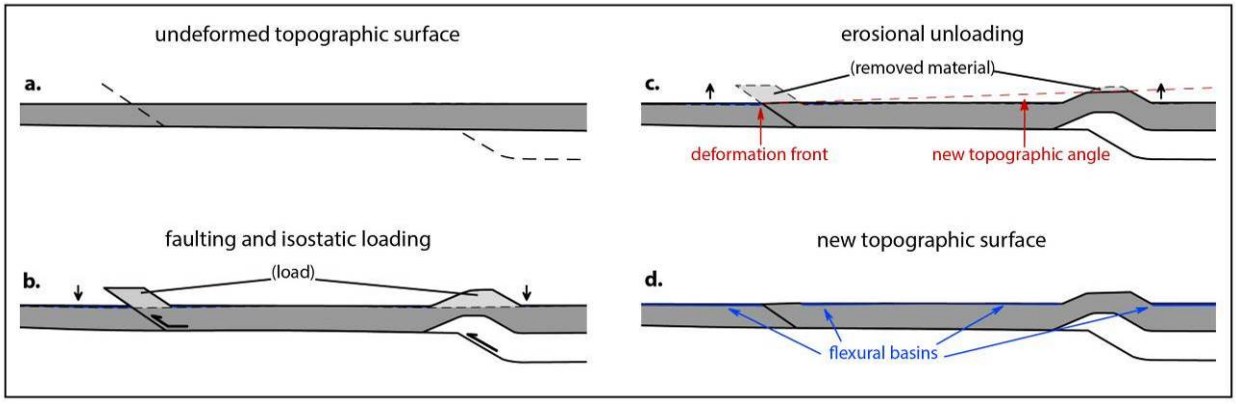

Figure 9. Illustration of deformation and isostatic compensation modeling sequence. Images show the simplified restored cross section (a), motion on a fault and isostatic loading (b), generation of new topography and erosional unloading (c), and the new topographic surface with flexural basins (d).

The isostatic model was completed iteratively while varying crustal density and EET to reproduce the foreland and hinterland basin thickness, angle of the decollement in the foreland, and the modern geology and the topography along the line of section. For the preferred isostatic modeling sequence, crustal density was set to 2900 kg/km^3 while EET was increased as the model progressed from 30 km to 70-90 km to simulate increased rigidity of the continental lithosphere as shortening accumulated (DeCelles, 2012). Despite the high crustal density and the variation in EET, the predicted Beni flexural foreland basin deposits were still too thin. In

addition elevations in the hinterland, the long-lived locus of deformation, were far too low, necessitating the use of an additional modeling step.

To account for the thick SA foreland basin deposits and the modern elevation of the EC and AP a long-wavelength subsidence was applied in the foreland and uplift was applied to the hinterland. Subsidence was applied to the foreland basin after initiation of the second basement thrust sheet (B) and during major shortening of the SA. Uplift was applied to the EC and AP over the same interval of deformation to maintain a high topography in the loci of long lived deformation. These long wavelength vertical adjustments were made by using the unfolding module in *Move*. A reference line, like the basal decollement, is chosen, copied and modified into a sine curve with the inflection point at the SA-IA border. Maximum vertical subsidence (-350 m) is located in the center of the SA while maximum vertical uplift (~500 m) is centered in the EC. Uplift decreases to 0 at the WC and at the eastern limit of the Beni foreland basin. The model is then unfolded to the reference line imposing the prescribed vertical motion to the cross section and associated grid. Thus the SA deepened, centered in synclinal basins, and uplift was added to the EC and the AP during each deformation step. This approach allows the model to reproduce the anomalously thick sediment deposition in the foreland, maintain high elevations in the hinterland, and accurately reconstruct particle paths towards the surface. Geodynamical arguments in support of both dynamic subsidence of the foreland basin and non-flexurally derived uplift for the Andean plateau are elaborated on in the discussion section.

After the modern geologic conditions of the cross section are reproduced, a 0.5x0.5 km grid of unique points are deformed in ~10 km deformation steps to trace particle paths in the model. These unique point paths are exported to create vectors of displacement that are converted to velocity fields by assigning time to each deformation step. Timing between each

deformation step is varied to create velocity models presented in this study. Constant rates of shortening are initially tested while varying the initiation age of deformation, with more complex velocity models explored thereafter. Velocity models and topographies are used as inputs to a modified version of the thermo-kinematic and erosion modeling software, *Pecube*, that predicts thermochronometer cooling signals based on geometry, shortening rate, and thermal parameters. Measured thermochronometer data were plotted along the measured section and are compared to predict cooling ages to constrain rates of shortening through time.

3.3.3 *Pecube* Thermal Modeling

Thermal modeling was conducted using kinematics and surface topographies from the preferred isostatic model, in conjunction with thermal parameters, and a variety of velocity models that describe the magnitude and rate of displacement for the advection-diffusion algorithm in *Pecube* (Braun, 2003; Whipp et al., 2009). *Pecube* models the evolving subsurface thermal field based on input thermal parameters and imported velocity fields to derive the time-temperature (t-T) history of p articles based on their transport path. Predicted cooling ages of mineral systems along the model-surface use thermochronometer kinetics described in both Ehlers et al., (2005) and Braun (2003). By fixing all but one input variable the effect of the parameter of interest on predicted thermochronometer cooling signals can be assessed (McQuarrie and Ehlers 2015). Shortening velocity models or thermal parameters were varied while kinematics (geometries) and surface topographies were kept constant to determine the sensitivity of the model to differences in rates of shortening or thermal state of the crust. The parameters were varied to determine which set of parameters most accurately reproduced thermochronometer cooling signals observed in the study region as well as how sensitive the

predicted cooling ages were to the age of initiation, rate of deformation or the range of realistic thermal properties. Cross section geometry, specifically the location of ramps, control particle paths towards the surface and exert a first order control on predicted thermochronometer ages (McQuarrie and Ehlers, 2015). We limit the number of geometries tested to the original kinematic model proposed by McQuarrie et al., (2008) and a second, modified kinematic model. Three thermal scenarios are presented to illustrate the effects of different thermal conditions on predicted ages; a cool scenario, a warm scenario, and a hot scenario. We illustrate the effects of geometry and thermal state of the crust but focus on how variation in age of deformation initiation and deformation rates affect predicted thermochronometer cooling along the modeled section.

The model extends 900 km and represents the South American margin, after the deposition of the Potoco Formation, and includes >80 km of length on the eastern and western edge to maintain a zero flux lateral boundary in the model. The model extends to a depth of 110 km and maintains constant temperature boundaries at the surface and 1300° C at its base. Temperatures at the surface at sea level are 23 C° (Santa Cruz yearly average) and decrease with elevation at a rate of 5.3 C°/km, the mean lapse rate measured in Bolivia (Gonfiantini et al., 2001). Radiogenic heat production was varied from 0.5 $\mu W/m^3$ to 0.7 $\mu W/m^3$. Mantle density and crustal density were maintained at 3300 and 2750 kg/m^2. Thermal conductivity was kept constant at 2.5 W/m K and specific heat capacity was set to 800 J/kg K° in accordance with global averages of crustal rocks (Ehlers, 2005). *Pecube* model parameters are summarized in table 1 and are similar to recent comparable thermochronometer modeling studies of the Bhutan Himalaya (Gilmore, 2014; McQuarrie and Ehlers, 2015).

Table 1. *Pecube* thermokinematic modeling properties

Model property	Input Values
crustal volumetric heat prod. (Ao)	0.5-0.7 mW/m3
e-fold depth	None
thermal conductivity	2.5 W/m K
specific heat	800 J/kg K
density	2750 kg/m3
model base	110 km
temperature at base	1300°C
temperature at surface	0 km 23 °
atmospheric lapse rate	5.3°/ km
kinematic grid spacing	0.5 km
displacement increment	~10 km
model domain	900 x 110 x 5 km
horizontal node spacing (numerical model)	0.5 km
vertical node spacing (numerical model)	1.0 km
model start time	100 Ma

3.3.4 Chronostratigraphic Correlation

Flexurally modeled basin sediment ages, as determined by velocity models, were compared to published chronostratigraphy to determine temporal relationships between modeled thermochronometer cooling and sediment accumulation. The stratigraphic location of dated ash-fall beds in the hinterland and foreland were compared to modeled sediment ages in each of the velocity models. A single interbedded volcanic tuff sample from the Beni syncline produced an Ar/Ar age of 22.1 ± 0.18 Ma and was described as being located in the lower levels of the clastic succession (Mosolf et al., 2012). The Beni syncline sample is located midway between the IA thrust and the axis of the syncline. The sample was placed in the stratigraphic column by projecting the sampled layer into the stratigraphy preserved in the syncline using dip information

from the area. Uncertainty related to the exact dip angle at the location of the sample and geometry of the syncline along strike results in a sample placement error of ±500 m. The geochronology sample from the AP is a single tuff that was collected in conjunction with a measured section from the base of the Totora Formation in the eastern limb of the Corque Syncline (Kennan et al., 1995). The sample site was near the town of Corque, 150 km SSE of our section line. The two biotite K-Ar ages (23.9 ± 1.3 Ma and 23.0 ± 0.8 Ma) are averaged and their ages and associated errors are combined as a single age of 23.5 ± 2.1 Ma (Kennan et al., 1995). Thicknesses of exposed lower Tertiary formations can be quite variable in the AP, thus we locate the sample 5-5.5 km from the top of the entire measured Corque syncline stratigraphic column (Horton et al., 2001; Garzione et al., 2006, Lamb, 2011) and 5 km from the top of the AP stratigraphic section that is produced by the flexural model. A ±500 m uncertainty in sample placement in both the foreland and hinterland stratigraphic columns is assumed due to possible variability in Beni syncline geometry and accurately locating the placement of the AP sample in the modeled stratigraphy. The error in both basin sample locations correlates to a 1 km thick package of modeled stratigraphy, which has different age estimates for the upper and lower boundary of that stratigraphy depending on the model velocities.

Time windows of wedge-top sediment emplacement were determined by assuming deposition must occur after deformation and erosion have impacted the location in the model but before deformation has totally ceased in the area. The lower age limit is set by the magnitude of deformation needed to deform and erode Paleozoic formations to the level of exposed strata preserved immediately below the wedge-top formations. Upper bounds are set by the magnitude of deformation needed to produce proximal deformation that could cause structural damming and facilitate deposition. The age and location of synorogenic sediment place important temporal

constraints on permissible deformation rates, particularly in the variable rate models. The correlation of flexurally modeled basin sediment age and distribution to dated-synorogenic sedimentary rocks and thermochronometer cooling signals allows us to quantitatively correlate exhumation and deposition within a linked FTB foreland basin system as well as use both datasets to determine acceptable rates of deformation (McQuarrie et al., 2008; Robinson and McQuarrie, 2012).

4.0 RESULTS: COPACABANA BALANCED CROSS SECTION

4.1 LARGE SCALE MAP PATTERNS

New geologic mapping of the region highlights changes in the width of tectonomorphic zones, exposure of Ordovician age rocks in the SA and differences in the rock formations preserved in the EC backthrust zone between the Beni and Copacabana cross section lines. The exposure of Ordovician rocks in the SA frontal thrust sheet in the north, in contrast to Devonian to Mesozoic units in the south, accompanies a shift in the frontal thrust towards the foreland (Fig. 3). Increased width of the IA in the north (along the Copacabana section) displays a gradual change from lower Paleozoic units exposed in the EC to Tertiary filled synclinal basins in the SA. Ordovician rocks exposed in the EC backthrust belt decrease in width towards the north associated with the loss of Triassic plutons. Increased thickness and exposure of upper Paleozoic and Mesozoic formations in the EC backthrust belt becomes important to the north and east of Escoma, as identified in both field and spectral lithology mapping. Precambrian rocks covered by Cretaceous and Cenozoic formations outcrop 60 km southwest of Copacabana indicating an absence of Paleozoic strata in this region of the AP. The large-scale geologic map patterns show a northward decrease in width of exposed lower Paleozoic rocks in the EC, increased width of the IA and narrower Tertiary synclines in conjunction with the appearance of Ordovician formations in the SA.

Foreland and hinterland wedge-top formations and perched, low-relief, paleo-landscapes are preserved in the EC of both sections and decreased in abundance towards the north. The Cangalli Formation is preserved along the Beni section, and between the sections, but pinches out or has been eroded before directly intersecting the Copacabana section line (Fig. 4). The EC back thrust belt contains the Oligocene Penas and Aranjuez Formations (27-25 Ma) between the cross sections, which are slightly younger but broadly syndepositional with the Salla Formation (29-24 Ma), located south of the Beni section (Murray et al., 2010; Leier et al., 2010). The northward younging of Oligocene formations indicate deformation may have occurred slightly later in the north but was largely synchronous. Low-relief paleo-landscapes are preserved in the EC intersecting both cross section lines but are larger and more frequent in the south (Fig. 6) (Whipple and Gasparini, 2014). The age and preservation of the wedge-top formations and erosional surface units links kinematic evolution of these two cross sections and impart geometric constraints on the location of the modern decollement ramp.

4.2 STRUCTURAL GEOMETRY

The depth of the Beni Basin is interpreted to be 4.5-5.0 km at the frontal thrust at Tumupasa with a basal decollement angle of 4°. The SA is characterized by the large (~25 km) open Madidi Syncline and tight (3-5 km) variably thrust faulted anticlines along its western edge. Ordovician rocks that outcrop along the frontal thrust indicate a detachment horizon at the base of the Paleozoic column accommodating recent SA displacement. The relatively shallow (3-4 km) Madidi Syncline is supported by stacked thrust sheets along its western limb (Gil, 2002) (Fig. 10). The gradual change from Tertiary sediments in the SA to lower Paleozoic rocks in the

IA is interpreted to be a result of an increase in basement thrust sheet involvement and duplexed Paleozoic formations A detachment at the base of the Devonian is needed to account for the repetition of Devonian through Carboniferous age rocks at the surface across the IA and indicates the need for a duplex in Ordovician-Silurian age rocks to accommodate similar magnitudes of shortening in these formations. The involvement of basement sheet B in the IA is used to fill space between the depth of the decollement (projected at a 4° dip from the foreland) and the Devonian rocks exposed at the surface (Fig. 10). The magnitude of displacement on the basement thrust sheet equals the shortening in the Ordovician and younger units to the east of it in the SA zone. The narrower wavelength structures in the western IA is accommodated by a decrease in length of Ordovician and Silurian horses. The EC is characterized by an Ordovician section that preserves eastward and westward verging thrusts, and the upper Paleozoic-Mesozoic backthrust zone that contains broad (20-30km) wide synclines and tight (1-5 km) anticlines. In the eastern portion of the EC the preservation of low-relief landforms in conjunction with stream indices analysis suggests the presence of a deep monoclinal structure in the decollement, interpreted to be the SA footwall ramp. The location of the ramp near the axis of vergence in the EC (Fig. 6 and Fig. 3) (Whipple and Gasparini, 2014) is consistent with the shear velocity model profiles, which shows a step in velocity structure in the central EC (Fig. 7). Shortening in upper Paleozoic and Mesozoic formations in the EC backthrust is balanced by an Ordovician backthrust duplex that is subsequently cut by late-stage faulting. Changes from upper to lower Paleozoic exposures in the EC backthrust zone suggest a long-wavelength (25-50 km) structural feature, which we interpret as a change in the depth to basement. The basement structures that accommodate the long-wavelength features are out-of-sequence basement thrust faults that facilitate the tightening and faulting of the EC Ordovician backthrust duplex. The outcrop of

Cretaceous covered Precambrian units in the AP place basement thrust sheets near the surface and mandates the pinching out of the Paleozoic column beneath the eastern AP. Shortening in the AP is less along the Copacabana section and is restricted to displacement along; the west verging fault that cuts the southern extent of Lake Titicaca; the east verging fault that exposes Cretaceous rocks at the southeastern margin of the Lake and the west verging fault that places Eocene rocks on Miocene units west of the line of section. The large step (~12 km) in structural elevation from the EC to the AP is similar to the Beni section and is interpreted to be the result of basement thrust sheet stacking. The Copacabana cross section displays the decrease in AP shortening, change in structural development of the EC, increased width of the IA, and decreased width of the SA moving north in Bolivia.

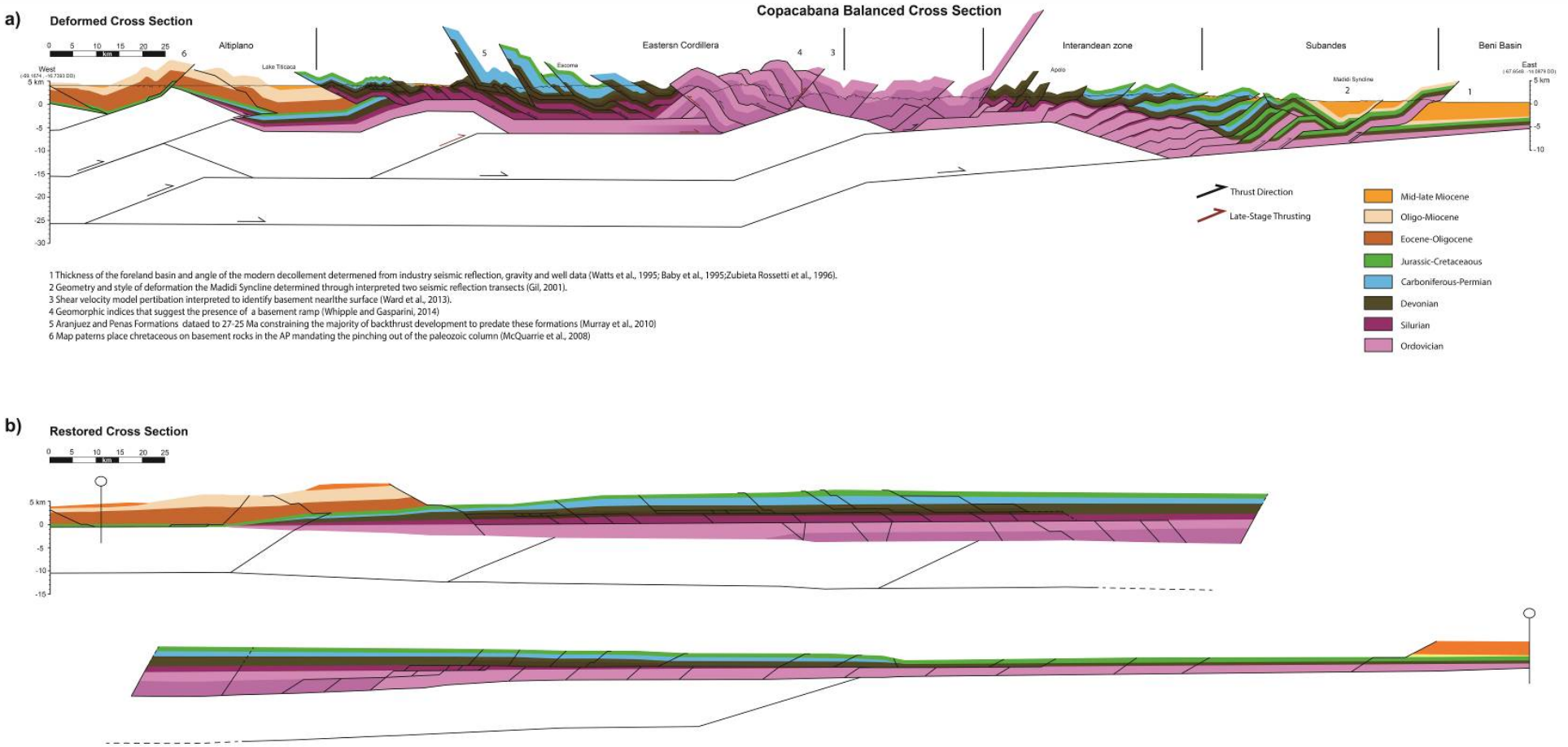

Figure 10. Copacabana balanced cross section with the deformed cross section (a) and the restored cross section (b).

4.3 SHORTENING

The total shortening across the northern Andean FTB along the trend of the Copacabana balanced cross section is 242 km. This study agrees with previous interpretations of a sequential increase in the magnitude of shortening towards the south to as high as >320 km south of the Santa Cruz bend in central Bolivia (McQuarrie, 2002; McQuarrie et al., 2008, Eichelberger et al., 2013). The restored cross section is 562 km indicating 43% total shortening similar to cross sections to the south (~40%) (McQuarrie, 2002; McQuarrie et al., 2008; Eichelberger et al., 2013). Total SA shortening along the section is 68 km and is fed by the displacement of basement sheet B. This represents 46% shortening in the SA along the Copacabana cross section, which is greater than the percent shortening interpreted in the SA of the Beni section (66 km and 40% shortening in the SA) (McQuarrie et al., 2008). Shortening in the IA was determined to be 53 km, a slight increase in shortening towards the north when compared to the Beni section (48 km). Total shortening in the EC and IA of 164 km is fed by displacement of the first basement thrust sheet (A) and is less than the 178 interpreted along the Beni cross section (McQuarrie et al., 2008). Late-stage faulting of thrust sheet A (11 km) is included in the total magnitude displacement of thrust sheet A (above; red arrows Fig. 10). Shortening in the EC is divided into 42 km of forethrusting, 58 km of back thrusting, and 11 km of late-stage faulting each contributing to the 111 km of total EC shortening. Shortening in the AP is low (10 km) but only accounts for shortening on the eastern edge of the AP.

5.0 RESULTS: FLEXURAL AND THERMAL MODELING - BENI SECTION

5.1 ISOSTATIC MODELING

Isostatic loads in the model are dictated by the location and magnitude of shortening, crustal density, EET evolution, and the proposed topographic evolution. Multiple iterations of the flexural model were run to evaluate the parameters needed to most accurately reproduce the exposed surface geology, the depth of the foreland basins and the dip of the modern decollement by adjusting crustal density and EET in each scenario. Throughout the isostatic modeling process topography evolves with topographic angles on east facing slopes ranging from 1-4^0 in the EC and WC. Topography along the western edge of the EC was generated as material moves over the basement footwall ramp of thrust A, however upper elevations were limited to no greater than 5-6 km. On the eastern side, model topography was limited to a max elevation of ~6 km with isolated peaks reaching as high as 7.6 km during formation of the EC Ordovician duplex to minimize erosion in this region. Flexural evolution of the cross section was varied with an overall increase in EET through time (from ~30 to ~90 km) with a constant Young's Modulus of 70 GPa. During the emplacement of the first basement thrust sheet, EET was kept low to preserve Ordovician units exposed at the surface, but systematically increased throughout the model to enhance the amount of sediment accumulation in flexural basins. Models with low EET (30-70 km) did not preserve significant sediment in the modeled foreland basins until late in the

model due to the short flexural wavelength in these scenarios. Initial modeling with crustal densities of 2750 kg/ km^3 did not produce the thick packages of foreland and hinterland basin sediments presently preserved in the orogen. Models using higher crustal densities (2900 kg/km^3) in conjunction with increasing EET from 30-90 km through model time were used to produce the deepest foreland basin possible, but SA synclines were still 2 km too shallow. Additionally, topography in the EC and AP was significantly (> 3 km) lower than modern topography due to its proximity to thrust-loading throughout the model. Vertical, long-wave uplift and subsidence was applied to the EC and foreland respectively after the initiation of basement thrust sheet B, and synchronously with major SA shortening. The long-wave uplift and subsidence had wavelengths of 400-600 km and an amplitude of ~500 m incremental elevation increase in the EC and AP and ~350 m of incremental subsidence of the foreland basin. A total of -2.2 km was imposed in the foreland and a positive 3.9 km was imposed in the hinterland with inflection occurring at the SA-IA contact (Fig. 11).

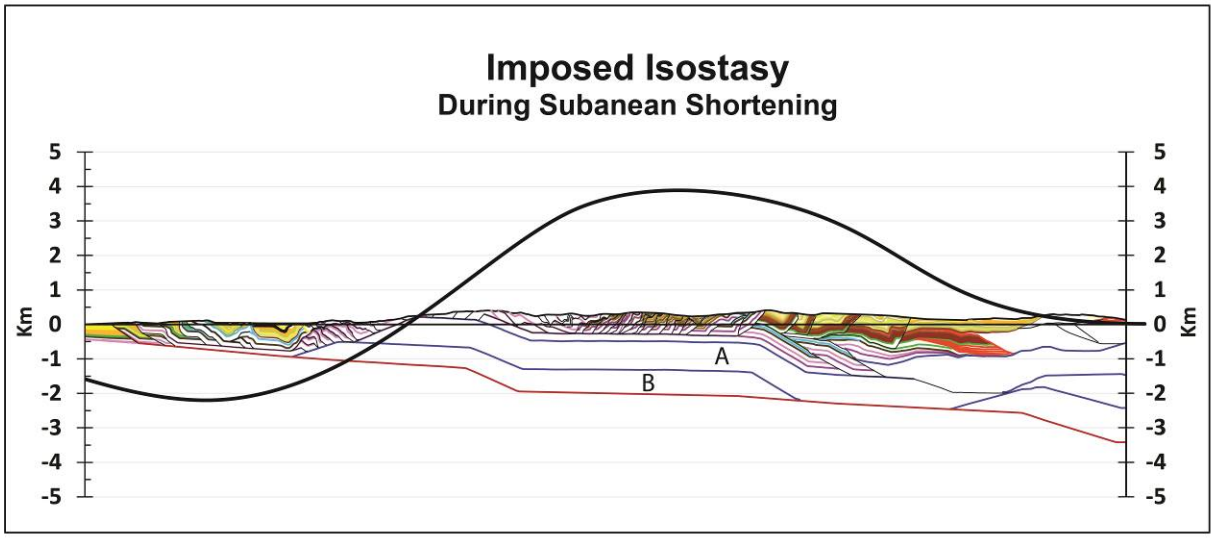

Figure 11. Magnitude of imposed flexure during isostatic modeling of the Beni cross sections applied synchronously with the emplacement of basement thrust sheet B.

5.2 INITIAL KINEMATIC MODEL

The effects of thrust belt geometry on exhumation, predicted thermochronometer cooling, and sedimentation are described for the kinematic model proposed by McQuarrie et al., (2008). At 45 Ma, the emplacement of basement thrust sheet A focused exhumation above footwall and hangingwall basement ramps, reset thermochronometers and produced flexural basins. The initial modeled U-shaped cooling patterns above basement ramps (after 26 km of displacement) (Fig. 12b) display age patterns that are the youngest at the top of the basement footwall ramp and show a gentle increase in age towards the tip of the hanging wall ramp before the steep increase in ages that represents a suite of partially reset to non-reset ages. As basement sheet A continues to be emplaced two U-shaped curves grow as a result of motion of material over the footwall ramp in the west and the hanging wall ramp in the east (Fig. 12c and 12d) the oldest ages (indicating ages of initial thrusting) are centered on the EC and young towards the west and east (Fig. 12e, 25 Ma). Sediment accumulated in flexural basins adjacent to thrust faulting is eroded and redeposited farther away from the initial locus of deformation in the EC. Isostatic loading of the model depresses the modeled grid in the foreland basin with respect to the topographic surface, imparting unique thermal histories to these points. The activation of thrust sheet B focused exhumation above the new basement ramp and in select SA thrust sheets in front of the basement thrust sheet (Fig. 12f, 14 Ma). Material is rapidly collected in the foreland basin as long-wavelength subsidence is imposed. The emplacement of the basement sheet B resets lower temperature AFT and A/He systems above its footwall ramp, which moves west relative to the pinned foreland basin (Fig. 12g, 6 Ma). Synclinal basins fill as isolated fault sheets reach the erosional surface in the SA. At the final model step (Fig. 12h, time 0), low temperature AFT and A/He systems are variably reset in the SA thrust sheets and display a younging trend from the IA

to the active ramp under the EC. The predicted cooling spectra display the oldest reset ages in the center of the EC and younger ages to both the east and west producing a prominent triangle reset pattern. The pattern is a direct consequence of motion of rocks over the significant hanging wall and footwall ramps of basement thrust sheet A. The young AFT and A\He predicted cooling signatures in the eastern EC increase in age towards the IA and are the result of material moving over the footwall ramp associated with basement sheet B. The youngest reset AFT and A\He ages in the SA are located at the base of thrust sheets that have been significantly eroded.

The youngest predicted AFT ages in the EC are not co-located with the young AFT measured ages in that region (Fig. 12i). The predicted young AFT ages are >10 km to the east and indicate the active ramp must be located west of its interpreted location. The simplest way to move the footwall ramp west is by increasing shortening in the SA, thus increasing the displacement over the ramp. A modified kinematic scenario, where increased shortening in the SA facilitates the westward movement of the decollement ramp, was developed to match thermochronometer cooling data in the EC.

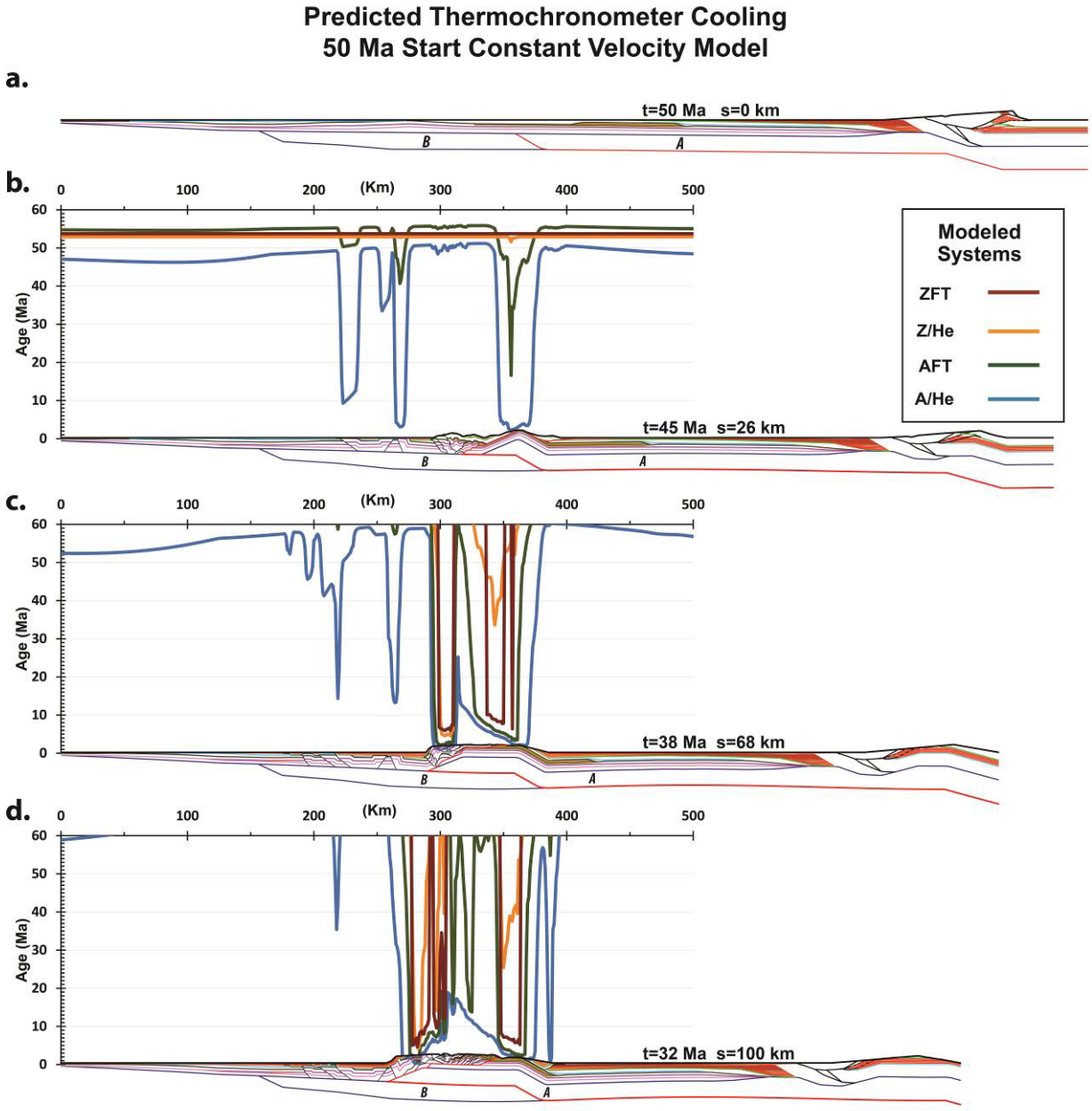

Figure 12. Structural, geomorphic, and thermochronometric evolution diagram for of the northern Bolivian FTB using kinematic scenario 1 (McQuarrie et al., 2008).

Figure 12 continued.

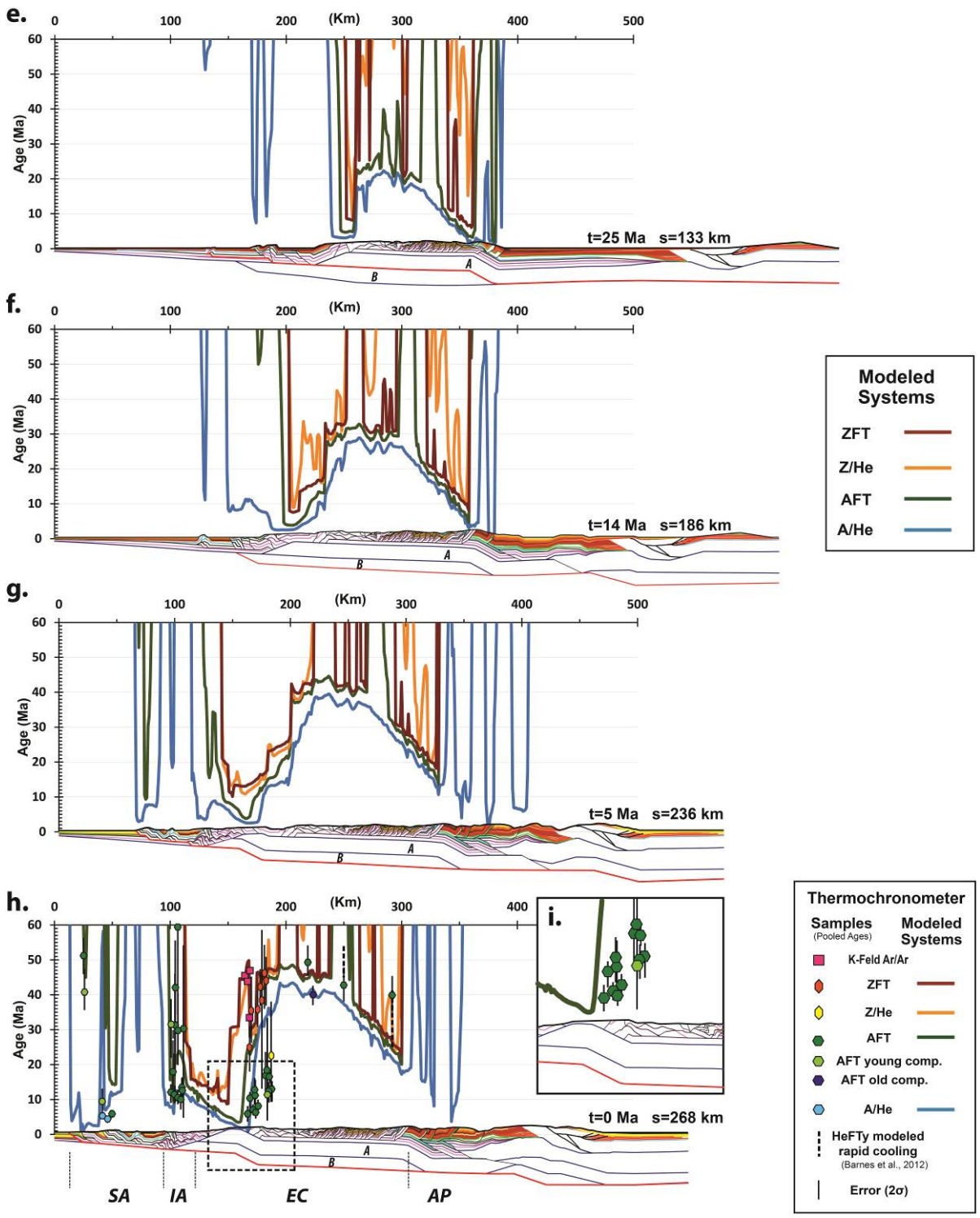

5.3 REVISED KINEMATIC MODEL

Kinematics proposed by McQuarrie et al., (2008) were altered to enable the westward shift of the basement decollement ramp. Westward movement of the active basement ramp was facilitated by both increasing SA shortening by 14 km and increasing the total amount of displacement on basement thrust B. Increased slip must be distributed to SA thrust sheets that do not have preserved hanging wall ramps, allowing for additional fault motion at these locations. Two kilometers or less displacement was added to other thrust structures in the SA to fully account for the extra 14 km of shortening. Revised total shortening along the kinematically modeled Beni balanced cross section is 282 km. The kinematics and associated erosional exhumation are similar to those described in initial kinematic model section (above) with the exception of an increase in exhumation in the eastern EC and on select SA thrust sheets. The increased shortening causes additional material to move over the active ramp in the EC and extends the young predicted AFT trend farther west (Fig. 13). In addition, the increased shortening in the SA causes younger predicted A/He ages in that region. Velocity models presented (below) utilize the revised kinematic scenario model for thermokinematic modeling.

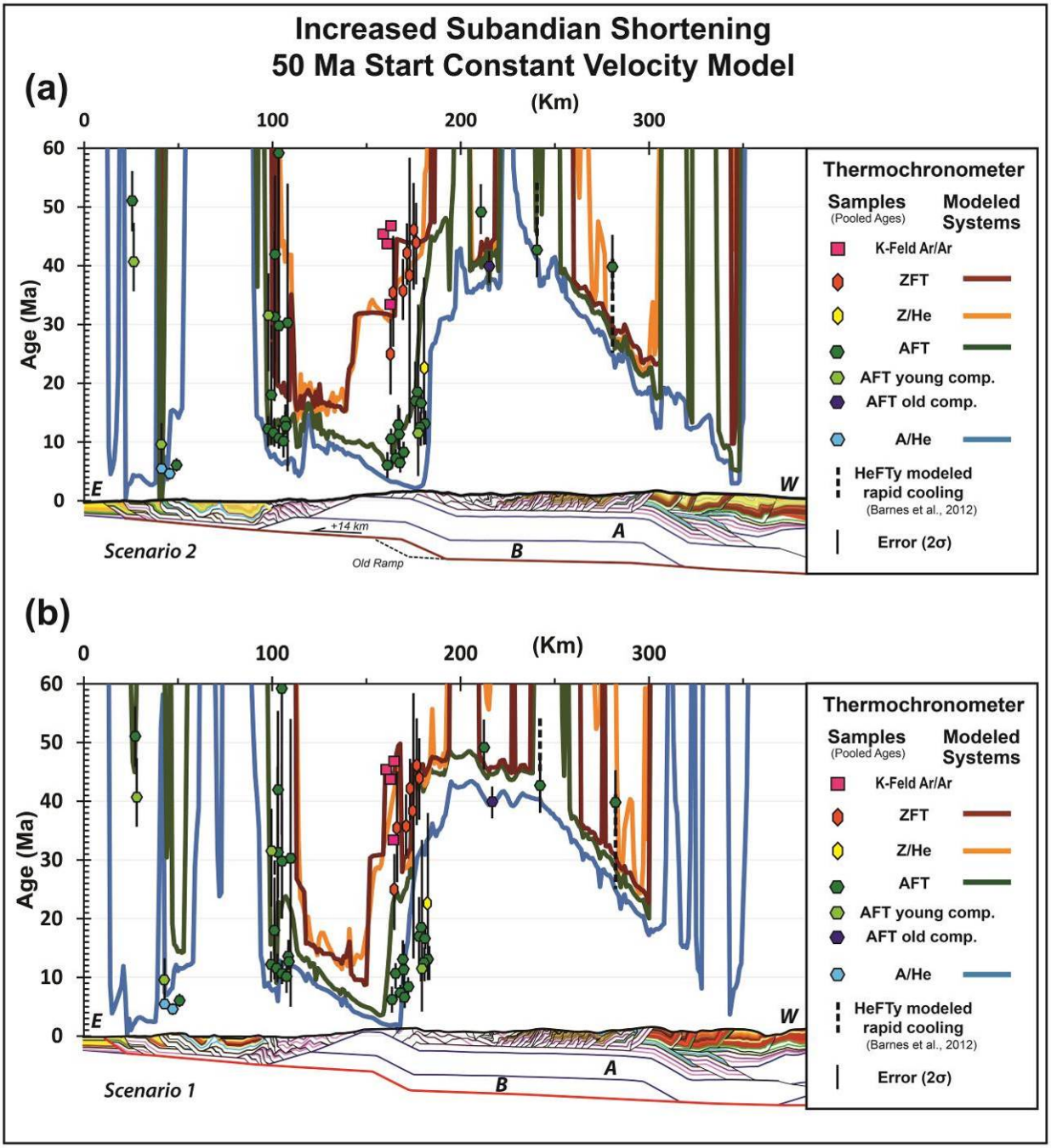

Figure 13. Predicted thermochronometer cooling spectra with scenario 1 (a) after McQuarrie et al., (2008) and scenario 2 (b) (14 km increased SA shortening). Difference in cooling trends at 150-175 km is related to the motion of increased material of the footwall ramp in scenario 2.

5.4 MODELED AGE OF INITIATION

An optimal onset of deformation was determined by testing constant-rate velocity models with different age starts (30-55 Ma) and comparing predicted thermochronometer cooling signatures and modeled chronostratigraphy to published datasets. Rates of shortening decrease with increasing age of initiation, ranging from 5.1-9.4 mm/yr (Fig. 14). Thermochronometer plots and deformation-magnitude plots are described for each velocity scenario to demonstrate the ability of the model to match chronologic datasets form the study region. Ages from three Z/He dated grains from a single sample (Barnes et al., 2006) were averaged and their errors were combined to a single Z/He data point in the eastern EC. Thermochronometer samples, with their 2σ error, have been plotted along the modeled line of section with dashed lines representing times of rapid cooling identified in HeFTy models (Table DR3 AFT good fits, Barnes et al., 2012) and are compared to predicted cooling signatures. Thermochronometer plots use a 1 Ma thick line for predicted cooling signatures and illustrate the match between modeled cooling signatures, 2σ errors of samples and HeFTy modeled rapid cooling along the modeled cross section. Predicted cooling of specific thermochronometer systems are described as: an optimal fit if they intersect the 2σ error of samples and HeFTy modeled cooling windows in a specified region; a good fit if they miss 1 of the samples, a moderate fit if they miss 2 of samples; and poor if they miss 3 or more of the samples. Dense data areas, like the EC and IA, are described by the percentage of data (within the 2σ error and HeFTy modeled cooling) that the predicted cooling signature intersects.

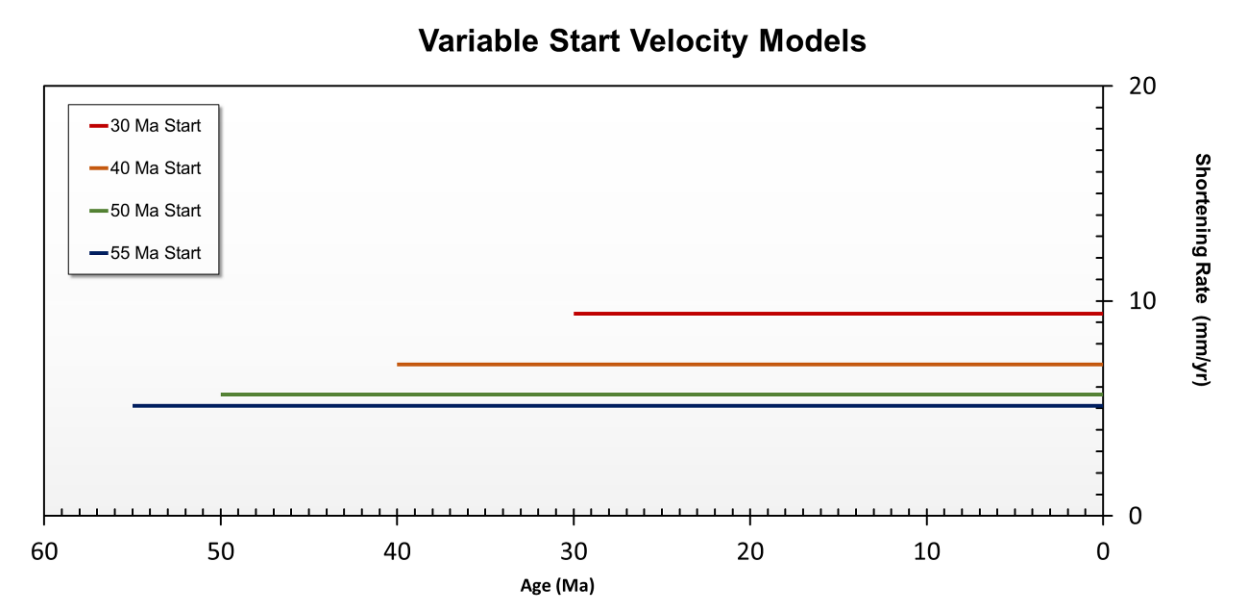

Figure 14. Variable start date velocity model plot illustrating the increase in deformation rate with younger modeled initiation dates.

Synorogenic sediment data are plotted on deformation-magnitude versus time plots and are divided into wedge-top or basin sediment geochronology. Uncertainty in the location of basin samples in the modeled stratigraphy results in a 1 km thickness in which the samples are assumed to be located. Velocity models are characterized as matching basin geochronology if any of the predicted modeled basin ages within the 1 km thick section of modeled basin stratigraphy, 500 m above and below the assumed sample location, matches the measured geochronologic ages of 23.5 ± 2.1 Ma for the AP (Kennan et al., 1995) and 22.1 ± 0.18 Ma for the SA (Mosolf et al., 2011) (Green box shows foreland error envelope Fig. 15). Velocity models are described as matching the wedge-top sediment data if geochronology samples fall between deformation-induced erosion of the unit below the formation and prior to the cessation of local deformation in the area. Two interbedded tuff samples from the Cangalli Formation (9.16 ± 0.07 Ma and 7.41 ± 0.52 Ma; Mosolf et al., 2011) indicate the upper Ordovician formations must have been previously eroded before that time. Two interbedded tuff samples form the Salla Formation

were dated to 28 ± 0.68 Ma and 24.59 ± 0.39 Ma (Gillis et al., 2006) and indicate that the Mesozoic and upper Paleozoic rocks were eroded before 28 Ma. The upper bound is set by the last pulse of deformation needed to provide localized structural damming adjacent to where wedge-top formations are located (Fig. 16). The flexural model does not reproduce wedge-top formations but defines windows in which formations could be deposited and uses these windows as additional chronologic constraints for testing velocity models. Together, predicted thermochronometer and deformation-magnitude plots are used to evaluate rates of deformation modeled in this study.

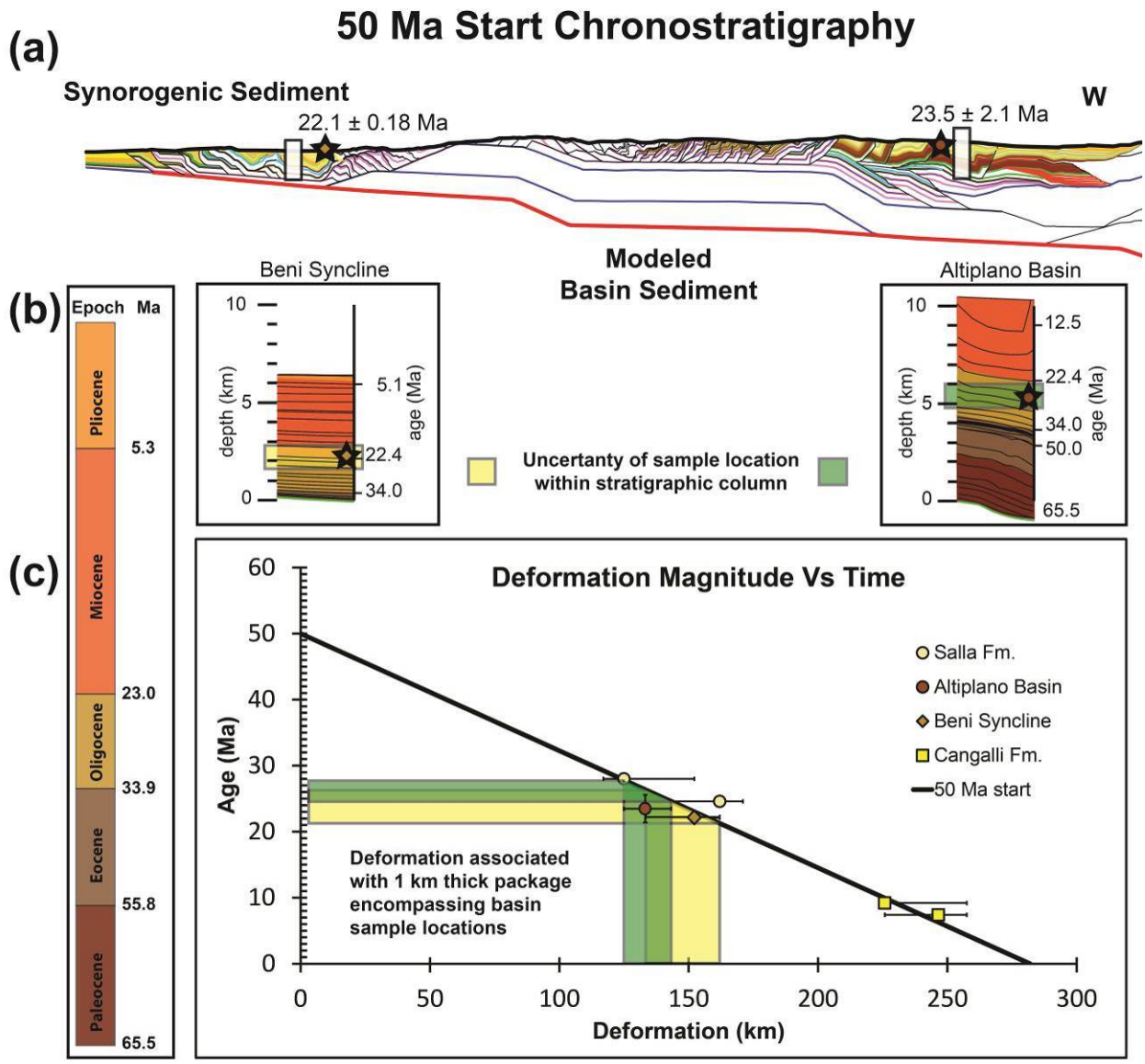

Figure 15. Basin sediment correlation diagram showing uncertainty envelopes associated with each sample for the 50 Ma start. Deformed, modeled cross section (a) (scenario 2) with the locations and ages of basin geochronology samples (stars) and the location of modeled chronostratigraphic sections (white rectangles) displayed below. Modeled chronostratigraphy (b) form the SA and the AP with uncertainty envelopes associated with each sample (green and yellow boxes) and Cenozoic timeline for reference. Deformation magnitude plots (c) with deformation interval and time interval, for the 50 Ma constant velocity model, associated with each basin sample.

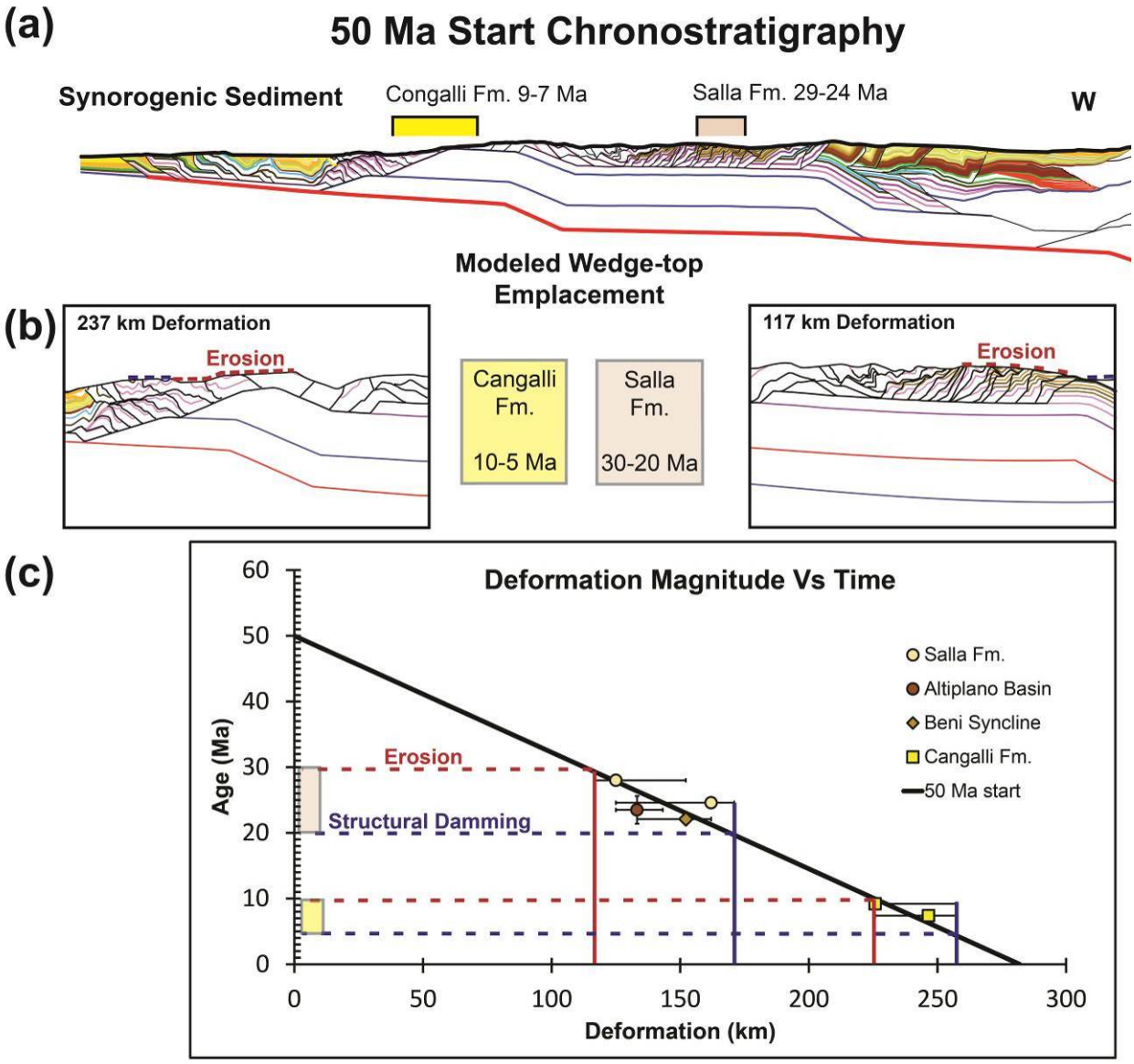

Figure 16. Wedge-top correlation diagram showing acceptable deformational windows for each sample for the 50 Ma constant velocity model. Deformed, modeled cross section (a) (scenario 2) with the locations and ages of wedge-top sediments. Images of model after specified amounts of deformation (b) showing the erosion of units (red) and the location of subsequent structural damming (blue). Deformation magnitude plots (c) describing acceptable wedge-top deposition windows for the 50 Ma constant velocity model.

5.4.1 50 Ma Start

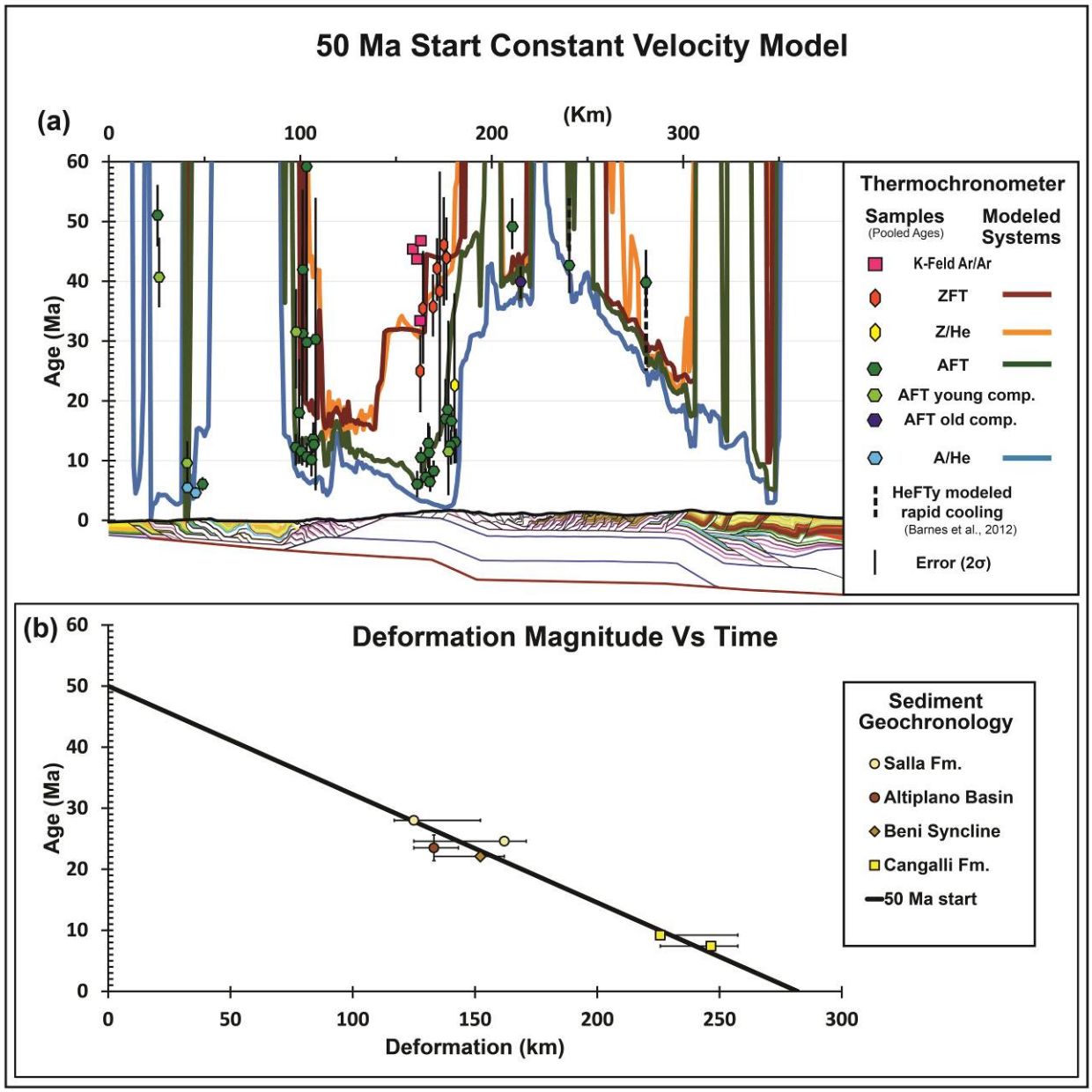

Figure 17. 50 Ma constant velocity model thermochronometer plot (a) and deformation magnitude plot (b).

Cooling signals show an optimal fit with A/He samples and a good fit with AFT samples in the center portion of the SA (Fig. 17a at 50 km) but an overall poor fit when including easternmost AFT samples at 25 km. Here modeled A\He is reset but there has not been enough

exhumation to predict partially reset AFT cooling ages that match the measured young component or pooled ages of 35-55 Ma. Cooling of AFT samples in the IA range from reset (~10 Ma) to partially reset (31-77 Ma). Although predicted AFT cooling ages only intersect 8 of the 13 measured AFT samples (62%), the remaining 5 samples fall within a cooling envelope between A/He and Z/He cooling signatures. Cooling signatures in the eastern EC intersects 54% of the AFT and 71% of the ZFT data, while missing the Z/He sample. Predicted AFT cooling ages in the western EC show a good fit to sample data, intersecting three of the four samples. The 50 Ma start constant velocity model accurately predicts old AFT cooling in the EC backthrust belt and fits most of the ZFT data in the EC.

Predicted basin and wedge-top sediment ages agree with measured ages in the 50 Ma velocity model (Fig. 17b). Upper Paleozoic strata in the Salla region of the EC backthrust belt are eroded by 29 Ma, predating the oldest depositional age of the Salla Formation (28 Ma). Structural damming persists until 20 Ma as final thrusting along the westernmost EC backthrust occurs. Erosion of Ordovician units upon which the Cangalli Formation is deposited occurs at 10 Ma with a final structural damming age of 4 Ma agreeing with the 9-7 Ma geochronology from the formation. The upper and lower ages predicted 500 meters above and below the SA geochronologic sample are 26 Ma at the bottom and 21 Ma at the top, encompassing the 22 Ma measured age from the Beni Syncline. The age window linked to the 1 km error associated with the AP sample is 28-24 Ma and encompasses the AP geochronologic measured age (23.5 ± 2.1 Ma). The deformation magnitude plots indicate that the 50 Ma start constant velocity model can accurately reproduce dated synorogenic sediment along the modeled section.

5.4.2 40 Ma Start

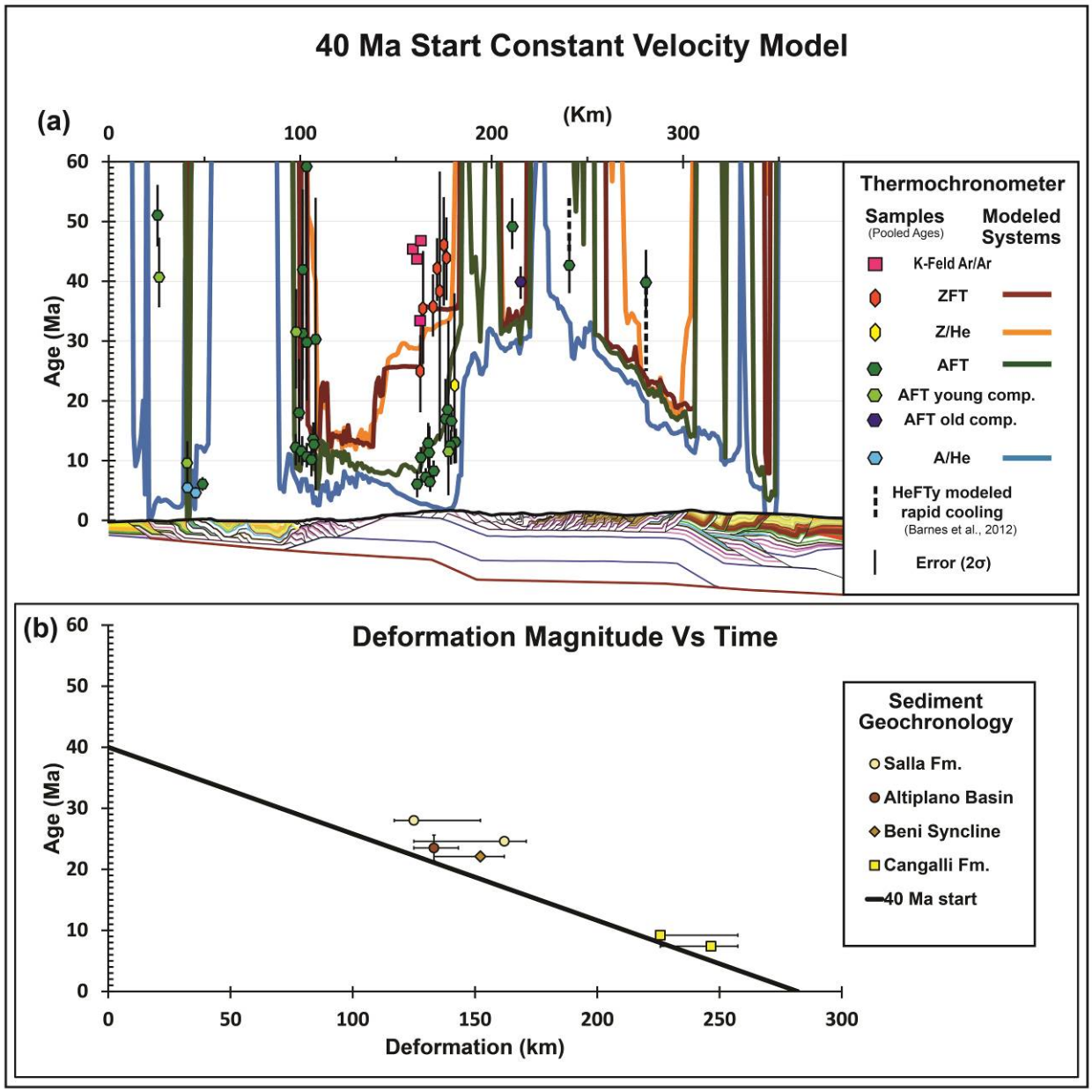

Figure 18. 40 Ma constant velocity model thermochronometer plot (a) and deformation magnitude plot (b).

Cooling signals in the SA are nearly identical to the 50 Ma start constant-velocity model and have the same optimal and poor fits to the measured A/He and AFT samples (Fig. 18a). Predicted cooling of the AFT system in the IA intersects 7 of the 13 (54%) samples and predict a

cooling window between AFT and Z/He that encompasses the remaining 6 AFT samples. The eastern EC predicted AFT cooling intersects with 46% of the data and ZFT predicted cooling intersects 57% of the sample points, while predicted Z/He intersects the measured sample. In the western EC predicted AFT cooling signatures fit poorly and miss all four of the AFT samples. Modeled AFT cooling in the EC backthrust is predicted to be 5-10 Ma too young with a 40 Ma start velocity model.

Predicted basin ages and wedge-top sediment depositional windows with the 40 Ma velocity model are dominantly too young and do not agree with sample data. Age of predicted erosion of Paleozoic strata in the Salla region of the backthrust belt is significantly later (22 Ma) than the 28-24 Ma age of the unit. Erosion of Ordovician in the location of the Cangalli Formation is slightly too young (8 Ma) compared to the earliest geochronologic age (9 Ma) of the formation but does overlap the younger age (7.4 Ma). The age window associated with the SA sample is 21-16 Ma, younger than the Beni syncline geochronologic sample by >1 Ma. The age envelope associated with the 1 km sequence in the AP is 22-20 Ma, which falls within the lower error bounds of the measured age (23.5 ± 2.1 Ma). Deformation magnitude plots show that the 40 Ma start constant velocity model does not match wedge-top sediment or the Beni Syncline geochronologic constraints (Fig. 18b).

5.4.3 30 Ma Start

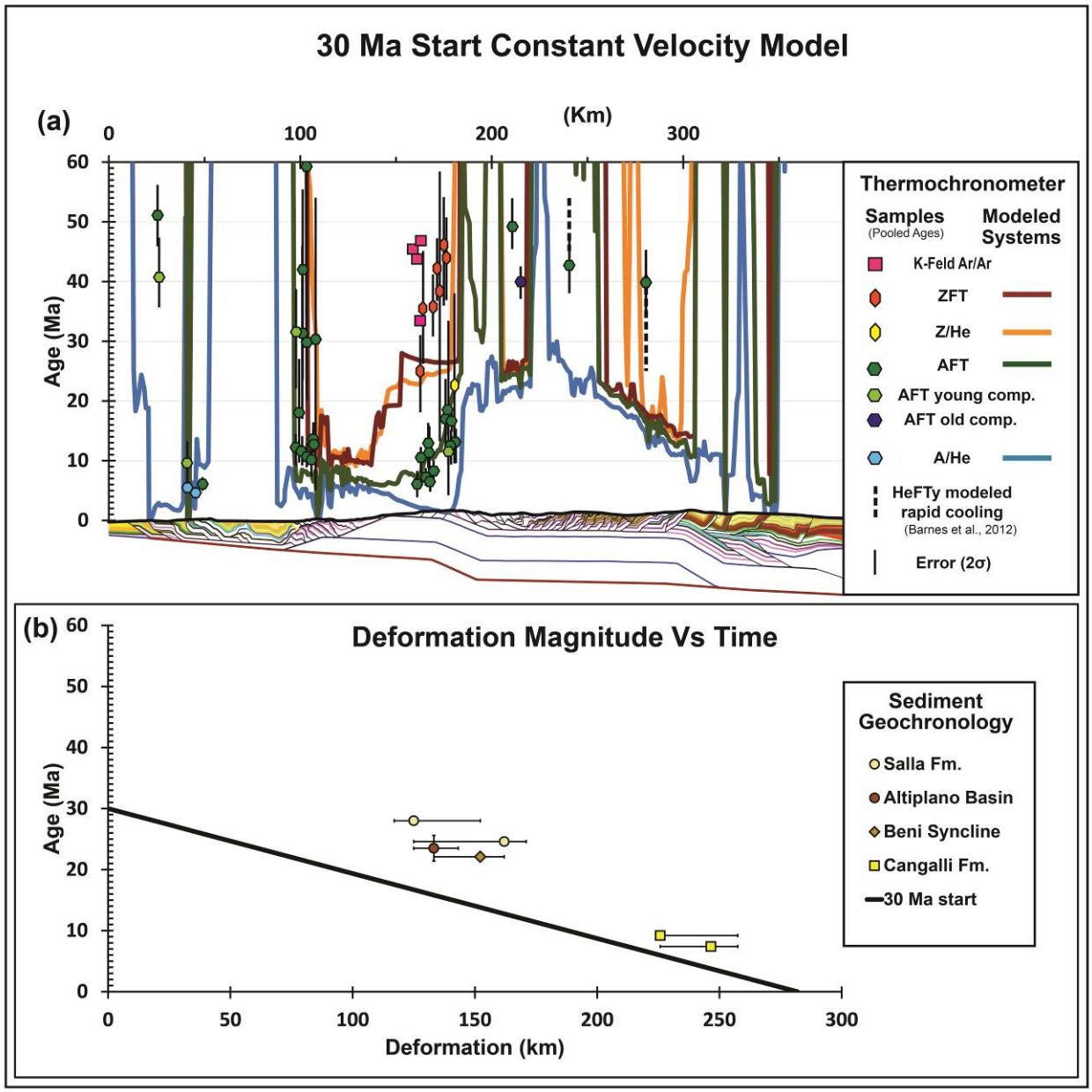

Figure 19. 30 Ma constant velocity model thermochronometer plot (a) and deformation magnitude plot (b).

Cooling signals in the SA show a slight broadening of the A/He signature but remains similar to the 50 and 40 Ma start models showing an overall optimal fit to the A/He samples and a poor fit to the AFT samples (Fig. 19a). Despite the higher rate of deformation, the rate of

exhumation in the SA is still insufficient to reset the AFT system in the eastern most SA. With the younger start, AFT cooling ages in the IA only intersect 5 of the 13 (38%) measured AFT ages, but the remaining samples still fall within the cooling envelope between Z/He and AFT signatures. In the eastern EC predicted AFT cooling intersect 77% of the data, ZFT predicted cooling intersect 29% of the sample ages, and Z/He cooling intersects the measured age. While the younger predicted AFT ages in the eastern EC (for the 30 Ma start model) intersect 23% more data than the 50 Ma start, the ZFT predicted cooling becomes too young and intersects 42% less data compared to the 50 Ma start model. Similar to the 40 Ma start model, western EC predicted AFT cooling signatures fit poorly and do not predict any of the AFT samples in the EC backthrust belt. Modeled AFT cooling in the EC backthrust is predicted to be >10 Ma too young while predicted ZFT cooling in the EC is 10-20 Ma too young.

Modeled sediment ages from the 30 Ma velocity model do not match wedge-top or basin chronostratigraphic constraints. Erosion of Paleozoic strata in the Salla region of the backthrust belt is much younger (18 Ma) than the earliest depositional age of 28 Ma reported from the unit. Erosion of the Ordovician unit in the eastern EC occurs too late (6 Ma) for both depositional ages (9 and 7 Ma) of the Cangalli Formation. The age window associated with the SA sample is 16-13 Ma, much younger than the Beni Syncline sample age. The age envelope associated with the AP sample is 17-15 Ma and is also significantly younger than the age of the geochronologic sample from the Corque Syncline. The deformation magnitude plots indicate that the 30 Ma start constant velocity model predicts very young deformation, erosion and sedimentation throughout the system that does not match basin or wedge-top geochronology data (Fig. 19b).

5.4.4 55 Ma Start

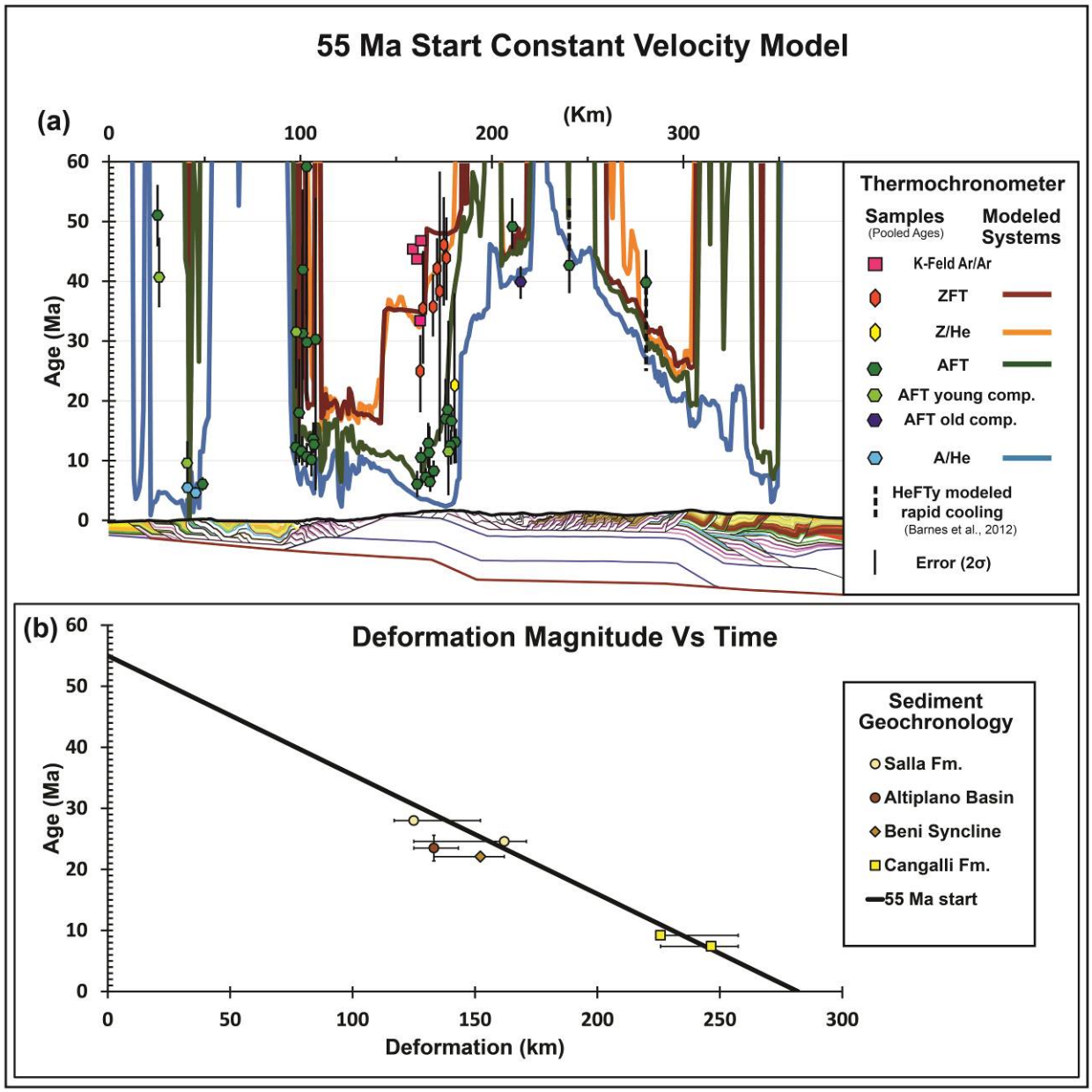

Figure 20. 55 Ma constant velocity model thermochronometer plot (a) and deformation magnitude plot (b).

Similar to the 40 and 50 Ma start dates, cooling signals in the SA show an optimal fit to A/He samples and a poor fit to AFT samples (Fig. 20a). The broadening of cooling signatures is evident by the increase in partial reset AFT and A/He signatures at 50 km. Changes in SA

cooling signatures with this older start-date model indicate samples that experience long residence time in the subsurface may be influenced by protracted thermal histories such as age and rate of basin formation. Predicted AFT cooling ages in the IA intersect 54% of the AFT sample while the remaining 6 samples fall within a cooling envelope between A/He and Z/He cooling signatures. Cooling signatures in the eastern EC intersect 54% of the AFT and 57% of the ZFT data, while missing the Z/He sample. Predicted AFT cooling in the western EC shows a good fit to the plotted samples by intersecting three of the four AFT samples. The 55 Ma start constant velocity model accurately predicts old AFT cooling in the EC backthrust belt and reasonably fits the ZFT data.

Predicted wedge-top sediment ages in the 55 Ma start constant velocity model agree with sample data while predicted basin ages are older than sediment geochronology data. Age of predicted erosion of Paleozoic strata in the Salla region of the backthrust belt occurs at 32 Ma prior to the earliest depositional age of the hinterland wedge-top formation. Final structural damming in the region occurs at 22 Ma postdating the youngest depositional age of the Salla Formation (24 Ma) matching the measured depositional window for the Salla Formation. Erosion of Ordovician rocks in the eastern EC at 11 Ma predates the oldest depositional age of the Cangalli Formation (9 Ma) with structural damming in the region persisting till 5 Ma. The age envelope associated with the SA sample is 29-23 Ma, 1 Myr older than the Beni syncline sample age. The chronologic range linked to the AP sample is 31-27 Ma and is also older than the sample age (23.5 ± 2.1 Ma). The deformation magnitude plots show that the 55 Ma constant velocity model can reproduce wedge-top chronologies but predicts basin sediments that are too old by 1 Myr or more (Fig. 20b).

5.5 MODELED VARIABLE RATE OF DEFORMATION

5.5.1 Step Function Hiatus Models

A best-fit step function variable rate of deformation was determined by analyzing predicted thermochronometer cooling signatures and chronostratigraphic features produced by models with variable rates of deformation that start at 55 Ma. A preferred start date of 55 Ma was used for step function variation hiatus models to match old AFT samples in the EC and maximize possible SA AFT partial resetting. All step function deformation rate models are the same from 55-25 Ma with a rate of 4.8 mm/yr and only diverge in rates of deformation from 25 Ma onward (Fig. 21; dashed yellow, orange and red lines). The difference in the length of time of the hiatal period, from 10-17 Ma, essentially changes the initiation of SA deformation from 15 Ma to 8 Ma. The rate of deformation in the SA is controlled by the time window in which deformation occurs (15-0 Ma, 12-0 Ma or 8-0 Ma) and the hiatus models induces rates that vary between 7.0-13.0 mm/yr. The rate of deformation during the hiatal period also varies with each model from 3.4-2.0 mm/yr (Fig. 21). Differences in chronology over the past 25 Ma are unique to each model and are specifically scrutinized.

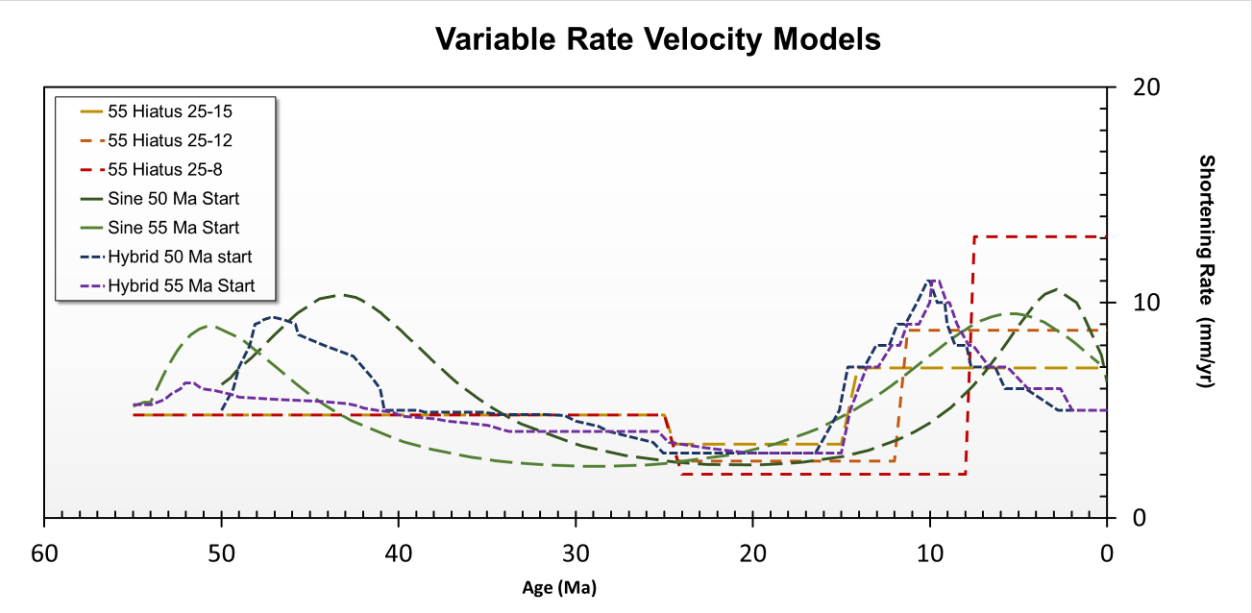

Figure 21. Variable rate velocity model plot illustrating the rates of deformation through time for the hiatus, sine and hybrid velocity models.

Older predicted AFT ages in the western EC and ZFT and Z/He in the EC are described here for the three step function velocity models as this early time window of exhumation is the same in each model. Predicted cooling of AFT systems in the EC backthrust belt shows moderate fits with predicted ages overlapping two of the four AFT samples (Figs. 22a, 23a and 24a). Predicted cooling of the ZFT system in the eastern EC matches 57% of the 7 samples (similar to the constant 55 Ma start velocity model) but retains a mismatch with the Z/He system. Surprisingly, predicted cooling signatures in the SA are similar for all 3 models, retaining an optimal fit to A/He samples and a poor fit to AFT samples. A general younging and westward shift of the A/He signature is evident with longer hiatal periods and increased rates of SA shortening but it does not increase the rate of exhumation enough to partially reset AFT signatures in the westernmost SA thrust sheet (Figs. 22a, 23a and 24a).

Synorogenic sediment ages are similar for each step function hiatus model fitting both foreland and hinterland basin and Salla Formation geochronology and incorrectly predicting the

erosion of Ordovician units in the eastern EC. In all three models erosion of the Paleozoic formations the EC backthrust belt occur at 30 Ma preceding the Salla Formation oldest depositional age. The age window associated with the AP geochronology sample is 28-25 Ma overlapping with the upper age limit of the geochronology sample. The age at the base of the 1 km thick succession associated with the SA geochronology sample is 27 Ma with all 3 hiatal models. The age at the top of the 1 km thick succession associated with the SA sample becomes younger (20-16 Ma) with longer hiatal models, all of which encompass the sample age of 22.1 Ma. In all 3 models, the erosion of the Ordovician rocks in the eastern EC postdates the oldest depositional age of the Cangalli Formation with the largest mismatch resulting from the longest hiatus model (25-8 Ma hiatus). The 25-15 Ma hiatus model predicts the erosion of Ordovician units in the eastern EC at 8 Ma within the bound of the youngest Cangalli Formation sample age (Figs. 22b, 23b and 24b). Deformation magnitude plots show similar fits to geochronologic samples in all 3 hiatus models with an increasing mismatch to the Cangalli Formation with longer hiatus velocity models.

5.5.1.1 55 Ma Start 25-15 Ma Hiatus

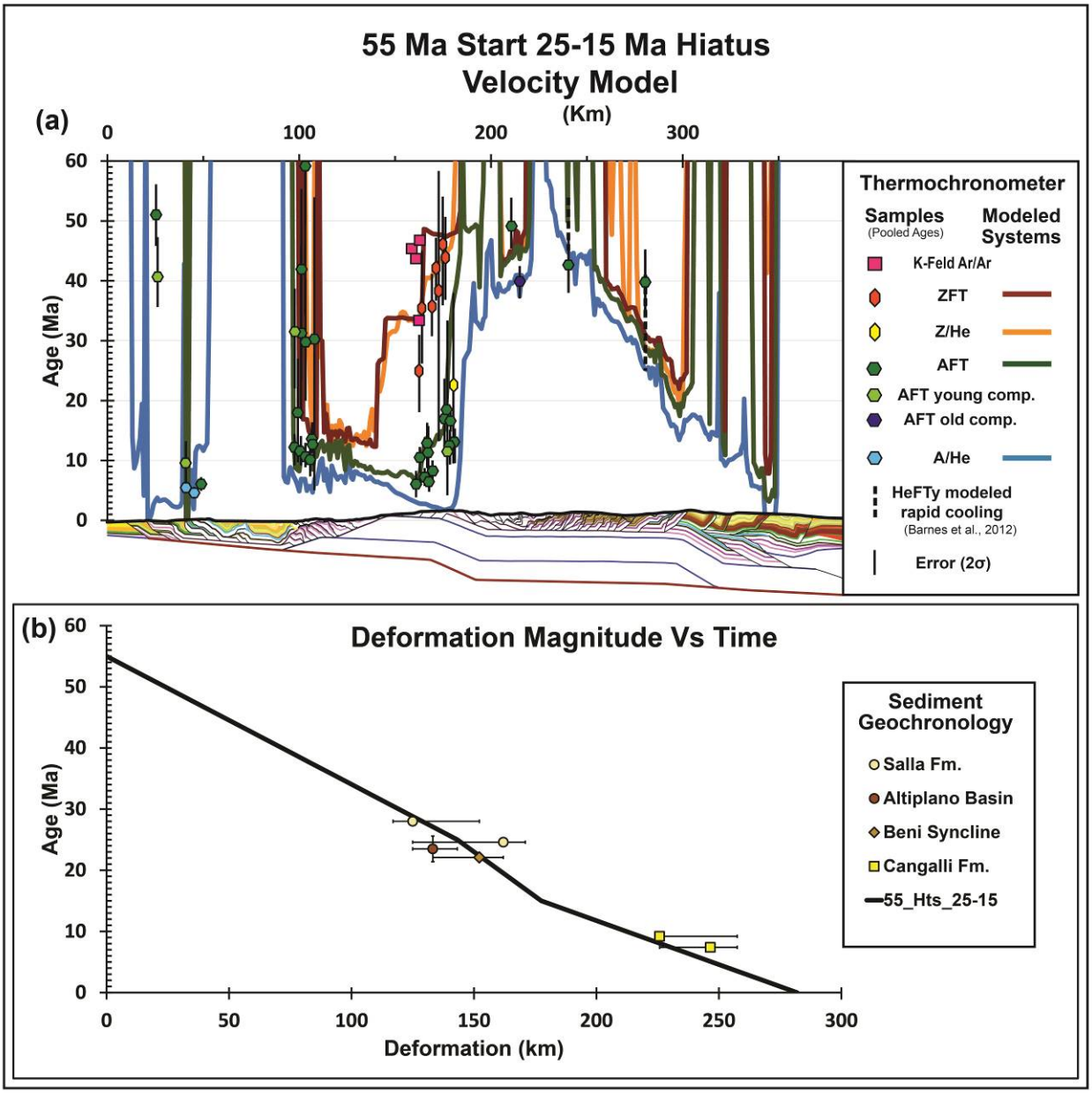

Figure 22. 55 Ma start 25-15 Ma hiatus velocity model thermochronometer plot (a) and deformation magnitude plot (b).

Predicted IA AFT cooling ages intersect 62% of the 13 measured AFT samples while the remaining 5 samples fall within a cooling envelope between AFT and Z/He cooling signatures (Fig. 22a). Predicted cooling in the eastern EC intersect 69% of the AFT data. The 55 Ma start

25-15 Ma hiatus velocity model accurately predicts AFT cooling signals in the IA and EC while intersecting more sediment geochronology samples than other hiatus models.

5.5.1.2 55 Ma Start 25-12 Ma Hiatus

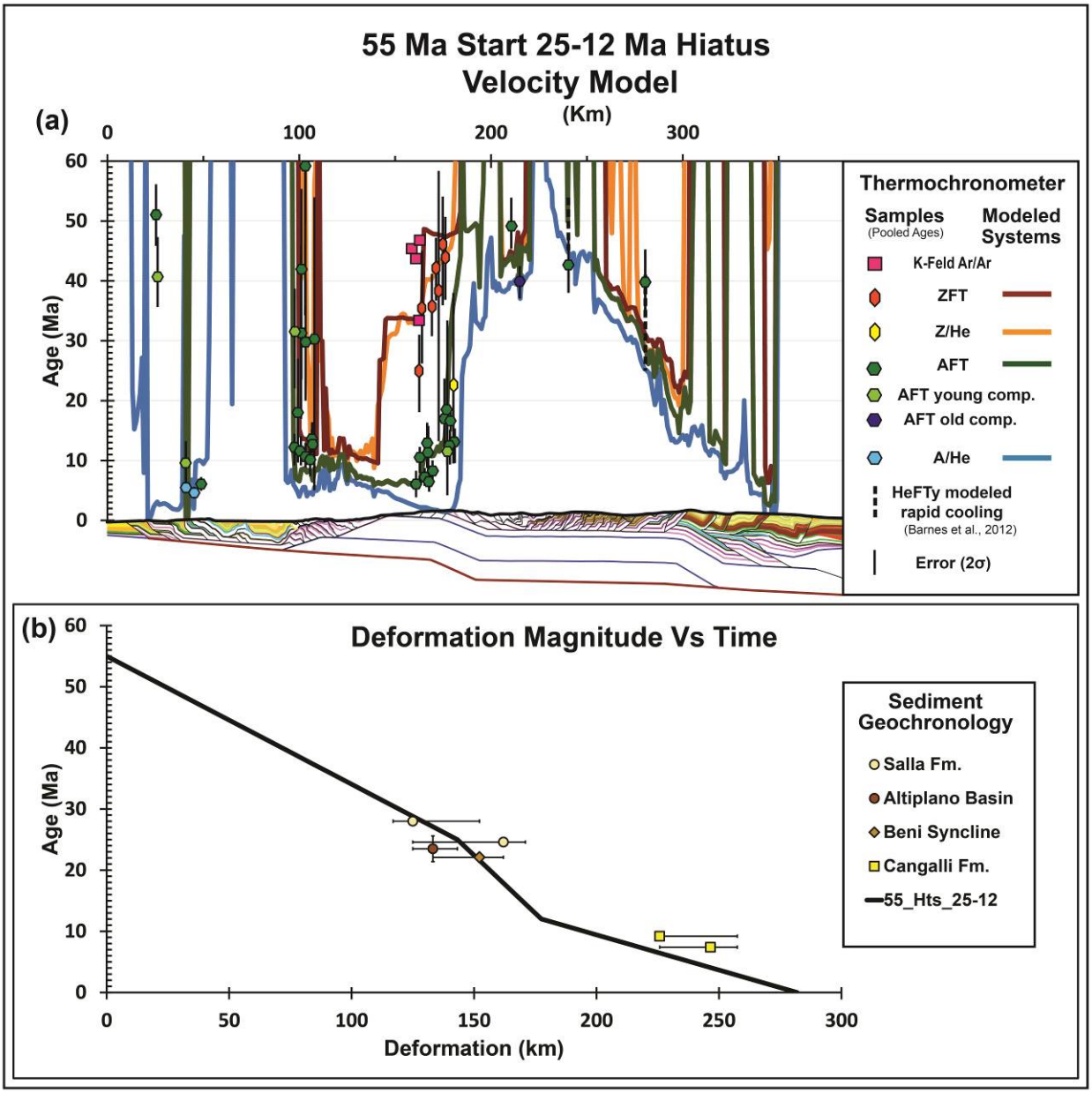

Figure 23. 55 Ma start 25-12 Ma hiatus velocity model thermochronometer (a) plot and deformation magnitude plot (a).

Predicted AFT cooling ages in the IA only intersects 46% of the 13 measured AFT samples while the remaining 8 samples fall within a cooling envelope between AFT and Z/He cooling signatures (Fig. 23a). The predicted AFT cooling signature in the IA intersects only the youngest measured AFT ages, suggesting these data are sensitive to the later SA starts induced by longer hiatus models. Predicted cooling in the eastern EC intersects 62% of the AFT data and is nearly indistinguishable from the 25-15 Ma hiatus model prediction. The 55 Ma start 25-12 Ma hiatus velocity predicts young AFT ages in IA when compared to the 25-15 Ma hiatus model.

5.5.1.3 55 Ma Start 25-8 Ma Hiatus

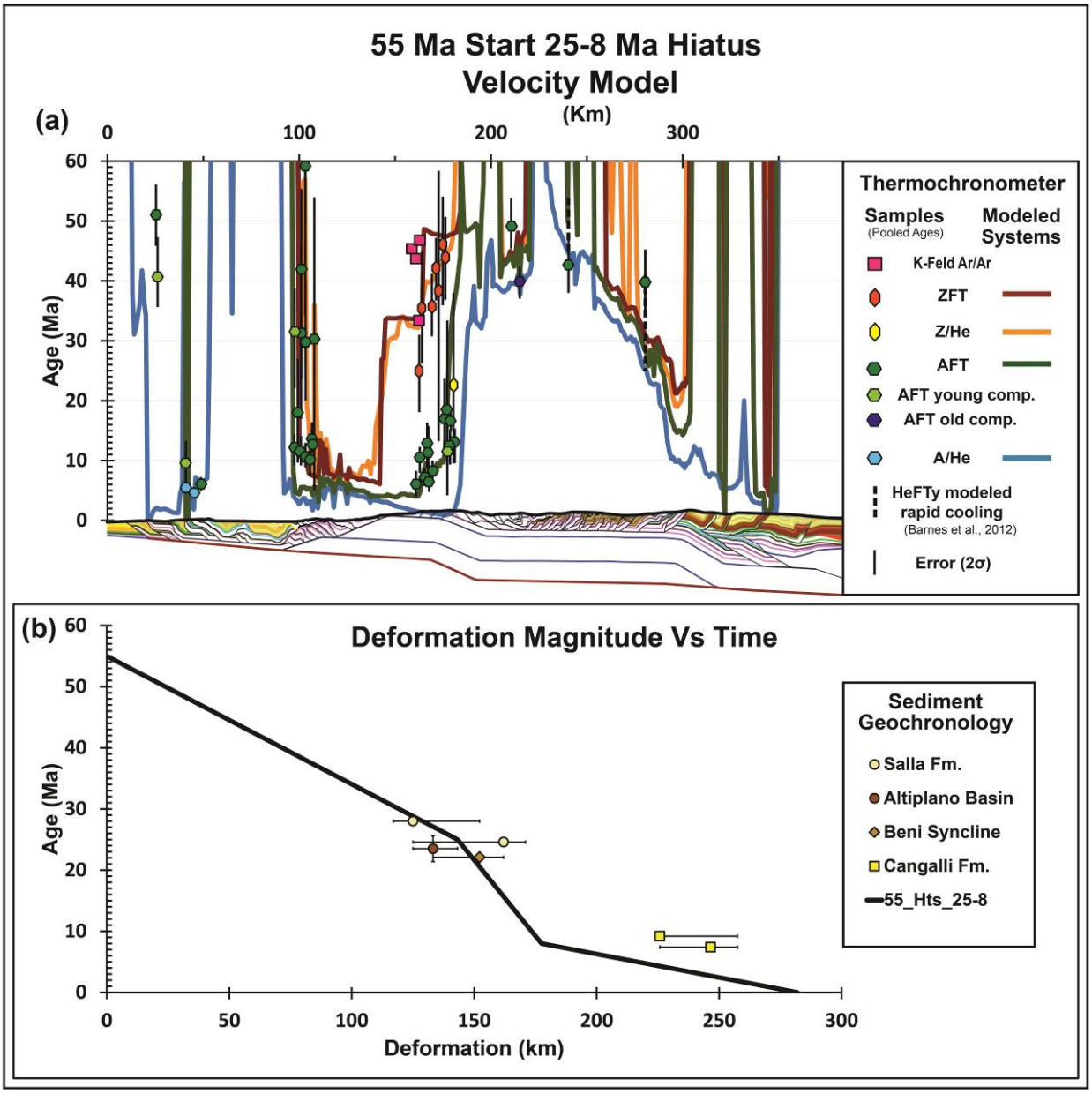

Figure 24. 55 Ma start 25-8 Ma hiatus velocity model thermochronometer plot (a) and deformation magnitude plot (b).

Predicted AFT cooling ages intersect only 31% of the 13 measured AFT samples in the IA while the remaining 8 samples still fall within the age cooling envelope between ZFT and Z/He cooling signatures (Fig. 24a). Predicted AFT cooling ages in the IA are much younger (~5 Ma) than the youngest measured AFT data. Predicted cooling in the eastern EC intersects 77% of

the AFT samples and follows the youngest trend in the data. The 55 Ma start 25-8 Ma hiatus velocity model predicts AFT ages in IA that are ~5 Ma too young while eastern EC AFT trends overlap the youngest recorded ages.

5.5.2 Sine Function Velocity Models

The sine function velocity models allow for increased rates of deformation at different times in the model and were tested at 50 Ma start and 55 Ma start dates (Fig. 21; green dashed lines). The application of a sine function to the rate of shortening is used to illustrate the sensitivity of the model to changes in deformation rate through time. Sine function velocity models are used to identify velocity models that fit specific thermochronometer cooling or chronostratigraphic characteristics by applying higher and lower rates of deformation throughout the model. The smooth character of the sine function requires more gradual transitions in shortening rates rather than instantaneous shifts used in the step function velocity models. The two sine function velocity models (Sine 50 Ma start and Sine 55 Ma start) are described separately due to their differences in predicted thermochronometer spectrum and predicted basin ages but have similar wedge-top constraint relationships. Both sine models fit the Salla Formation constraint but predict erosion of Ordovician rocks in the eastern EC >2 Ma later than the earliest depositional history of the Cangalli Formation. While both models fit the Salla Formation wedge-top constraints, the time envelopes differ significantly with the Sine 55 Ma start model predicted ages intersecting the younger bounds (32-14 Ma) and the 50 Ma start model intersecting the older bounds (36-20) of Salla Formation samples (Figs. 25b and 26b). Both model windows of Salla Formation deposition encompass long periods of time because of the low rates of deformation in the middle of the sine velocity models causing higher dispersion

predicted basin ages. Variations in the rates of shortening produce unique differences in the shape of the thermochronometer spectra that are related to character of the sine functions.

5.5.2.1 Sine 50 Ma Start Velocity Model

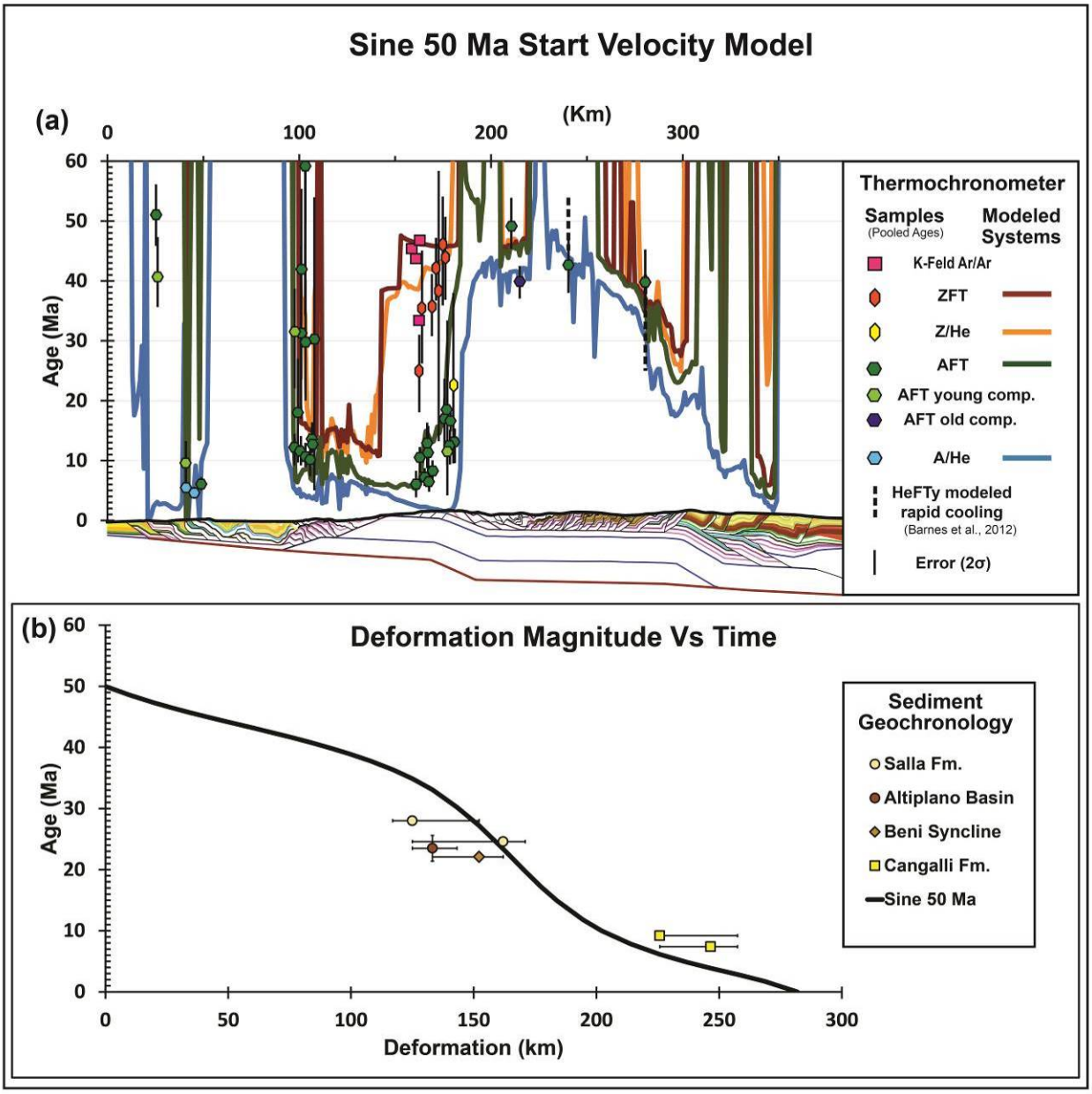

Figure 25. Sine 50 Ma start velocity model thermochronometer plot (a) and deformation magnitude plot (b).

Cooling signatures in the SA are characterized by a similar fit as in previous models with an optimal fit to A/He samples and a poor fit to AFT samples. The Sine 50 Ma start model produces a broadening and younging of the A/He signature and also partially reset the AFT signature in the westernmost SA thrust sheet (Fig. 25a at 55 km). Predicted cooling of AFT in the IA intersects 54% of the ages trending along the youngest bounds of the sample errors. Predicted cooling signatures in the eastern EC intersect 62% of the AFT samples, 57% of the ZFT samples and misses the Z/He sample. Predicted cooling of the ZFT system in the eastern EC is too old and only intersects the oldest samples. Predicted AFT cooling in the EC backthrust belt fits moderately, intersecting 50% of the samples. The Sine 50 Ma start model produces a broadening of the A/He signature in the SA, young AFT predicted ages in the IA, and old ZFT and AFT predicted ages in the eastern EC. The time window associated with deposition of the SA geochronologic sample is 33-23 Ma, predicting sedimentation in the SA that is too old, and does not agree with the sample age. The time envelope associated with the AP geochronologic sample is 35-30 Ma, also predicting sedimentation in the AP that is too old to agree with the sample age. Both predicted basin chronostratigraphic packages in the Sine 50 Ma start model do not fit the sample data.

5.5.2.2 Sine 55 Ma Start Velocity Model

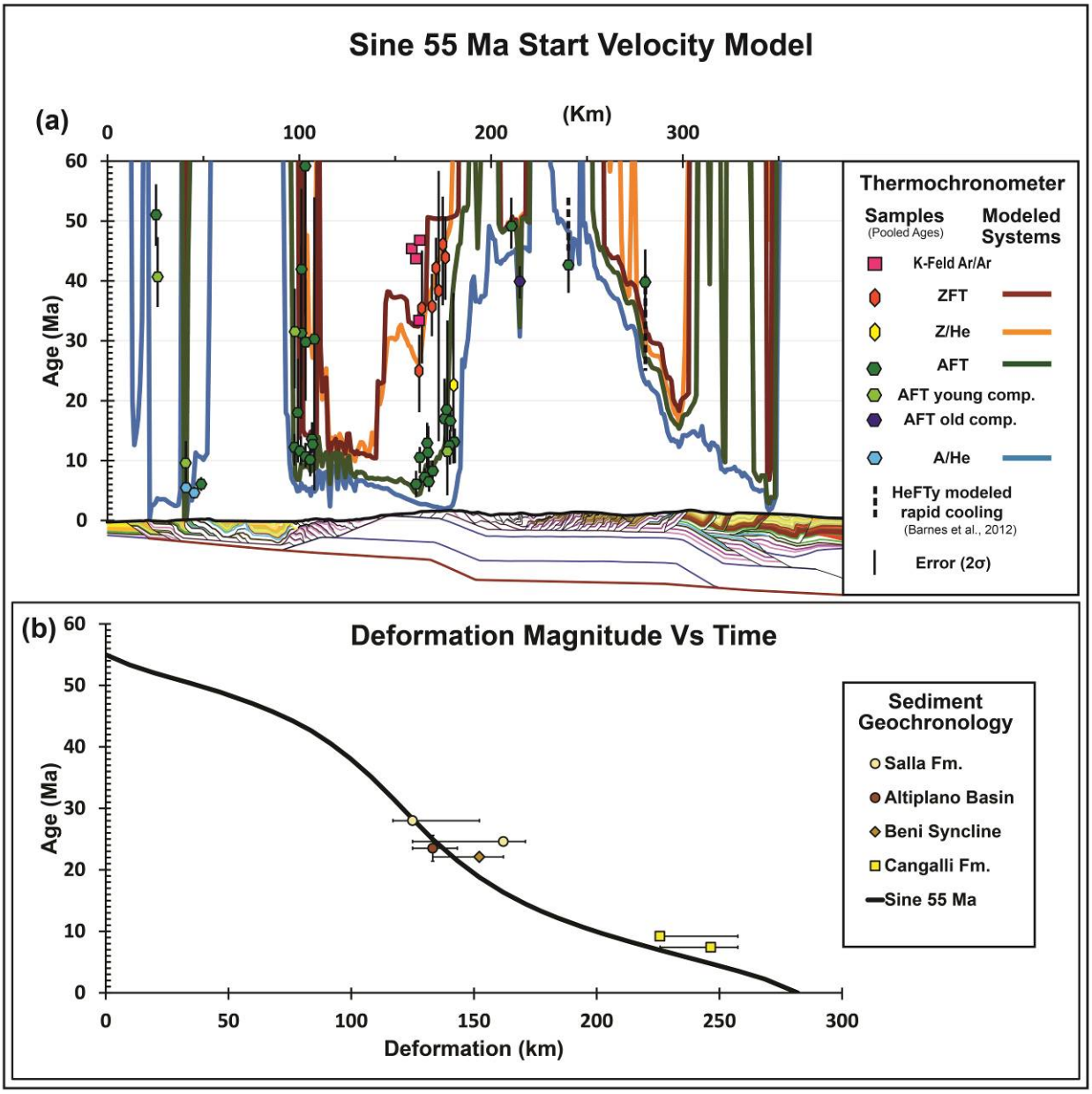

Figure 26. Sine 55 Ma start velocity model thermochronometer plot (a) and deformation magnitude plot (b).

Predicted cooling in the SA for the Sine 55 model are the same as the 50 Ma and 40 Ma start models and the hiatus models with an optimal fit to the A/He samples and a poor fit to the AFT samples. In the IA predicted AFT cooling signature intersects 62% of the samples and trend along the younger AFT sample pooled ages (Fig. 26a). Predicted cooling signatures in the eastern EC intersect 85% of the AFT samples, 57% of the ZFT samples and misses the Z/He sample. The predicted AFT signature in the eastern EC lies in the middle of the younger AFT ages, intersecting nearly all the sample ages in the region. Predicted AFT cooling in the western EC shows a good fit intersecting three of the four samples including the oldest sample in the center of the EC. The Sine 55 Ma start model accurately predicts young pooled AFT age trends in the IA and EC with predicted ZFT in the EC slightly older than most measured samples. The time window associated with deposition of the SA geochronologic sample is 25-16 Ma overlapping the sample age. The time envelope associated with the AP geochronologic sample is 28-22 Ma, encompassing the Corque Syncline sample age. Both predicted basin chronostratigraphic packages in the Sine 55 Ma start model fit the sample data in the foreland and hinterland.

5.5.3 Hybrid Velocity Models

Correlation between the shortening rate functions and specific thermochronometer and sediment geochronology constraints were used to tailor hybrid velocity models that fit specific chronologic data. The development of the unique hybrid velocity models attempts to maximize the chronologic fit to both datasets. The hybrid velocity models initiate at 50-55 Ma with a slight increase followed by a steadily decreasing trend till 15 Ma followed by a second, higher-amplitude, pulse that peaks near 11 Ma and diminishes thereafter (Fig. 21; blue and purple lines).

The fast initial start is selected to reset AFT systems in the EC early in the model. The long diminishing plateau in shortening rates from 45-52 Ma till 15 Ma is chosen to maximize the steepness of the ZFT cooling signatures in the eastern EC (from 170-200 km). The second pulse of deformation that peaks at 11 Ma is used to facilitate the resetting of AFT in the eastern EC and IA and erode the Ordovician formations in the eastern EC to fit the Cangalli Formation geochronology sample depositional age. While initiation of the hybrid models differ by 5 Ma the velocities used converge by 40 Ma and remain similar thereafter (Fig. 21; blue and purple lines).

Both models accurately predict erosion and sedimentation in the model and fit the wedge-top and basin geochronologic data (Fig. 27b and 28b). Erosion of Paleozoic formations in the EC backthrust belt occurs at 32 Ma in both models, predating the earliest deposition of the Salla Formation by 4 Ma and agreeing with sample ages. Both models erode Ordovician formations in the eastern EC at 9 Ma synchronously with the earliest depositional age of the Cangalli Formation. The age window associated with the SA geochronology sample is 28-19 Ma encompassing the Beni Syncline sample age. The ages associated with the AP sample are 30 Ma at the bottom and 25.3-25.6 Ma at the top falling within the older age range of the sample from the Corque Syncline (23.5 ± 2.1 Ma). Cooling of thermochronometers is described independently due to their unique characters.

5.5.3.1 Hybrid 50 Ma Start Velocity Model

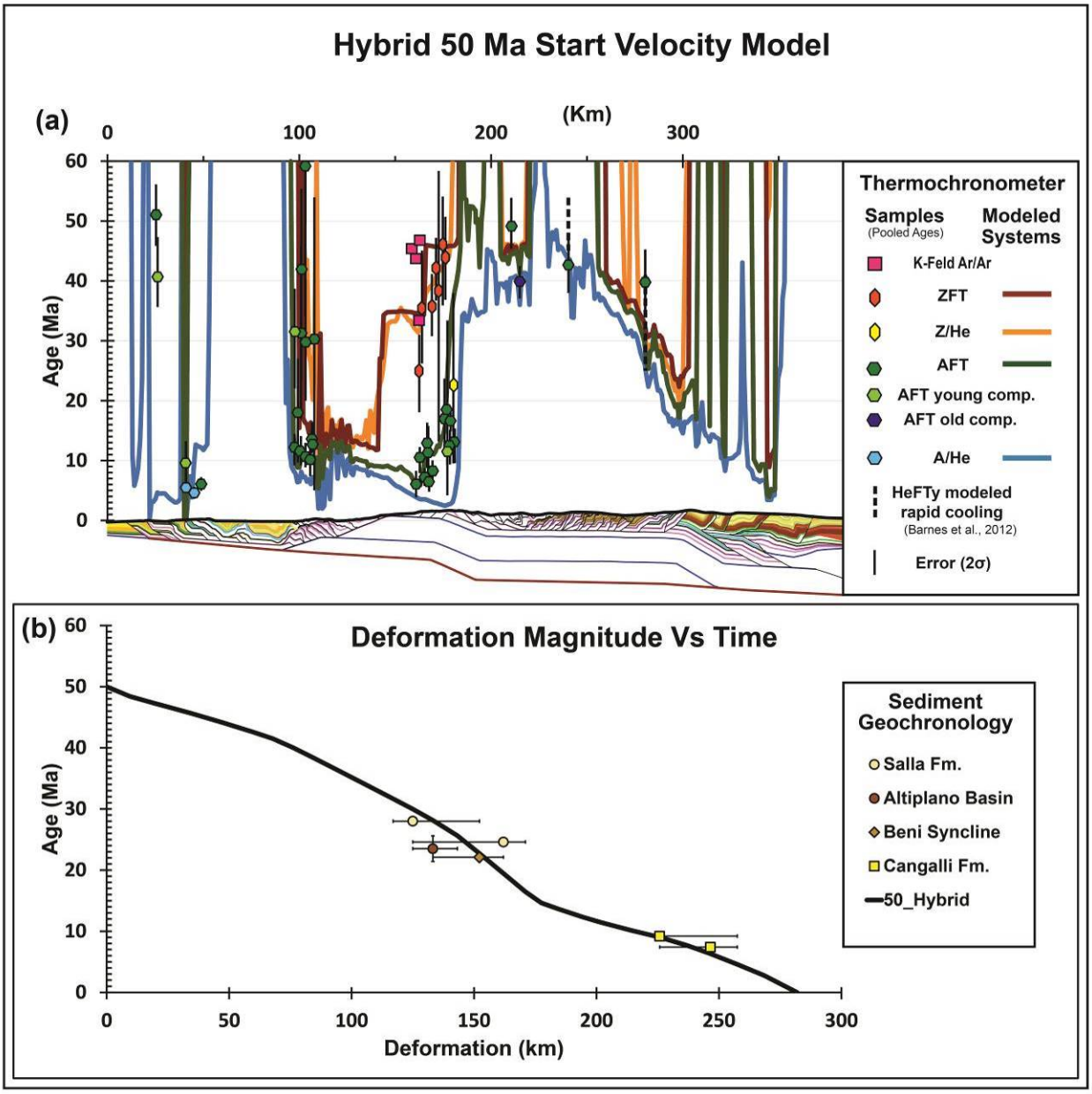

Figure 27. Hybrid 50 Ma start velocity model thermochronometer plot (a) and deformation magnitude plot (b).

Cooling signals in the SA are similar to the 50 and 40 Ma start models and show an optimal fit to A/He samples and a poor fit to AFT samples (Fig. 27a). Predicted cooling ages in the IA intersects 54% of the AFT samples with the remaining 7 samples falling within a cooling envelope between AFT and Z/He cooling signatures. Cooling signatures in the eastern EC

intersect 77% of the AFT data, 71% of the ZFT samples, and do not fit the Z/He sample age. Predicted AFT cooling in the western EC shows a moderate fit, overlapping 50% of the samples. The Hybrid 50 Ma start velocity model reproduces the trends of the young AFT ages in the IA and intersect the upper and lower young AFT ages in the eastern EC.

5.5.3.2 Hybrid 55 Ma Start Velocity Model

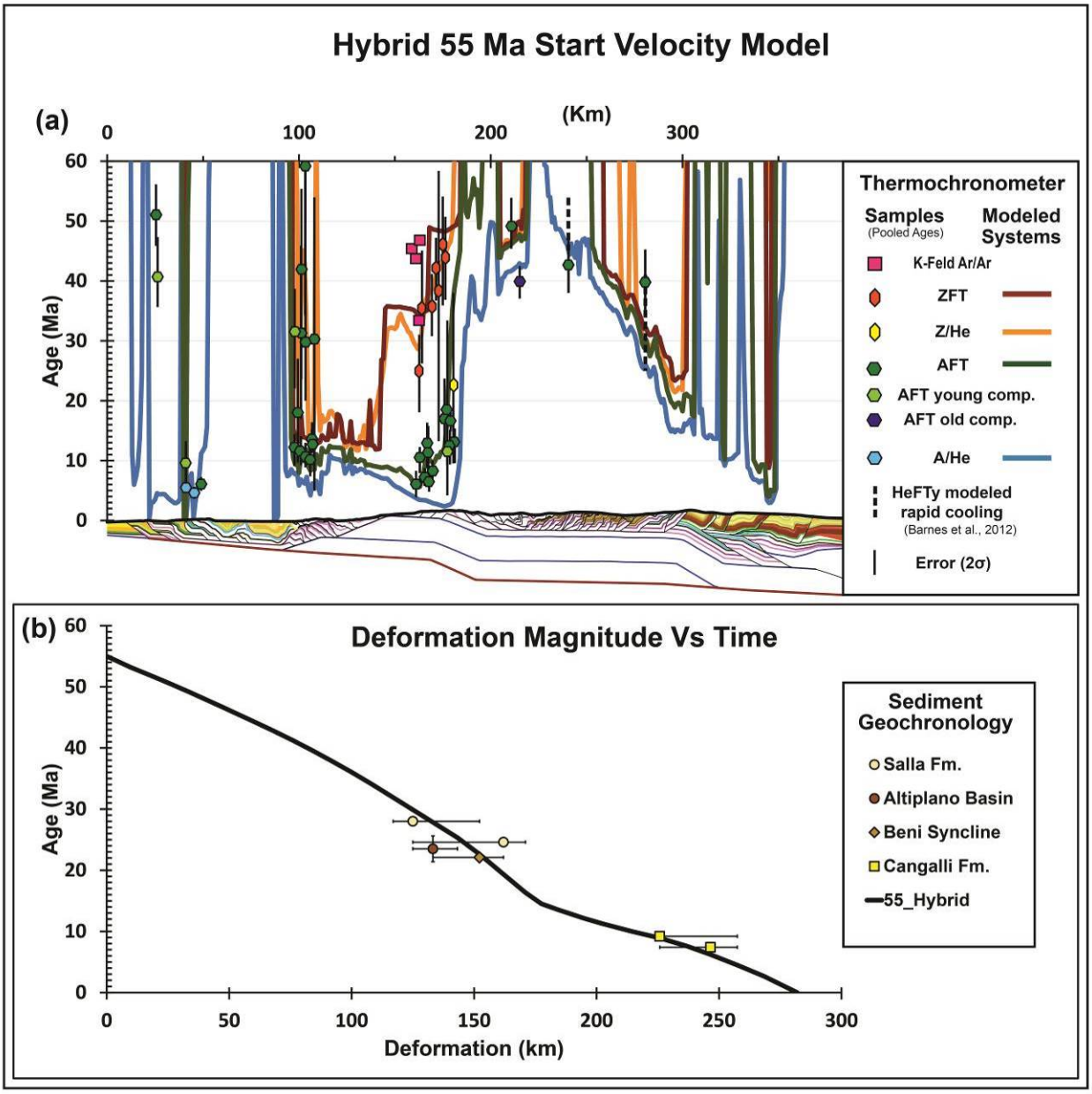

Figure 28. Hybrid 55 Ma start velocity model thermochronometer plot (a) and deformation magnitude plot (b).

Cooling signals in the SA are similar to the 55 Ma start models and show an optimal fit to A/He samples, that is broader than the 50 Ma start models, and a poor fit to the AFT sample ages (Fig. 28a). Predicted cooling ages in the IA intersect 46% of the AFT samples with the remaining 8 samples falling within a cooling envelope between AFT and Z/He cooling signatures. Cooling

spectra in the eastern EC intersects 92% of the AFT ages, 71% of the ZFT samples, and misses the Z/He sample age. Predicted cooling ages in the AFT system fall in the middle of the older and younger sample ages and intersect nearly all samples. Predicted AFT cooling in the western EC shows a moderate fit, overlapping 50% of the samples, including the oldest EC sample in the center of the EC. While the hybrid 55 Ma and the hybrid 50 Ma rates are similar in the last 15 Myr. The hybrid 55 Ma model starts the second pulse of deformation at 15 Ma (versus 16 Ma) and reaches the peak rate at 9.5 Ma (versus 10 Ma) this subtle shift makes the fit to published data EC AFT data better by 15% but decreases the IA AFT fit by 8%. The hybrid 55 Ma start model reproduces the trends of the younger AFT ages in the IA and EC, intersects the oldest AFT sample in the EC backthrust belt and intersects most of the AFT samples.

5.6 BEST FIT MODELS

Velocity models were compared based on their ability of match the thermochronometry and geochronology data along the modeled section with equal weight given to each sample (Table 2). The total percent fit for each model was calculated by dividing the amount of chronologic samples the model intersected by the total samples along the section. Variable initiation constant velocity models show similar fits to SA thermochronometry and show a decreasing total percent fit with 40 Ma and 30 Ma start models. Younger start models miss an increasing number of AFT ages in the IA and western EC and ZFT in the eastern EC as well as the measured ages of sediment geochronology samples. While the 55 Ma start constant velocity model is similar to the 50 Ma start constant velocity model, it misses SA and AP basin geochronology and some of the thermochronometry in the IA and eastern EC with a 54% fit to

the AFT ages and a 57% match to the ZFT ages. The 50 Ma start constant velocity model fits AFT ages in the IA (62%) and eastern EC (54%), ZFT ages (71%) and sediment geochronology samples better than other variable initiation models tested. The 50 Ma start constant velocity model is selected as the best constant velocity model intersecting 64% of the chronologic constraints.

The preferred hiatus model was determined by the best possible fit to IA AFT samples and the Cangalli Formation constraint. Hiatus models all have the same fit to measured SA ages and older ages (50-30 Ma) in the EC along with Salla wedge-top and basin geochronology constraints. The models fit IA and EC AFT thermochronometry data and Cangalli Formation constraints differently and are specifically scrutinized in these areas. Models with shorter hiatal periods increasingly match IA AFT samples and intersect the Cangalli Formation constraint. The 25-15 Ma hiatus model has the shortest (10 Ma) hiatus and accurately predicts the 10-14 Ma cooling ages in the IA and intersects one of the two the Cangalli Formation constraint. The 25-15 Ma hiatus velocity model fit the most chronologic constraints out of the 3 hiatus model tested and was chosen as the best hiatus velocity model. Overall the velocity model fits 62% of the chronologies suggesting a good match to both datasets (Table 2).

Sine models illustrate the application of a continually changing rate of deformation model and are unique from one another based on the predicted cooling in the IA and EC, Cangalli Formation depositional windows and basin sediment ages. Both Sine models have the same fit to SA thermochronometer samples with an optimal fit to A/He samples and a poor fit to AFT samples. In addition, both models predict two of the four EC backthrust belt samples and match the Salla Formation depositional window. The high amplitude rate of deformation in the Sine 50 Ma start model cause misfits when compared to the Cangalli Formation wedge-top samples and

the basin geochronology. The pulse of early rapid deformation causes the predicted basin ages to be too old while the pulse of young rapid deformation causes the erosion that must predate the Cangalli Formation to be too young (Fig. 21b). The Sine 55 Ma start velocity model fits all the sediment geochronology except the earliest Cangalli Formation sample age and predicted 8% more of the AFT cooling the IA and 23% more of the AFT cooling in the EC when compared to the Sine 50 Ma start model. The different fit to the chronologic data with each of the Sine models shows the sensitivity of this model to varying rates of deformation through time and identifies the importance of determining the best fit to both; the initiation of deformation, and the variable rate of deformation to understand the shortening history of a FTB. The preferred sine velocity model was determined to be the Sine 55 Ma start model with a 66% fit to the chronologic constraints (Table 2).

Table 2. Comparison of velocity model predicted chronology to thermochronometry and geochronology samples.

	Thermochronometry % fit							Geochronology % fit				
Sample type/location	***SA AFT***	***SA A/He***	***IA AFT***	***EC AFT***	***E-EC ZFT***	***E-EC Z/He***	***W-EC AFT***	***Salla Fm.***	***Cangalli Fm.***	***SA Basin***	***AP Basin***	***Total Fit***
Constant rate models												
50 Ma start	25%	100%	62%	54%	71%	0%	75%	100%	100%	100%	100%	**64%**
40 Ma start	25%	100%	54%	54%	57%	100%	0%	0%	50%	0%	100%	**48%**
30 Ma start	25%	100%	38%	77%	29%	100%	0%	0%	0%	0%	0%	**42%**
55 Ma start	25%	100%	54%	54%	57%	0%	75%	100%	100%	0%	0%	**56%**
55 Ma start hiatus models												
Hiatus 25-15 Ma	25%	100%	62%	69%	57%	0%	50%	100%	50%	100%	100%	**62%**
Hiatus 25-12 Ma	25%	100%	46%	62%	57%	0%	50%	100%	0%	100%	100%	**54%**
Hiatus 25-8 Ma	25%	100%	38%	77%	57%	0%	50%	100%	0%	100%	100%	**56%**
Variable rate models												
Sine 50 Ma start	25%	100%	54%	62%	57%	0%	50%	100%	0%	0%	0%	**52%**
Sine 55 Ma start	25%	100%	62%	85%	57%	0%	50%	100%	50%	100%	100%	**66%**
Hybrid 50 Ma start	25%	100%	54%	77%	71%	0%	50%	100%	100%	100%	100%	**66%**
Hybrid 55 Ma start	25%	100%	46%	92%	71%	0%	50%	100%	100%	100%	100%	**68%**
Ao = 0.7 µW/m³ models												
50 Ma start	25%	100%	69%	69%	100%	0%	75%	100%	100%	100%	100%	**74%**
55 Ma start	50%	100%	69%	69%	86%	0%	50%	100%	100%	0%	0%	**68%**
50 Ma - Hts. 25-15 Ma	25%	100%	62%	92%	100%	0%	75%	100%	50%	100%	100%	**78%**
55 Ma - Hts. 25-15 Ma	25%	100%	62%	92%	86%	0%	50%	100%	50%	100%	100%	**72%**

The hybrid velocity models are nearly indistinguishable and only differ slightly in the fit of AFT in the EC and IA. The hybrid velocity models combine moderate amplitude variability in deformation rate with long periods of relatively consistent rates of deformation. Both Hybrid models have a significant increase in rates at the beginning of SA deformation. This facilitates early erosion of Ordovician rocks and subsequent deposition of the Cangalli Formation matching foreland wedge-top chronologic constraints. The Hybrid 55 Ma start velocity model predicts 8% less of the AFT in the AI and 15% more of the AFT in the EC compared to the Hybrid 50 Ma start model. The Hybrid 50 Ma and Hybrid 55 Ma models have nearly identical matches to the chronologic data at 66% and 68% respectively. This similar fit with differing initiation ages illustrates the limitations of the model to distinguishing between a 50 or 55 Ma age of initial deformation – while the younger increase in deformation (16 or 15 Ma) is better constrained by the data. Despite these similarities, the Hybrid 55 Ma start model has the best fit to chronologic constrains (68%) when compared to the Hybrid 50 Ma start model and is the best fitting model tested. The combination of these and thermal modeling (discussed below) suggests an envelope of acceptable rates of deformation in the northern Bolivian Andes that falls between the best velocity models. The best fit velocity envelope would acceptably reproduce the chronologic data along the modeled section and requires an early 50-55 Ma start, but allows for a constant rate of deformation or variable deformation rates for the region (Fig. 29, green area). One additional 25-15 Ma hiatus model is included in the acceptable velocity model diagram that initiates at 50 Ma (described in section 5.7.2, below) that is encompassed by the acceptable velocity envelope (Fig. 29).

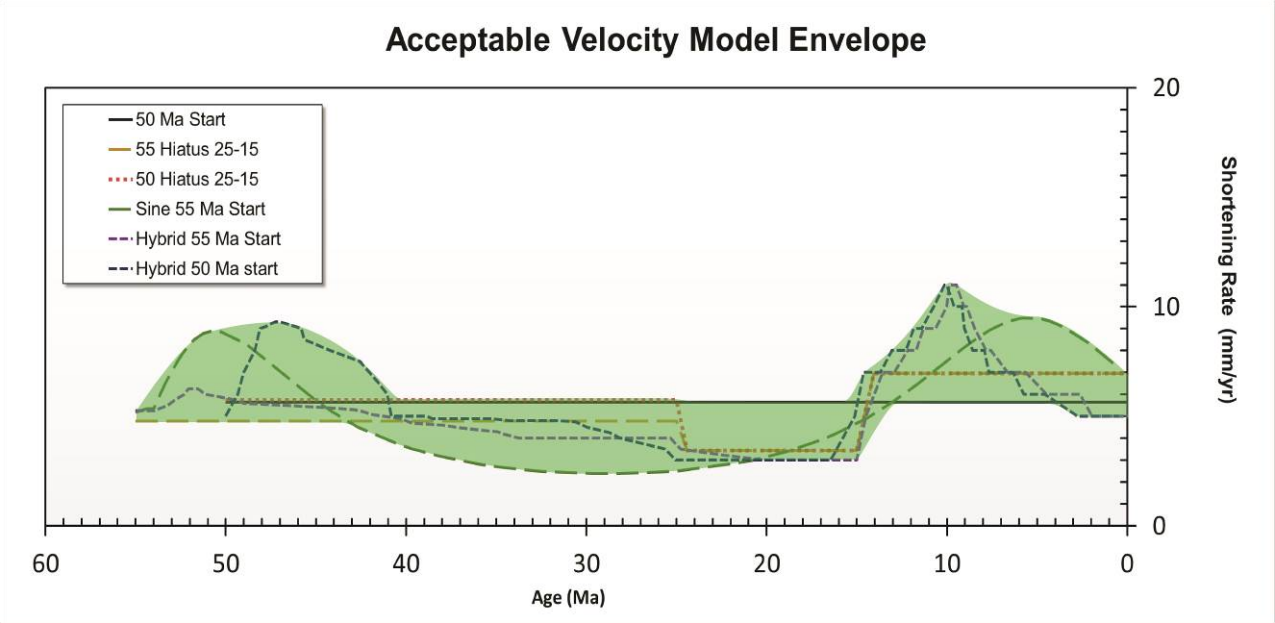

Figure 29. Velocity model plot showing the acceptable velocity model envelope (green) that predict the best fits to chronologic constraints.

5.7 MODELED THERMAL VARIATION

5.7.1 Variable Radiogenic Heat Production Values

Using the same constant velocity model, thermal parameters were changed to investigate the sensitivity of the model to different thermal states of the crust. Thermal modeling in *Pecube* requires estimates for a series of parameters including; radiogenic heat production, thermal conductivity, specific heat capacity, material density, size of model, temperature at the base of the model, temperature at the surface, and atmospheric lapse rate. Thermal parameters used are listed in table 1 and are based on previous thermochronometric modeling studies (Gilmore, 2014; McQuarrie and Ehlers, 2015) and other reported thermal parameters (Gonfiantini et al., 2001; Lucassen et al., 2001; Babeyko, 2005; Ehlers, 2005; Tassara et al., 2005). Reported radiogenic

heat production (Ao) values for the upper crust in the Andes range from 0.85-1.30 $\mu W/m^3$ with lower crustal measurements and modeled estimates that range 0.3-0.33 $\mu W/m^3$ (Babeyko, 2005; Ehlers, 2005; Syracuse et al., 2010). In this study, crustal Ao values are varied from 0.5 to 0.7 $\mu W/m^3$, and are an approximate average of reported upper and lower crustal values for radiogenic heat production in this region. All velocity models presented in the velocity modeling sections (sections 5.4 and 5.5, above) use Ao = 0.6 $\mu W/m^3$, a radiogenic heat production value in the middle of the values tested in this section.

Three different Ao values (0.5, 0.6, and 0.7 $\mu W/m^3$) are evaluated for a 50 Ma start constant-velocity model to evaluate the magnitude of change in modeled cooling ages with changes in Ao. Increased heat production values promote elevated thermal gradients and result in younger predicted thermochronometer cooling ages because sample points cool through their closure temperatures later in the model. To a first order, the predicted AFT ages show minimal variations due to changes in Ao. The notable exception is a younging of predicted AFT ages with increased radiogenic heat production in the eastern EC at 150-170 km (Fig. 30). Predicted AFT cooling ages are 6-10 Ma older for the 0.5 $\mu W/m^3$ than for the 0.7 $\mu W/m^3$ in the eastern EC. In addition, predicted AFT ages in the EC backthrust belt (Fig. 30; 190 km) show an 18 Ma difference between the highest and lowest Ao values tested. Predicted ZFT ages show a higher degree of variability with changes in Ao. Predicted ZFT ages in the eastern EC (Fig. 31; 150-175 km) decreases significantly with increasing radiogenic heat production and have broader reset patterns across the model. The ~15 Ma younging of the predicted ZFT ages with higher heat production increases the fit to the measured ZFT samples in the eastern EC with the 0.7 $\mu W/m^3$ intersecting all seven samples.

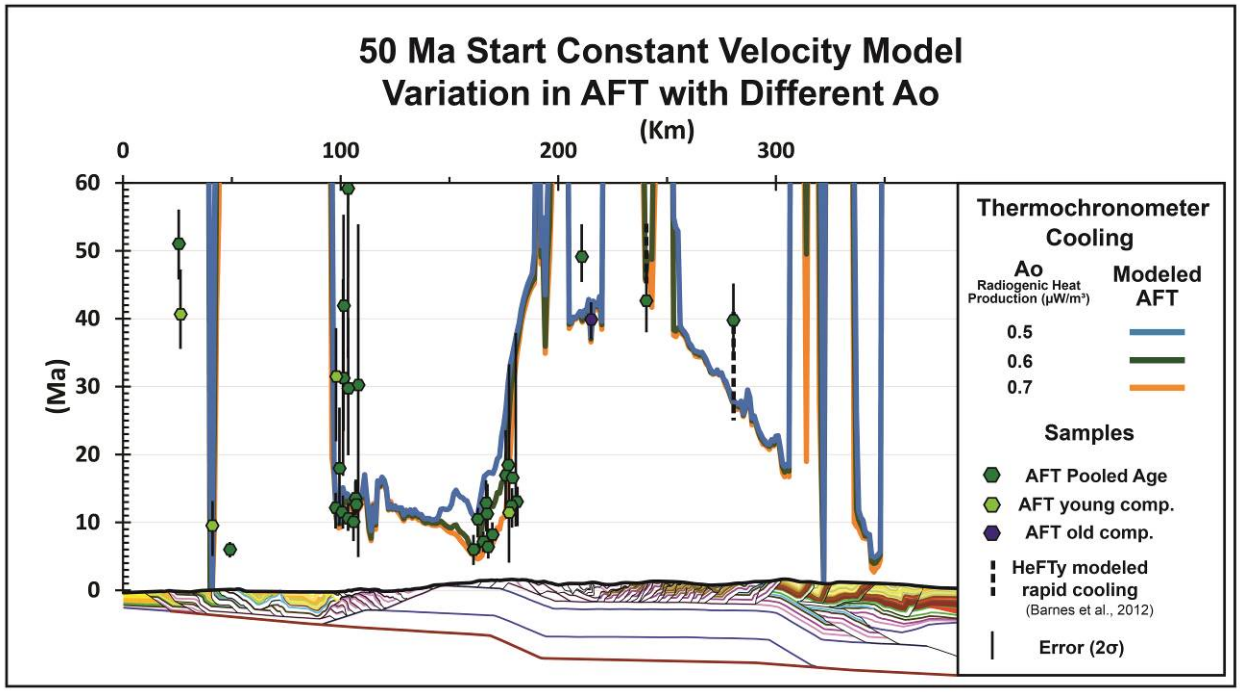

Figure 30. Thermochronometer plot for 50 Ma start models showing the variation in AFT predicted cooling with different radiogenic heat production values (Ao).

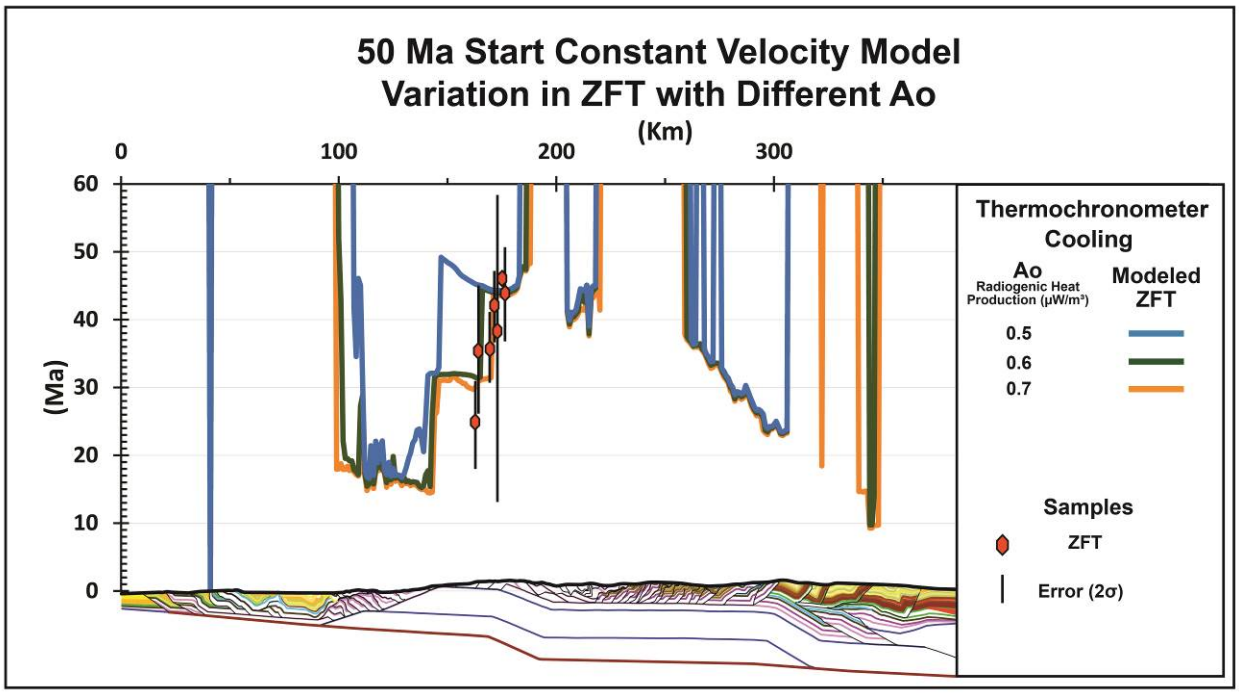

Figure 31. Thermochronometer plot for 50 Ma start models showing the variation in ZFT predicted cooling with different radiogenic heat production values (Ao).

Younger predicted ages with increased radiogenic heat production is the most noticeable result and has been identified in similar modeling studied (Gilmore, 2014; McQuarrie and Ehlers, 2015) illustrating the influence of radiogenic heat production on thermochronometer cooling. Increasing radiogenic heat values improves the ZFT fits in the EC for both the 50 and 55 Ma start constant velocity models. Specific velocity models that are significantly improved by increased Ao are described below and display the best match between measured and modeled thermochronometer ages (Table 2). Although these results do not drastically change our velocity interpretations they indicate that older start models may be coupled with higher radiogenic heat production parameters to attain similar fits as slightly younger models with lower radiogenic heat production values.

Predicted AFT cooling in the SA with the 55 Ma start constant velocity model (Ao=0.7 $\mu W/m^3$) intersects the central sample and the westernmost sample (the best fit we attain) (Fig. 32a). The partial resetting of AFT in the western most thrust sheet with this long duration, high radiogenic heat production model suggests that the resetting of thermochronometers in basins in our model is influenced by rates of basin development (as identified above). With a higher Ao of 0.7 $\mu W/m^3$ the 55 Ma start velocity model is equal with the best fit model (Hybrid 55 Ma start model), intersecting 68% of the chronometer data (Table 2). The 55 Ma start hiatus from 25-15 Ma velocity model with Ao=0.7 $\mu W/m^3$ shows a 23% improvement to EC AFT data and a 29% increase in EC ZFT sample ages when compared to the Ao=0.6 $\mu W/m^3$ (Table 2). While this improves thermochronometer matches this does not change any mismatches with sediment chronologies, suggesting that the independent sediment chronology provides important timing information independent of thermal modeling parameters.

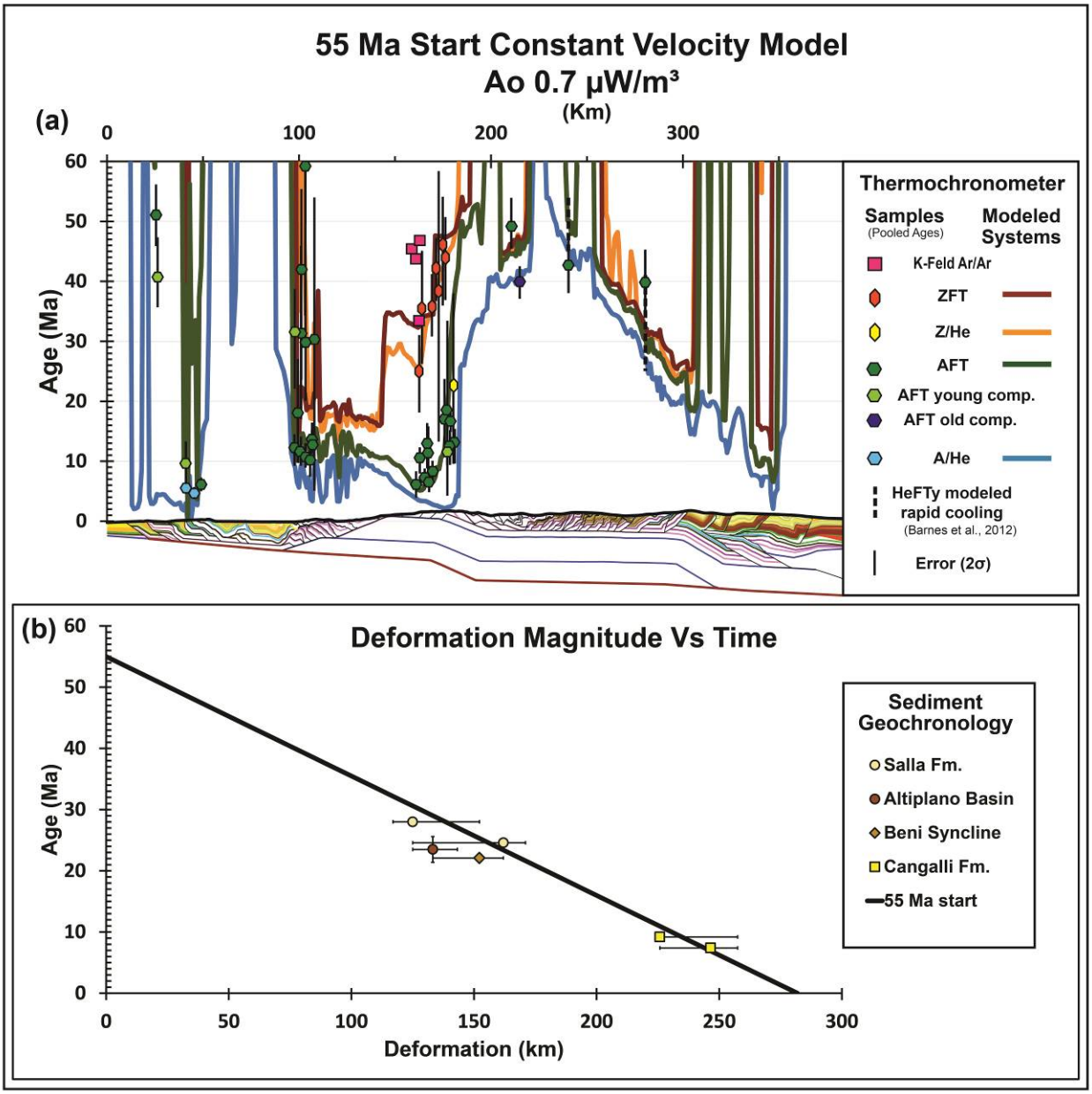

Figure 32. 55 Ma start constant velocity model with Ao=0.7µW/m^3 thermochronometer plot (a) and deformation magnitude plot (b).

The 55 Ma start 25-15 Ma hiatus velocity model with Ao=0.7 µW/m^3 intersects the same number of SA thermochronometers as the Ao=0.6 µW/m^3 model, with an optimal fit to A/He samples and a poor fit to AFT samples (Fig. 33a). Predicted cooling of AFT in the IA intersects 62% of the samples and is the same as the lower radiogenic head production model. Cooling of

thermochronometers in the eastern EC intersect 92% of the AFT samples, 86% of the ZFT samples and miss the Z/He sample. Predicted AFT cooling in the EC backthrust belt fits moderately, intersecting two of the four sample ages. The improved fit of the 55 Ma start 25-15 Ma hiatus velocity model in the IA and eastern EC is presented in table 2 and shows the increase in total chronologic fit from 62% to 72% with the increase from 0.6-0.7 μW/m^3 Ao.

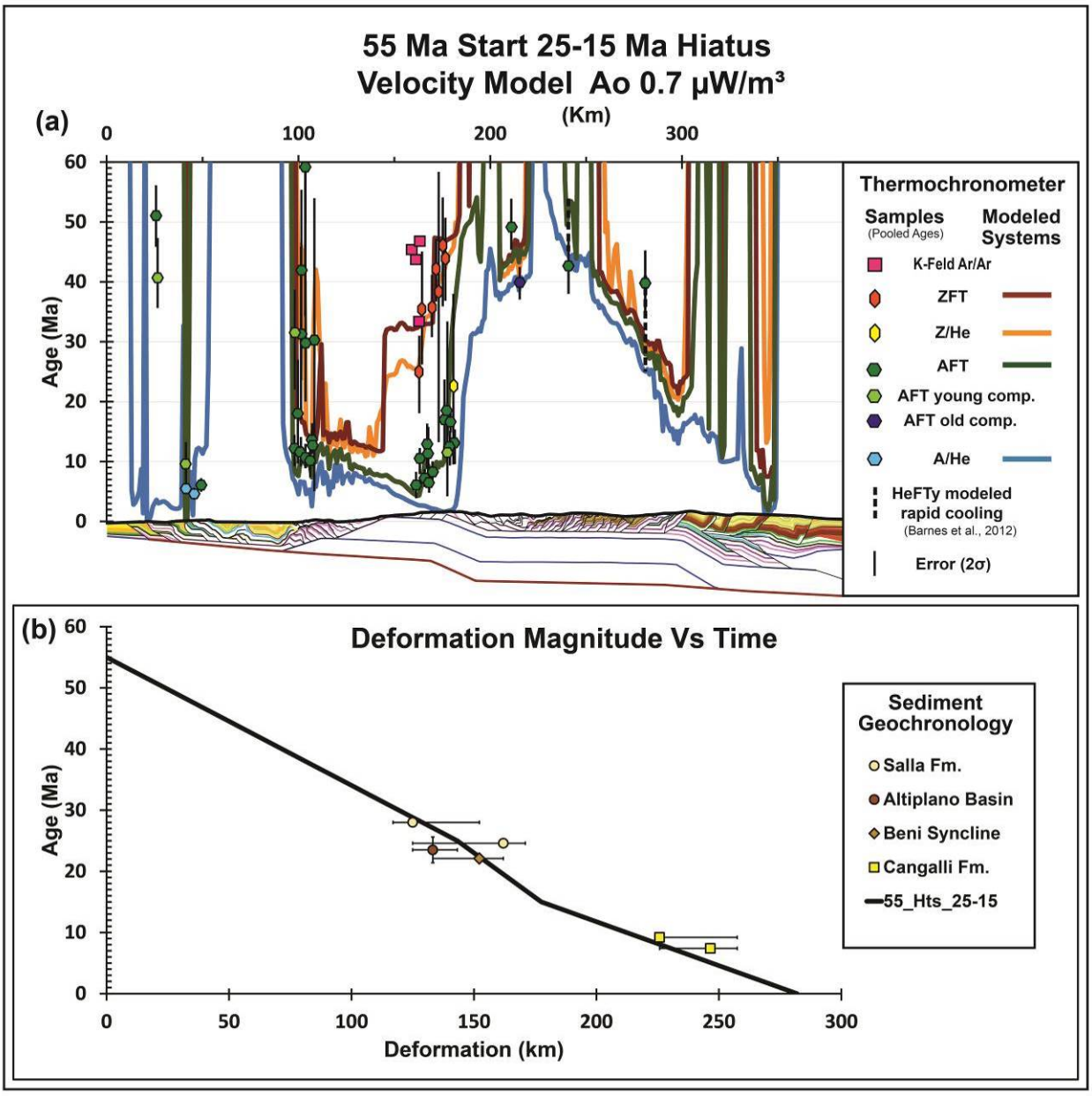

Figure 33. 55 Ma start 25-15 Ma hiatus velocity model with Ao=0.7μW/m^3 thermochronometer plot (a) and deformation magnitude plot (b).

With the thermal information above, a hiatus velocity model with decreased rates of deformation from 25-15 Ma with a 50 Ma start (proposed by McQuarrie et al., 2008) with a higher radiogenic heat production value (0.7 $\mu W/m^3$), was found to intersect the most chronologic data (78%) out of the velocity models tested (Table 2). Predicted cooling in the SA is similar to previous models, with an optimal fit to A/He samples and a poor fit to AFT samples. Predicted AFT cooling in the IA intersects 8 of the samples (62%) with the remaining 7 samples intersecting the cooling envelope between AFT and Z/He cooling (Fig. 34a). The increased fit to thermochronometer samples when compared to previous models occurs in the EC where ZFT and AFT are more accurately predicted. Cooling signatures in the eastern EC intersects 92% of the AFT samples and all 7 (100%) of the ZFT samples. Predicted cooling of AFT in the EC backthrust belt intersects 75% of the samples and is very close to intersecting the western most HeFTy modeled rapid cooling window (Barnes et al., 2012). Similar to the 55 Ma start hiatus from 25-15 Ma velocity model, all synorogenic sediment geochronology samples are intersected except the oldest constraint of the Cangalli Formation The 50 Ma start Hiatus from 25-15 Ma model with Ao=0.7 $\mu W/m^3$ provides a best fit model that most accurately reproduces EC thermochronology cooling and intersects the greatest amount of chronologic samples (78%) along the modeled line of section. While these thermal elevated radiogenic heat production value models increase the total fit of the velocity models they do not change our interpreted acceptable velocity envelope (Fig. 29).

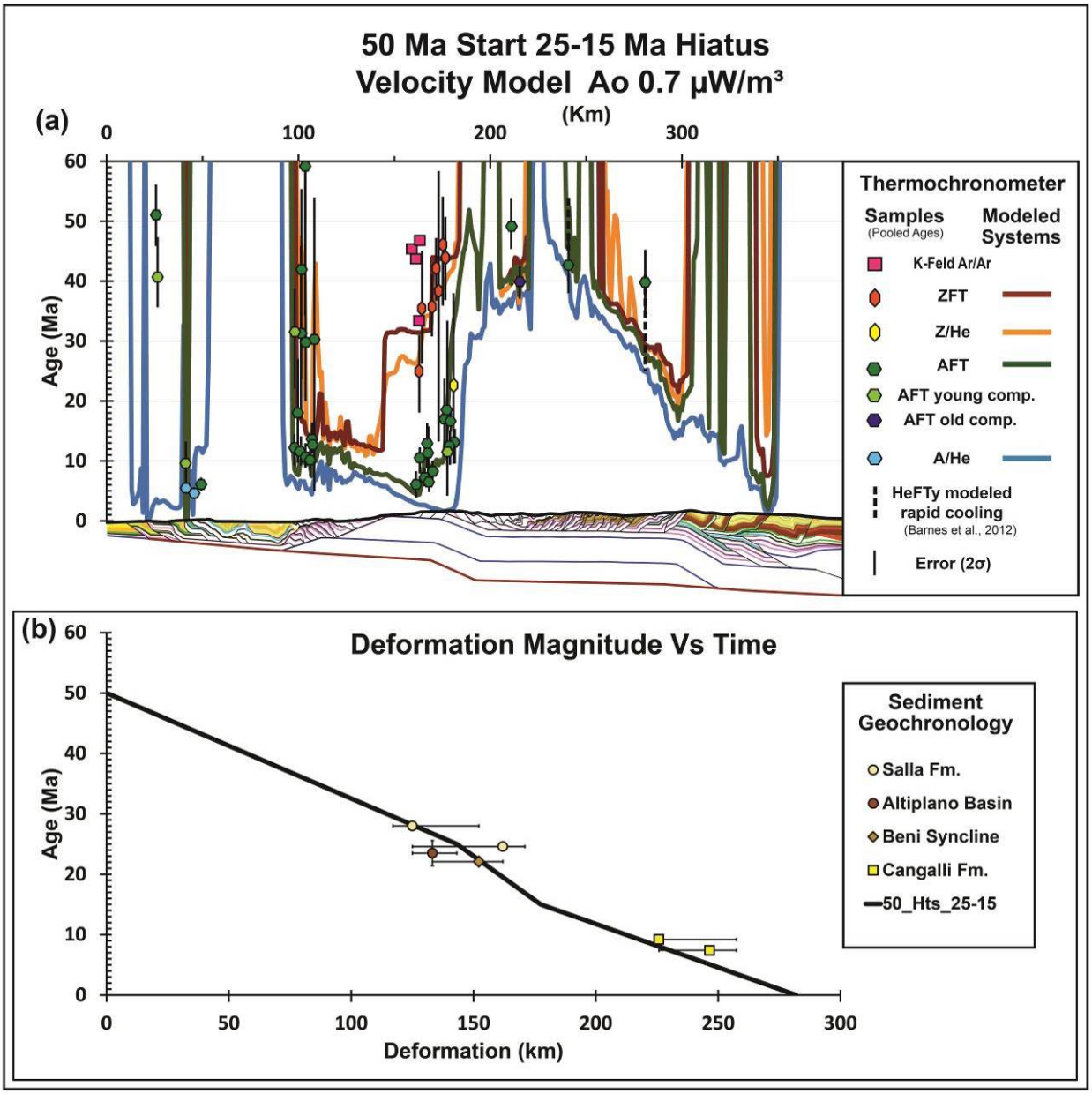

Figure 34. 50 Ma start 25-15 Ma hiatus velocity model with Ao=0.7µW/m^3 thermochronometer plot (a) and deformation magnitude plot (b).

6.0 DISCUSSION

6.1 DETERMINING DEFORMATION KINEMATICS FROM BALANCED CROSS SECTIONS

Linking thermokinematic models to balanced geological cross sections has been developed as a new tool to integrate deformation and exhumation as well as constrain the timing, rate and geometry of fault motion (Gilmore, 2014; Erdos et al., 2014; McQuarrie and Ehlers, 2015; Mora et al., 2015). While the thermal and thermochronometric modeling methods are almost identical in these studies, the kinematics that control material movement and the resulting subsurface deflection of isotherms are different. There are two approaches to producing a kinematic model from a balanced cross section. The method presented here starts with an undeformed cross section and sequentially deforms it, moving forward with time, taking into account isostatic loading and unloading due to faulting and erosion (McQuarrie and Ehlers, 2015). The second approach starts with the balanced cross section and uses palinspastic restoration to sequentially undo motion on faults moving backwards in time (Mora et al., 2015; Erdos et al., 2014). While in theory restoring motion forward or backward should produce the same kinematics, restorations that move backwards with time provide no mechanism to account for the deflection of points due to isostatic loading of faults or erosional unloading. If material is undeformed along the current fault system, the effects of isostatic loading through time is not taken into account

and material will project to an increasingly deeper level with respect to the surface of the earth. If topography is assumed to be steady state (Erdos et al., 2014) the sample of interest will restore deeper below the surface increasing the predicted peak burial temperature of the sample (e.g. Erdos et al., 2014) as well as the predicted magnitude of exhumation. Mora et al., (2015) estimated the magnitude of overburden based on the assumption that different fully reset thermochronometers provide estimates of closure temperature depth, assuming a geothermal gradient. The magnitude of overburden is adjusted as a parameter to determine the best modeled and predicted ages either by altering the dip of the decollement, the overlying topography or both. The dip of the most recent or modern decollement (as illustrated in any balanced cross section) is a function of the progressive load of the FTB, increasing the dip of the decollement angle through time (McQuarrie and Ehlers, 2015; Stockmal et al., 2007). Thus moving backwards in time (as modeled by Erdos et al., (2014) or Mora et al., (2015) the decollement angle would be expected to systematically decrease as isostatic loading from previous thrust faulting is removed. The importance of isostasy in FTB models was addressed by Stockmal et al., (2007) who noted in models where isostasy was applied, increased critical angles developed (isostatic loading increased the decollement angle β), creating broad synclinal basins and long thrust sheets, similar to the SA of northern Bolivia. Forward modeling of cross section kinematics allows isostatic adjustment of decollement, creation of a modeled foreland basin, and the exhumation of the FTB to be linked to this foreland basin evolution, facilitating this additional data to be incorporated into timing constraints (e.g. Robinson and McQuarrie, 2012). The significant effects of thrust belt loading on foreland basin morphology are well established (Jordan 1981; DeCelles, 2012). In this study we note that subsidence history (magnitude and age) effect the modeled thermal profile and imparts a cooler thermal signal to the foreland (see

section 6.5). Previous thermokinematic models that evaluate the advection of isotherms due to motion on a fault and the accompanying erosion had a fixed fault location in the center of the model [e.g. Bollinger et al., 2006; Célérier et al., 2009; Herman et al., 2010]. The fixed fault requires that convergence is partitioned into an overthrusting rate that advects warmer material from the hinterland and an underthrusting rate that bring cooler material from the foreland creating a locally inverted temperature gradient near the main fault (Henry et al., 1997; Bollinger et al., 2006; Célérier et al., 2009; Herman et al., 2010). In our modeling approach, the fault is not fixed, but the isostatic loading of the foreland and associated sedimentation depresses isotherms in the foreland while exhumation focused in the deforming hinterland raises and compresses isotherms in this region creating a thermal field that is similar in shape to ones generated in static fault models (Fig. 35). Incorporation of isostatic processes in FTB modeling alter kinematic and thermal paths, and provide modeled chronostratigraphy that can be correlated to synorogenic sediments.

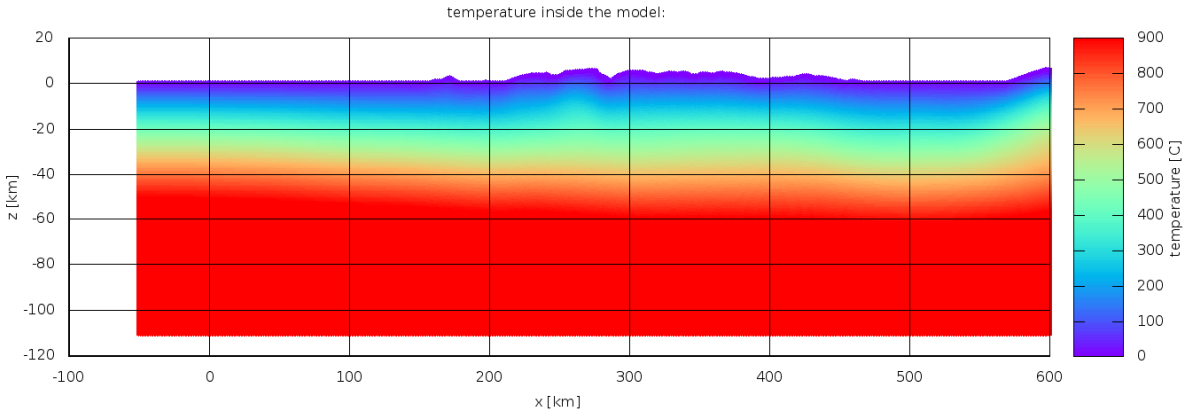

Figure 35. Thermal field plot from *Pecube* showing differences in thermal fields during SA shortening during the emplacement of basement thrust sheet B. Increased thermal gradients at 250-275 km (Decollement ramp location) are adjacent to decreased thermal gradients at 125 km and 200 km (SA synclinal basins).

6.2 COOLING SIGNALS IMPOSED BY LARGE BASEMENT THRUST SHEETS

Cooling ages in the Bolivian Andes reflect a first order signal resulting from the emplacement of basement thrust sheets. In our model the location of basement ramps through time focuses uplift, producing high topography, causing concentrated erosion, exhumation and thermochronometer cooling. The motion of material up the hinterland footwall ramp imparts the westward younging cooling signal recorded in EC backthrust belt samples. The eastward propagation of the basement (sheet A) hangingwall ramp forms a crustal-scale passive-roof duplex producing an eastward younging cooling pattern in the EC as material moves over this frontal hangingwall ramp. The combination of these basement ramps reproduces the triangular cooling pattern preserved in thermochronometer samples across the EC. The clustering of young (<15 Ma) AFT cooling ages in the central EC is a function of the location of the basement thrust that feeds slip into the SA. Previous interpretations of this recent cooling expressed as young AFT ages include: active deformation manifested as surface breaking faults or subsurface accretion (Norton and Schlungger, 2011); focused erosion driven by an increase in precipitation (Gillis et al., 2006; Barnes et al., 2012) and uplift over a basement ramp (Whipple and Gasparini 2014). Our modeling shows that the motion of crustal material over the basement sheet B ramp focuses 5-8 km of exhumation in this region resetting cooling signals in a westward younging pattern. The migration of these prominent basement ramps through time imparts a first order cooling signal evident in our model and matches the distribution of thermochronometer cooling ages in the EC.

6.3 LONG WAVELENGTH IMPOSED UPLIFT AND SUBSIDENCE

The discrepancy between the thickness of measured foreland basin fill in the SA to the thickness of modeled foreland basin strata produced solely by thrust loads highlights the need for imposed subsidence. Despite the high density (2900 kg/m^3) and high EET (30-90 km) used, predicted thicknesses of sedimentary strata in the SA were still significantly (>2km) too thin. We suggest that this discrepancy indicates the presence of dynamic subsidence in this region not accounted for in flexural modeling. In addition, the only way our modeling produces and maintains elevation is through an increase in structural elevation due to thrust faulting. Once thrust faulting ceases in the region, that region gradually subsides with time due to loading from uplift along distal ramps. Thus modeled elevations in the EC decrease slowly through time and do not match modern EC elevations mandating imposed uplift to match the modern elevation profile.

In retroarc foreland basin systems, dynamic subsidence, related to viscous coupling of the mantle wedge, can increase the load experienced by the foreland and facilitate the increased preservation of foreland basin sediment (DeCelles, 2012). The thickness and distribution of sedimentary basins in retroarc subduction zones requires an additional load (dynamic subsidence) that can alter the depth and location of foreland basin deposits (Mitrovica et al., 1989; Gurnis, 1993; Catuneanu, 2014; DeCelles 2012). Accumulation of sedimentary packages in the North American Cordillera strongly suggests a component of dynamic subsidence in addition to flexural subsidence related to thrust-fault loading (Gurnis, 1992; Gurnis, 1993; Painter et al., 2013). Subsidence of ~350 m was imposed on the model in the foreland during each deformation step adding -2.2 km of increased subsidence (Fig. 11) during SA deformation to reproduce the thickness and extent of Tertiary basin fill. While the time interval selected to

impose the additional load to the foreland basin can affect the fit of the modeled foreland basin sediment, this time interval post-dates the ages of the 1 km thick sections correlated to basin geochronology samples. The additional subsidence in the foreland is necessary to replicate geologic constraints of the cross section (thick SA synclines) and predict particle paths.

Imposed uplift in the EC and AP was necessary to maintain the high elevations present in the hinterland of the Andes today. Several arguments against flexural support of the Andean Plateau have been suggested including: Airy isostatic compensation due to a thick crustal column (Beck, 1998), the presence of weak lower crust (Isack, 1988), delamination processes invoking recent (<4Ma) rapid uplift (Garzione et al., 2006) and thickening of the EC and AP by lower crustal material displaced to the west due to SA shortening (Isack, 1988; Lamb, 2011; Eichelberger et al., 2015). Crustal thicknesses of ~70 km beneath the AP are consistent with Airy-type isostasy indicating the high elevations in the hinterland are supported by thick crust and not the EET of the lithosphere (Beck et al., 1996). Additionally, the high magnitude of documented upper crustal shortening in the Bolivian Andes (McQuarrie et al., 2002; McQuarrie et al., 2008; Eichelberger et al., 2013) must be balanced by lower crustal shortening (not specifically modeled in this study) and thickening producing an excess of lower crust that must be accounted for (e.g. delamination or lower crustal flow) (Garzione et al., 2006; Eichelberger et al., 2015). Since these processes responsible for the modern elevation of the hinterland of the Bolivian Andes cannot be flexurally modeled, an approximately 500 m imposed uplift in the EC and AP is implemented during each step of SA deformation to reproduce modern topographic expression of the FTB and maintain high elevation in the hinterland (Fig. 12). This vertical adjustment does not change the relationship of modeled particle paths to the surface but only changes the absolute elevation of the hinterland in the model after the initiation of basement

thrust sheet B. Models with EC and AP imposed uplift are nearly identical when compared with the same model without the hinterland adjustment (not shown). When compared specifically in each zone, the average A/He is 0.36 Ma younger while the averaged AFT cooling age is 0.54 Ma younger with the imposed subsidence and uplift. In the EC the ZFT predicted cooling ages are 1.57 Ma older with the imposed flexure. These differences may be related to the surface temperature gradient (lapse rate 5.3 C°/km) in the model causing higher elevation samples to cool through isotherms earlier or the advection of warm material as exhumation occurs above active ramps.

6.4 MODIFICATION OF THERMAL FIELDS VIA FLEXURAL SUBSIDENCE AND EROSIONAL ADVECTION

Thermochronometric modeling indicates different exhumation magnitudes are necessary to reset the same thermochronometer based on the location of the sample in the fold-thrust-belt-foreland basin system. Cooling of the AFT system recorded in samples across the EC show systematic age clustering; 40-50 Ma in the backthrust belt and 5-19 Ma in the core of the EC. These age populations indicate an early exhumation event that is recorded in the old samples and recent exhumation that partially reset some AFT samples that still retain an early component age (Benjamin et al., 1987; Barnes et al., 2012; McQuarrie et al., 2008). In kinematic scenario 1 (kinematics proposed by McQuarrie et al., 2008) 50 Ma start model, early thrust faulting in the EC induces 1-2.5 km of exhumation causing some partial resetting in the AFT system (Fig. 12b). These partially exhumed samples are subsequently buried by approximately 3 km of sediment, as adjacent faulting drives subsidence, before they are thrust over the basement thrust hangingwall

ramp triggering 9 km of exhumation (Fig. 12e). Although the large magnitude exhumation occurs between 32 and 25 Ma in the model (Figs. 12d and 12e) final predicted ages above the EC duplex record early deformation induced exhumation at ~45 Ma (Fig. 12h at 200 km). AFT samples in the EC backthrust belt that are never covered with significant sediment are partially reset with as little as 3.4 km of exhumation (Fig. 12b) and fully reset with 4 km of exhumation (Fig. 12c). These unique differences in amount of exhumation necessary to reset AFT systems in the EC are related to: the compression of isotherms above major faults (minimum exhumation 4 km) due to the advection of warm material; and blanketing (the depression of isotherms in rapidly accumulating basins; Husson and Moretti, 2002) that help to preserve protracted exhumation histories (McQuarrie and Ehlers, 2015).

In the SA for kinematic scenario 1, modeling predicts 4 km of exhumation is required for partial resetting of the AFT systems (easternmost SA thrust sheet Fig. 12h) and over 4.5-5 km of exhumation is needed to cause full resetting of the AFT system (central and western SA thrust sheets Fig. 13h). These exhumation magnitudes are approximately 1 km greater than exhumation needed to reset AFT systems in the EC backthrust belt upon which minimal sediment was deposited. The revised kinematic scenario (kinematic scenario 2) requires similar amounts of exhumation to set predicted AFT cooling in the EC backthrust belt (3-4 km) but models SA sample points differently. The revised kinematic scenario increased SA shortening by 14 km and imposed a long wavelength subsidence, increasing subsidence and exhumation magnitudes experienced by sample points. This scenario invokes 5.7-6.0 km of exhumation in the eastern and western SA thrust sheets with no resetting of either AFT system (Fig. 17). The westernmost thrust sheet in the SA only becomes fully reset with the 55 Ma start constant velocity model and the higher radiogenic heat production value (0.7 $\mu W/m^3$). Predicted AFT in the central thrust

sheet in the SA becomes fully reset, in the revised kinematic scenario, with 7.0 km of exhumation. While these magnitudes are high, samples reach their maximum depth during the rapid (imposed) subsidence period and are subsequently exhumed. Despite exhumation magnitudes being higher in the revised kinematic scenario, SA basins are thicker, amplifying the blanketing effect and predicting less resetting of the AFT system – which matches the range of resetting in the data; the most exhumed samples contain a young reset component but also include older, partially reset grains (Barnes et al., 2006). The effects of erosion and sedimentation on the near surface thermal field is notable in foreland basin systems that experience rapid sedimentation such as the Apennines where heat flow data from the foreland is half as high as in the frontal thrusts (Husson and Moretti, 2002). Due to this effect, velocity models with low rates of deformation (and sedimentation) predict increased resetting of AFT samples in SA thrust sheets.

Thermochronometric models of linked fold-thrust-belt-foreland basin systems that attempt to predict hydrocarbon maturation require kinematics that account for isostatic compensation, basin formation and realistic fault networks. Variations in predicted thermochronometer cooling between the two kinematic scenarios presented highlight the effects of sedimentation and kinematics on thermokinematic modeling results from the foreland (Fig. 13). Fluctuations in magnitude or rate of subsidence in modeled foreland basins can affect predicted thermochronometer cooling signals by altering kinematic paths and thermal regimes (Husson and Moretti, 2002). Kinematic solutions that oversimplify fault network geometries, and do not take into account the evolution of a fault network through time, inaccurately predict thermochronometer cooling and hydrocarbon maturation. Thrust systems typically exhibit ramp-flat geometries that are fed by displacement on basement structures that may migrate through

time (Boyer and Elliott, 1982). These larger basement structures will have a greater effect on the magnitude and distribution isostatic subsidence than more proximal narrower structures. Fault network geometry and isostasy are important variables controlling kinematics and near surface thermal-field evolution in thermokinematic models that utilize balanced cross sections for kinematic paths (McQuarrie and Ehlers, 2015; Husson and Moretti, 2002). Thermochronometer cooling and hydrocarbon maturation predictions that stem from kinematic models that do not account for isostatic loading or realistic fault networks (Erdos et al., 2014; Mora et al., 2015) must be scrutinized when assessing the viability of model results.

6.5 COMPARISION OF MODELED DEFORMATION RATES TO PUBLISHED DATA

The sensitivity of modeled thermochronologic data to the age at which deformation initiates indicates that northern Bolivian EC started deforming at 50 Ma and may have begun as early as 55 Ma. This initiation date is >15 Ma earlier than interpretations that dominantly rely on synorogenic sediment data (Sempere, 1990; Allmendinger, 1997; Jordan, 1997). While the incorporation of synorogenic sediment ages is important in placing temporal bounds on FTB development, linking these constraints to a sequentially deforming kinematic model allows for the incorporation of structural, thermochronometric, and geomorphic datasets. When kinematics derived from balanced cross sections are linked with geodynamic principles of foreland basin migration it becomes apparent that sediments shed from the earliest deformational phases are rarely preserved in the associated foreland basin systems, especially if shortening magnitudes are large (DeCelles, 2012). Therefore, synorogenic sediment ages in FTB systems should not be

interpreted as indicators of the initiation of deformation but must be linked to fault networks derived from balanced cross sections and foreland basin evolution models to palinspastically restore these basins in their original depositional location.

The early initiation of crustal shortening suggested in this study also predates interpretations made using AFT, ZFT, K/Ar, and $^{40}Ar/^{39}Ar$ thermochronometer cooling ages from Triassic plutons exhumed in the EC (Benjamin et al., 1987; Farrar et al., 1988; Gillis et al., 2006). Similar to interpretations based on synorogenic sediment ages, rapid cooling of thermochronometers must be spatially linked to the kinematic evolution of the orogen to understand the context of the reported ages. Age elevation plots were used to identify two ZFT trends that intersect at 45 Ma to argue for a change in exhumation rates at this time (Benjamin et al., 1987). Biotite and muscovite K/Ar dates and $^{40}Ar/^{39}Ar$ step-heating of EC samples identified minimum age plateaus at 38 Ma which were interpreted as a regionally extensive (400 km along strike) thermal event associated with early deformation in the core of the EC (Farrar et al., 1988). More comprehensive analysis of $^{40}Ar/^{39}Ar$ and fission track thermochronology by Gillis et al., (2006) used the overlapping systems to corroborate interpretations that cooling began at 45-40 Ma. These thermochronometry analyses suggest earlier deformation than sediment geochronology but are modeled in one-dimensional space and assume a steady 30 °C geothermal gradient which calculate an exhumation history independent of a structural context. When accounting for topographic evolution, a minimum amount of shortening is required to impose sufficient uplift, erosion and exhumation to reset thermochronometer cooing signals in the EC (Fig. 12b). The delay between the onset of deformation and oldest ZFT signal is 8 Ma in the 50 Ma constant velocity model (Fig. 12h). Additionally after rocks have been uplifted erosion rates may be significantly lower than shortening rates. In the Himalayas, GPS derived shortening rates

of ~20 mm/yr are nearly an order of magnitude greater than exhumation rates (2-5 mm/ya) (Galy et al., 2001; Blyth et al., 2007; Clift et al., 2008). Modern exhumation rates for the central Andes have been calculated by inverse thermal modeling of AFT ages determining rates of ~2-6 mm/yr (Safran et al., 2006). Long-term average rates of exhumation were calculated along the Beni cross section using cross section estimates and thermochronometry estimates identifying rates from ~0.1-0.6 mm/yr (McQuarrie et al., 2008). The discrepancy in erosion rates identifies the uncertainty in the rates of exhumation that would be associated with minimal erosion rates. The lag time between deformation and exhumation induced cooling is evident in modeled ZFT cooling signals that show an 8 Ma gap between the age of model initiation and final ZFT predicted cooling ages (Fig. 12h).

The acceptable velocity envelope for the Beni modeled section (Fig. 36) implies relatively constant rates of shortening through time with permissible rates of deformation that mimic a sine wave curve, increasing at ~15 Ma and reaching a peak at 11 Ma. Initiation of deformation in the SA is determined by the initial motion of basement thrust sheet B, facilitating exhumation above the hanging and foot wall ramps of this basement thrust and resulting in focused exhumation in the IA duplex in Ordovician-Silurian age rocks, westward migrating exhumation in the EC, and exhumation above select SA footwall ramps. Erosion of Mesozoic through Ordovician strata at the eastern edge of the EC is a result of motion on basement sheet B and must predate the deposition of the Cangalli Formation. These constraints indicate the need for rapid deformation soon after the initiation of SA shortening (e.g. hiatus, hybrid and sine models). This elevated rate of shortening during SA deformation falls within the range of modern GPS rates of shortening in the SA (9-13 mm/yr) (Bevis et al., 2001; Klotz et al., 2001; Brooks et al., 2011) and SA pulsed shortening rates from southern Bolivia that fluctuate between

0-5 mm/yr to 11-13 mm/yr from 9 Ma to present (Echavarria et al., 2003). Additionally, the modern rainfall gradients (Fig. 6) are interpreted to have been established at 15-11 Ma, potentially inducing orographically enhanced exhumation rates (Barnes et al., 2012) that could in turn increase SA shortening rates to replace eroded material in the deforming wedge and facilitate the westward motion of the basement decollement ramp. Modeling of Central Andean orocline rotation suggests an increase in SA shortening (~20 km) along the Beni cross section due to vertical axis rotation that is similar in magnitude to the 14 km added to fit the EC thermochronometer trends in this study (Eichelberger and McQuarrie, 2015). Thus erosion above the newly developed basement thrust sheet ramp (B) at the initiation of SA shortening links exhumation signals in the IA and EC to SA thrust sheet emplacement and the age and location of this exhumation is the signal that is most sensitive to the age and rate of SA deformation

The modeled age of SA initiation for models with constant velocities are 11 Ma for the 30 Ma model, 15 Ma for the 40 Ma model, 19 Ma for the 50 Ma model and 20 Ma for the 55 Ma model. The 50 and 55 Ma start constant velocity models are selected as the best fit constant velocity models based on the AFT cooling trends in the EC and IA and the intersection of sediment geochronology ages. Early SA deformation at 19-20 Ma is consistent with previous HeFTy modeling of the AFT data which indicate rapid exhumation occurred between 4 Ma and 19 Ma (Barnes et al., 2006; McQuarrie et al., 2008). In addition, young AFT samples in the EC record 8-21 Ma cooling that are a direct function of the rate of SA deformation (and westward migration of the basement ramp) also supporting the possibility of early SA initiation. While constant velocity models with a later start date (40-30 Ma) also match this young AFT component in the EC, sediment geochronology ages, ZFT samples in the EC, and the young IA

ages are not correctly predicted by later start date models. Hiatus velocity models predict decreasing ages of SA initiation 15 Ma, 12 Ma and 8 Ma for models with increasing hiatal periods (25-15 Ma, 25-12 Ma, and 25-8 Ma). The hiatus from 25-15 Ma is the preferred hiatus velocity model, matching 65% of AFT cooling samples in the EC and 62% of AFT ages in the IA and intersecting one of the Cangalli Formation geochronology samples, agreeing with previous interpretations of SA initiation at 15 Ma (Barnes et al., 2006; McQuarrie et al., 2008; Eichelberger and McQuarrie, 2015). Models with longer hiatal periods intersect less AFT samples in the IA and increasingly miss the erosional constraint of the Cangalli Formation. The Sine 55 Ma start velocity model predicts a slightly later SA shortening initiation at 12 Ma with a peak in maximum shortening rates of 11 mm/yr at ~5 Ma – but Cangalli erosion is 2 Myr to young. Initiation of SA deformation at 20 Ma is the oldest SA initiation age that best matches the data and is 11 Ma older than the 9 Ma start date suggested by Echavarria et al., (2003) from sediment accumulation curves in southern Bolivia. Both hybrid velocity models have similar rates of shortening after 40 Ma and predict SA initiation at 15 Ma with a rapid increase from ~3 mm/yr to ~11 mm/yr by 11 Ma to uplift and erode Ordovician rocks in the EC facilitating deposition of the Cangalli Formation. The high magnitude of SA shortening needed to uplift and exhume Ordovician rocks in the EC allowing the deposition of the Cangalli Formation indicates that either an old (~20 Ma) start date or a young (15 Ma) initiation of deformation coupled with an initially high rate of deformation is necessary to meet this wedge-top constraint. Young A/He samples form the SA record recent exhumation since 7 Ma (Lease and Ehlers, 2014 abstract), which is accurately predicted by all velocity models tested. Combined, these constraints suggest that SA deformation initiated between 20 and 15 Ma, inducing AFT cooling in the EC and IA. A young start date (15 Ma), with rates of shortening peaking around 11 Ma, may be a function of

orographically enhanced exhumation rates (Barnes et al., 2012) linked to attainment of threshold elevations (>75% of modern). Modern shortening rates from GPS stations located in the actively deforming region of the FTB are slightly higher (9-13 mm/yr) than the modern rate predicted by the preferred shortening velocity envelope (Fig. 36) (Bevis et al., 2001; Klotz et al., 2001; Brooks et al., 2011).

Deformation in the IA is synchronous with EC deformation with early partially reset AFT ages of 30-60 Ma and young (<15 Ma) cooling (Barnes et al., 2006; McQuarrie et al., 2008; Barnes et al., 2012). Early cooling ages in IA suggest early initial deformation in the region (>25 Ma) while the kinematics from sequential cross section restorations indicate final IA deformation would predate SA deformation (~15 Ma) (McQuarrie et. al., 2008). Preferred velocity models all predict a similar onset of significant IA deformation between 28-30 Ma. Exhumation the IA continues after deformation in the zone is complete as material moves over the basement thrust sheet ramps. Predicted AFT cooling in the IA is sensitive to changes in SA initiation and suggest initial motion on thrust sheet B started between 20 Ma and 15 Ma. This suggests a window of IA deformation from 28-30 Ma to 15-20 Ma.

Previous estimates of shortening rates are based on total shortening magnitudes and the estimated age over which that shortening occurred. Using a section across southern Bolivia (21°S; 450 km south) and combining cross section shortening estimates, synorogenic sediment accumulation curves preserved in the SA and a suite of AFT cooling ages, Oncken et al., (2006) proposed shortening rates that varied through time (Fig. 36 blue line; Oncken et al., 2006). Temporal constraints of the model are strongly influenced by Oligocene (Sempere, 1990) and Miocene synorogenic deposits (Uba et al., 2006), as well as a suite of AFT data across the EC and IA that range from 40-20 Ma, with the oldest ages (40-33 Ma) focused in the core of the EC

and a cluster of 30-20 Ma ages to the east and west (Schueber et al., 2006). Emphasis on the Oligocene basin deposits combine with the aerial extent of the 30-20 Ma ages biased the model towards a high shortening rate during the Oligocene. SA shortening magnitude was quantified at 21°S (90 km) but the age of shortening was taken from the well-dated section at 22.5 °S, where 60 km of shortening occurs over the last 9 million years (Echavarria et al., 2003). Due to these factors, the strain accumulation model (Oncken et al., 2006) under predicts rates of shortening from 55-50 Ma to 33 Ma and over predicts rates of shortening from 33 Ma to 15 Ma when compared to the acceptable shortening rate envelope for northern Bolivia (15-17°S). Although the strain accumulation model is centered 500 km south of our modeled section, this comparison identifies key differences in the modeling techniques and illustrates how robust fault network kinematics and flexural isostasy modeling have the potential to significantly alter shortening rate results.

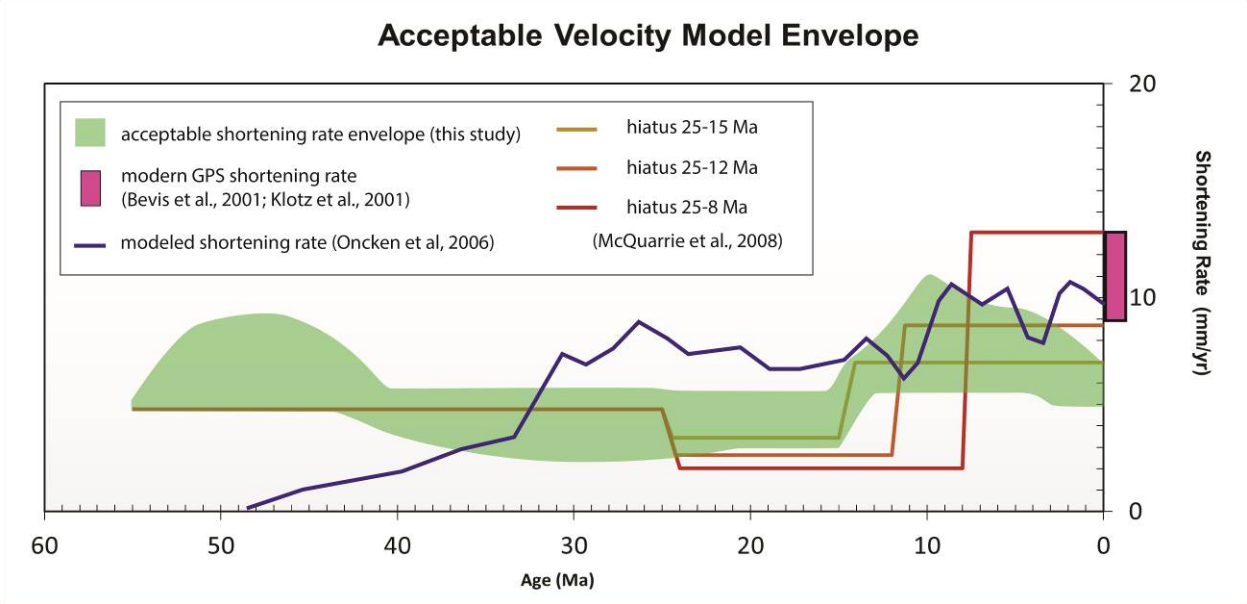

Figure 36. Shortening rate diagram with acceptable shortening rate envelope (this study), modern GPS rates of shortening (pink box) (Bevis et al., 2001; Klotz et al., 2001), modeled shortening rate from 21°S (blue line) (Oncken et al., 2006), hiatus models proposed by McQuarrie et al., (2008).

6.6 KINEMATIC IMPLICATIONS FOR THE COPACABANA CROSS SECTION

Temporal constraints determined from modeling of the Beni cross section indicate the emplacement of basement thrust sheet A began at 50 Ma (possibly as early as 55 Ma) feeding slip into the EC forethrust and backthrust belt. The Oligocene Aranjuez and Penas Formations were deposited synchronously with the Salla Formation indicating deformation and erosion along the Copacabana cross section must reach the western EC by 27 Ma. The kinematic solution for the cross section requires a minimum of 42 km of backthrust shortening prior to 27 Ma. We interpret EC forethrusting and some IA thrusting also may occur during this time period. Late-stage faulting of the EC (6.5 km) occurs after EC backthrust faulting is complete and must significantly postdate the deposition of the Aranjuez and Penas Formations (27-25 Ma) facilitating the full emplacement of the backthrust sheet at the AP-EC contact. Velocity modeling of the Beni cross section favors initiation of basement thrust sheet B at 15 Ma (possibly as early as 20 Ma) facilitating distributed cooling patterns in the EC, IA and SA as material is exhumed over the new basement ramp and in select SA thrust sheets. Therefore, SA shortening along the Copacabana cross section (68 km) is partitioned into a temporal window from 20-15 Ma to present agreeing with recent modeling of the region (Eichelberger and McQuarrie, 2015). The 10.2 km of shortening in the AP is assumed to have occurred since 15 Ma due to the young component AFT ages of 8.7 Ma and 4.2 Ma located 25 km south of the Copacabana cross section in the AP (Barnes et al., 2006). The shortening rate during the past 20-15 Myr, accounting for AP and SA deformation, is interpreted to be constant at 3.9-5.2 mm/yr. If EC and IA shortening (164 km) predate the initiation of SA and AP shortening (78 km) at 20-15 Ma shortening rates of 4.1-5.5 mm/yr from 50-55 Ma to 20-15 Ma would account for the emplacement of basement sheet A and late-stage EC faulting. The single hinterland wedge-top constraint and the ability of

the kinematic solution to feed slip into the forethrust or backthrust belt inhibits our ability to resolve variable rate models, thus we interpret a constant rate of deformation of 4.1-4.8 mm/yr across the Copacabana cross section. Similar to the Beni cross section an acceleration of deformation is possible, after the initiation of basement thrust sheet B (20-15 Ma), to facilitate the erosion of lower Paleozoic units to fit the Cangalli Formation geochronology ages of 9-7 Ma in the eastern EC. Timing of deformation was determined through flexural and themochronometric modeling of the Beni balanced cross section (McQuarrie et al., 2008) and was extrapolated along strike to the Copacabana cross section using basement thrust sheet initiation to link the cross sections. Although sediment geochronology and AFT thermochronology were incorporated to interpret rates of deformation along the Copacabana cross section, sequential forward modeling with applied isostasy would further constrain proposed rates of shortening. Suggested deformation rates for the Copacabana cross section are slightly lower than the acceptable rates of deformation determined for the Beni cross section due to the decreased magnitude of shortening in northernmost Bolivia.

7.0 CONCLUSIONS

This research focuses on mapping and development of the Copacabana cross section and complementary isostatic and thermochronometric modeling of the adjacent Beni cross section (McQuarrie et al., 2008) in the northern Bolivian Andes. These ~300 km long crustal cross sections traverse the Andean FTB from the AP to the Beni plain. Geometries and kinematics from balanced cross sections can be used as inputs for isostatic and thermochronometric models that reveal the geodynamic evolution of the FTB-foreland basin system, timing and rates of shortening and identifies possible inaccuracies with the modeled cross section.

7.1 COPACABANA CROSS SECTION

New geologic mapping of the northern Bolivia and southern Peruvian regions of the Andean FTB highlighting the northward decrease in the width of the SA and Ordovician EC countered by the increased width of the IA. Geometry and kinematics of the Copacabana cross section is controlled by basement thrust sheets that feed slip to the surface and are correlated to basement thrust sheets in the Beni cross section. Total magnitude of shortening is 242 km, 35 km less than the Beni cross section 50-100 km to the south. This study agrees with previous interpretations of a sequential increase in the magnitude of shortening towards the south to as

high as >320 km south of the Santa Cruz bend in central Bolivia (McQuarrie, 2002; McQuarrie et al., 2008; Eichelberger et al., 2013). Despite the decrease in total shortening there is an increase in percent shortening, from 40% along the Beni cross section to 43% along the Copacabana cross section. Shortening magnitudes in the IA and SA increase in the north implying higher total foreland shortening along the Copacabana cross section complementing increased SA shortening along the Beni modeled section to move the basement ramp west and match young AFT thermochronometer ages in the EC. A constant rate of 4.1-4.8 mm/yr that initiated at 55-50 Ma is proposed along the Copacabana cross section by linking basement thrust sheet initiation form the Beni modeled cross section in conjunction with sediment geochronology and thermochronometer cooling in northernmost Bolivia.

7.2 BENI CROSS SECTION MODELING

The method of deriving particle paths for thermokinematic models from sequentially deformed, isostatically compensated, balanced cross sections facilitates the creation of an integrated model that predicts thermochronometer cooling in the FTB and the ages of modeled sediment in adjacent foreland basins. The magnitude of SA deformation proposed by McQuarrie et al., (2008) resulted in a mismatch between predicted and measured AFT cooling ages in the EC prompting the development of an alternate model with increased shortening, facilitating the westward motion of the basement ramp by 14 km. The increased SA shortening scenario significantly increased the match of predicted AFT age to measured ages from 0% to 92% in some cases.

Insufficient SA basin deposits and EC low elevations produced in the first round of flexural models, mandated an imposed long wavelength subsidence (-2.2 km) in the foreland and uplift in the hinterland (3-4 km). We argue that the need for this imposed subsidence mandates a significant component of dynamic subsidence influenced the foreland resulting from viscous coupling between mantle wedge and the subducting oceanic plate (DeCelles, 2012) particularly over the last 15 Myr. Imposed uplift in the hinterland may be related to the attainment of Airy isostasy (Beck et al., 1998), via lower crustal flow (Eichelberger et al., 2015) or delamination rebound (Garzione, 2006). Regardless of the mechanism driving the process, flexural isostasy due to thrust belt stacking does not account for the full subsidence history recorded in the northern Bolivian Andes foreland basin system, and cannot maintain the high elevations in the hinterland.

Modeled thermochronometry cooling patterns indicate that deformation initiated in the EC at 50-55 Ma (depending on the thermal parameters). Early initiation is needed to reproduce EC 40-50 Ma AFT and 38-46 Ma ZFT sample ages and correctly predict the age of synorogenic basin sediments and wedge-top sediment windows. A set of variable rate deformation models were found to comparably reproduce chronologic constraints along the modeled cross section and were used to define an acceptable rate of shortening envelope. A 50 Ma start with a marked slowing of deformation between 25-15 Ma, $Ao=0.7\mu W/m^3$ was shown to most accurately fit the measured cooling ages in the EC and the chronologic constraints as a whole. Although this is the most accurate fitting model, the model deformation rate falls within the acceptable rate of deformation envelope. Variable rate velocity models that fit the data have a sinusoidal character with the first pulse initiating shortening at 50-55 Ma followed by a window of decreased rates of shortening and a second pulse of more rapid rates from 15-11 Ma. Initiation of SA deformation

is ~15 Ma in most acceptable velocity models but may have occurred as early as 20 Ma. The initiation of SA deformation determined in this study is 6-11 Myr earlier than ages identified in southern Bolivia (9 Ma, Echavarria et al., 2003), which are often used in geodynamical models (Garzione et al., 2008; DeCelles et al., 2009).

Accounting for isostasy in the kinematics used for inputs to thermochronometric models is evident by the variation in exhumation necessary to reset the same chronometer in the foreland versus the hinterland. An extra ~1 km of exhumation is needed to reset AFT in the foreland when compared to the sample in the hinterland for kinematic scenario 1 (McQuarrie et al., 2008). An additional 3 km of exhumation is necessary to reset AFT in the foreland when compared to the hinterland in the revised kinematic scenario where rapid subsidence in the foreland amplifies the blanketing effect experienced by buried samples (Husson and Moretti, 2002). These results identify the need to account for the transient foreland basin migration history across a FTB when modeling particle paths for thermochronometric modeling. The integration of synorogenic sediment geochronology in thermochronometric models provides an additional source of chronologic constraints that can improve model interpretations (Robinson and McQuarrie, 2012). Correlation of the model to chronologic datasets identifies a window of acceptable velocities of deformation that can similarly reproduce chronologies of the samples. Although constant rate models can fit the chronology, need for elevated rates of deformation during SA shortening in the variable rate models is the result of the Cangalli Formation and is independent of thermal parameters.

This study presents new mapping, cross section creation, and cross section modeling of the northern Bolivian Andes FTB defining acceptable initiation and rates of shortening. Forward modeling deformation from restored cross sections with applied isostasy and erosion provide a

geodynamic solution describing the evolution of the linked fold-thrust-belt-foreland basin that can incorporate mapped geology, thermochronology, sediment geochronology, geomorphology, and geophysical information in a single model. Results from this study suggest early initial deformation in the EC at 50-55 Ma and lower rates of deformation during the Oligocene with potentially increased rates of shortening from 15-11 Ma. The timing of basement thrust sheet initiation was used to correlate timing from the Beni modeled to the Copacabana balanced cross sections. This research provides insights into the erosion, sedimentation, and geomorphic evolution of the northern Bolivian Andes.

BIBILIOGRAPHY

Allmendinger, R. W., T. E. Jordan, S. M. Kay, and B. L. Isacks 1997. The evolution of the Altiplano-Puna Plateau of the central Andes, Annual Review Earth Planetary Science 25, 139–174, doi:10.1146/annurev.earth.25.1.139.

Babeyko, A.Y., S.V. Sobolev, 2005. Quantifying different modes of the late Cenozoic shorting in the central Andes. Geology 33, 8, 621-624 doi:1130/G21126.1.

Baby, P., R. Limachi, I. Moretti, E. Mendez, J. Oller, B. Guiller, and M. Specht, 1995. Petroleum system of the northern and central Bolivian sub-Andean zone. In: Tankard, A.J., Suarez, R., Welsink, H.J. (Eds.), Petroleum Basins of South America: American Association of Petroleum Geologists Memoir 62, 445–458.

Barnes, J.B., T.A. Ehlers, N. McQuarrie, P.B. O'Sullivan, and J.D. Pelletier, 2006. Variations in Eocene to recent erosion across the central Andean fold-thrust belt, northern Bolivia: Implications for plateau evolution: Earth and Planetary Science Letters 248, 118–133, doi:10.1016/j .epsl.2006.05.018.

Barnes, J.B., and T.A. Ehlers, 2009. End member models for Andean Plateau uplift. Earth- Sci. Rev. 97, 105–132.

Barnes, J. B., T. A. Ehlers, N. Insel, N. McQuarrie, Paulsen, C. J., 2012. Linking orography, climate, and exhumation across the Central Andes, Geology 40, 12, 1135-1138.

Benjamin, M.T., N.M. Johnson, and C.W. Naeser, 1987. Recent rapid uplift in the Bolivian Andes; evidence from fission-track dating. Geology 15, 680–683.

Beck, S.L., G. Zandt, S.C. Myers, T.C. Wallace, P.G. Silver, and L. Drake, 1996. Crustal thickness variations in the central Andes. Geology 24, 407–410.

Blythe, A.E., D.W. Burbank, A. Carter., K. Schmidt, and J. Putkonen, 2007. Plio-Quatenary exhumation history of the central Himalaya: 1. Apatite and zircon fission-track and Apatite [U-Th]/He data. Tectonics 26, TC 3002.

Bollinger, L., P. Henry, and J.-P. Avouac, 2006, Mountain building in the Nepal Himalaya; Thermal and kinematic model, Earth and Planetary Science Letters 224, 1, 58-71.

Boyer, S.E, Elliott, D., 1982. Thrust systems, American Association of Petroleum Geologists Bulletin 66, 9, 1196-1230.

Braun, J., 2003. Pecube: A new finite-element code to solve the 3D heat transport equation including the effects of a time-varying, finite amplitude surface topography, Computer Geosciences 29, 787-794.

Catuneanu, O., 2004, Retroarc foreland systems – evolution through time, Journal of African Earth Sciences 38, 225-242.

Célérier, J., T.M. Harrison, O. Beyssac, F. Herman, W.J. Dunlap, and A.A.G. Webb, 2009, The Kumaun and Garwhal Lesser Himalaya, India: Part 2. Thermal and deformation history, Geological Society of America Bulletin, 121, 9-10, 1281-1297.

Clift, P.D., K.V. Hodges, D. Heslop, R. Hannigan, K. Van Long, and G. Calves, 2008. Correlation of Himalayan exhumation rates and Asian monsoon intensity. Nature Geosciences 1, 875-880.

Coney, P. J, and C.A. Evenchick, 1994. Consolidation of the American Cordilleras, Journal of South American Earth Sciences 7, ¾, 241-262

DeCelles, P. G., M. N. Ducea, P. Kapp, and G. Zandt 2009. Cyclicity in Cordilleran orogenic systems, Nature Geoscience 2, 251–257, doi:10.1038/ ngeo469.

DeCelles, P. G., 2012. Foreland basin systems revisited: variations in response to tectonic setting, *In:* Tectonics of Sedimentary Basins: Recent Advances, First Edition. Edited by C. Busby, Azor, A., Blackwell Publishing Ltd., 405-426.

Dunn, J.F., K.G. Hartshorn, and P.W. Hartshorn, 1995. Structural styles and hydrocarbon potential of the sub-Andean thrust belt of southern Bolivia. In: Tankard, A.J., Suarez, R., Welsink, H.J. (Eds.), Petroleum Basins of South America: American Association of Petroleum Geologists Memoir 62, 523–543.

Echavarria, L., R. Hernandez, R. Allmendinger, and J. Reynolds, 2003. Subandean thrust and fold belt of northwestern Argentina: Geometry and timing of the Andean evolution. AAPG bulletin 87, 6, 965-985.

Ehlers, T.A., 2005. Crustal thermal processes and thermochronometer interpretations, Reviews in Mineralogy and Geochemistry 58, 315-350.

Eichelberger, N., and N. McQuarrie, 2015, Kinematic reconstruction of the Bolivian Orocline, Geosphere 11, 2, 445-462.

Eichelberger, N., N. McQuarrie, T.A. Ehlers, E. Enkelmann, J.B. Barnes, and R.O. Lease, 2013. New Constraints on the chronology, magnitude, and distribution of deformation within the central Andean orocline, Tectonophysics 32, 1432-1453. doi:10.1002/tect.20073

Erdös, Z., P. van der Beek, and R.S. Huismans, 2014. Evaluating balanced section restoration with thermochronology data: A case study from the Central Pyrenees, Tectonics, dio:10.1002/2013TC003481.

Farrar, E., A.H. Clark, D.J. Kontak, and D.A. Archibald, 1988. Zongo-San Gaban Zone: Eocene foreland boundary of the central Andean orogen, northwest Bolivia and southeast Peru. Geology 16, 55–58.

Galy, A., C. France-Lanard, 2001 Higher erosion rates in the Himalaya: Geochemical constraints on riverine fled

Garzione, C.N., P. Molnar, J. Libarkin, and B. MacFadden, 2006. Rapid late Miocene rise of the Bolivian Altiplano: evidence for removal of mantle lithosphere. Earth and Planetary Science Letters 241, 543–556.

Garzione, C.N., Hoke, G.D., Libarkin, J.C., Withers, S., MacFadden, B., Eiler, J., Ghosh, P., Mulch, A., 2008. Rise of the Andes, Science 320, 1304-1307.

Gasparini, N. M., K. X. Whipple, 2014. Diagnosing climatic and tectonic controls on topography: Eastern flank of the northern Bolivian Andes, Lithosphere, doi:10.1130/L322.1

Gil Rodriguez, Willy Fernando, 2002, Evolution Lateral de la Deformacion de un Frente Origenico, Ejemplo de las Cuencas Subandinas Entre 0° Y 16° S, Sociedad Geologica Del Peru, Institut de recherché pour le dEveloppement (IRD), Publicacion Especial N° 4, 129.

Gilmore, M.E., Quantifying Deformation in the Eastern Bhutan Himalaya: Insights from flexural and thermal-kinematic models of a balanced cross section, [M.S. thesis]: University of Pittsburgh, 60.

Gillis, R.J., B.K. Horton, M. Grove, 2006. Thermochronology, geochronology, and upper crustal structure of the Cordillera Real: implications for Cenozoic exhumation of the central Andean plateau. Tectonics 25, TC6007, 1-22, doi:10.1029/2005TC001887.

Gonfiantini, R., M.A. Roche, J.C. Olivry, J.C. Fontes, G.M, Zuppi, 2001. The altitude effect on the isotopic composition of tropical rains, Chemical Geology 181, 147-167.

Gonzalez, M., E. Diaz-Martinez, and L. Ticlla, 1996. Comentarios sobre la estratigraphia del Silurico y Devonico del norte y centro de la Cordillera Oriental y Altiplano de Bolivia, paper presented at Simposio Sul Americano do Siluro-Devoniano, Anais, Ponta Grossa, Brazil.

Gotberg, N., N. McQuarrie, and V.C. Caillaux, 2010. Comparison of crustal thickening budget and shortening estimates in southern Peru (12–14°S): Implications for mass balance and rotations in the "Bolivian orocline". Geological Society of America Bulletin 122, 5/6, 727-742.

Gozzard, J. R., 2006. Image processing of ASTER multispectral data: Western Australia Geologic Survey, Record 2006/9, 1-51.

Grader, G. W., P. E. Isaacson, B. Mamet, and V. Davydov, 2003. Late Carboniferous to Middle Permian Copacabana Formation in Bolivia: cyclic carbonate-clastic successions in a back-arc setting, American Association of Petroleum Geologists Search and Discovery Article, 90012, 4.

Gurnis, M., 1992, Rapid Continental subsidence following the initiation and evolution of subduction, Science 255, 1556-1558

Gurnis, M., 1993. Depressed xontinental hypsometry behind oceanic trenches: A clue to subduction controls on sea-level change, Geology 21, 29-32.

Herman, F., P. Copeland, J.P. Avouac, L. Bollinger, G. Maheo, P. Le Fort. S. Rai, D. Foster, A. Pecher, K. Stuwe, P. Henry, 2010, Exhumation, crustal deformation, and thermal structure of the Nepal Himayaya derived from the inversion of thermochronological and thermobarometric data and modeling of the topography, Journal of Geophysical Research 115, B06407, dio:10.1029/2008JB006126.

Hindle, D., Kley, J., Klosko, E., Stein, S., Dixon, T., and Norabuena, E., 2002. Consistency of geologic and geodetic displacements during Andean orogenesis. Geophysical Research Letters 29. dio:10.1029/2001GL013757

Horton, B. K., and P. G. DeCelles, 1997. The modern foreland basin system adjacent to the Central Andes, Geology 25, 10, 895-898

Horton, B. K., and B. A. Hampton, 2001. Paleogene synorogenic sedimentation in the Altiplano plateau and implications for initial mountain building in the central Andes, Geologic Society of America Bulletin 113, 11, 1387-1400.

Horton, B. K., B. A. Hampton, B.N. L$_A$Reau, and E. Baldellon, 2002. Tertiary provenance history of the northern and central Altiplano (Central Andes, Bolivia): A detrital record of plateau-margin tectonics, Journal of Sedimentary Research, 72, 5, 711-726.

Horton, B. K., and P. G. DeCelles, 2003. Early to middle Tertiary foreland basin development and the history of Andean crustal shortening in Bolivia. Geologic Society of America Bulletin 115, 1, 58-77.

Horton, B. K., 2012. Cenozoic Evolution of Hinterland Basins in the Andes and Tibet, *In:* Tectonics of Sedimentary Basins: Recent Advances, First Edition. Edited by C. Busby, Azor, A., Blackwell Publishing Ltd, 427-444.

Horton, B. K., N. D. Perez, J. D. Fitch, and J. E. Saylor, 2014. Punctuated shortening and subsidence in the Altiplano Plateau of southern Peru: Implications for early Andean mountain building, Lithosphere, 10.1130/L397.1.

Husson, L., and I. Moretti, 2002. Thermal regime of fold and thrust belts – an application to the Bolivian sub Andean zone, Tectonophysics 345, 253-280.

Iaffaldano, G., Bunge, H.-P., Dixon T.H., 2006, Feedback between mountain belt growth and plate convergence. Geology 34, 893-896.

Isacks, B.L., 1988. Uplift of the Central Andean Plateau and bending of the Bolivian Orocline. Journal of Geophysical Research 93, 3211–3231.

Jordan, T.E. 1981. Thrust loads and foreland basin evolution, Cretaceous, western United States, American Association of Petroleum Geologists Bulletin 65, 12.

Jordan, T.E. 1995. Retroarc foreland and related basins, *in* Tectonics of Sedimentary Basins, Edited by C.J. Busby, and R.V. Ingersoll, Oxford, Blackwell Science, 331–362

Kennan, L., S. Lamb, and C. Rundle, 1995. K-Ar dates from the Altiplano and Cordillera Oriental of Bolivia: Implications for Cenozoic stratigraphy and tectonics: Journal of South American Earth Sciences 8, 163–186.

Kley, J., 1996. Transition from basement-involved to thin-skinned thrusting in the Cordillera Oriental of southern Bolivia. Tectonics 15, 763–775.

Lamb, S., 2011. Did shortening in thick crust cause rapid Late Cenozoic uplift in the northern Bolivian Andes. Journal of the Geologic Society of London 168, 1079-1092, dio:10:1144/0016-76492011-008.

Lease, R.O., T.A. Ehlers, 2014, Climatic and geodynamic influences on diachronous orogenic wedge propagation in the Central Andes, 2014 Geologic Society of America Annual Meeting in Vancouver, British Columbia, Abstract 1779/2000.

Leier, A., N. McQuarrie, C. Garzione, and J. Eiler, 2013. Sable isotope evidence for multiple pulses of rapid surface uplift in the Central Andes, Bolivia, Earth and Planetary Science Letters, 371-372, 49-58.

Leier, A., N. McQuarrie, B.K. Horton, and G.E. Gehrels, 2010, Upper Oligocene conglomerates of the Altiplano, Central Andes: the record of deposition and deformation along the margin of a hinterland basin, Journal of Sedimentary Research, 80, 750-762, doi:10.2110/jsr.2010.064

Lucassen, F., R. Beccio, R. Harmon, S. Kasemann, G. Franz, R. Trumbull, H.G. Wilke, R.L. Romer, and P. Dulski, 2001. Composition and density model of the continental crust at an active continental margin – the Central Andes between 21° and 27°S, Tectonophysics 341, 195-223.

McQuarrie, N., and P. DeCelles, 2001. Geometry and structural evolution of the Central Andean back thrust belt, Bolivia: Tectonics, 20, 669–692, doi:10.1029/2000TC001232.

McQuarrie, N., 2002. The kinematic history of the central Andean fold–thrust belt, Bolivia: implications for building a high plateau. Geol. Soc. Am. Bull. 114, 950–963.

McQuarrie, N., B. K. Horton, G. Zandt, S. Beck, and P. G. DeCelles, 2005. Lithospheric evolution of the Andean fold-thrust belt, Bolivia, and the origin of the central Andean plateau, Tectonophysics 399, 15 – 37, doi:10.1016/j.tecto.2004.12.013.

McQuarrie, N., J.B. Barnes., and T.A. Ehlers, 2008. Geometric, kinematic, and erosional history of the central Andean Plateau, Bolivia (15–17 degrees S). Tectonics, 27, TC3007.

McQuarrie, N., T.A. Ehlers, 2015, Influence of thrust belt geometry and shortening on thermochronometer cooling ages: Insights form thermokinematic and erosion modeling of the Bhutan Himalaya, Tectonics, doi:10.1002/2014TC003783, (in press).

McRae, L., 1990. Paleomagnetic isochrones, unsteadiness, and Uniformity of sedimentation in Miocene intermontane basin sediments at Salla, Eastern Andean Cordillera, Bolivia, Journal of Geology, 98, 479-500.

Meade, B.J., Conrad, C.P., 2008, Andean growth and the deceleration of South America subduction: time evolution of a coupled orogen-subduction system, Earth and Planetary Science Letters 275, 93-101.

Mitrovica, J.X., C. Beaumont, and G.T. Jarvis, 1989. Tilting of continental interiors by the dynamical effects of subduction, Tectonics 8, 1079-1094

Mora, A., W. Casallas, R.A. Ketcham, D. Gomez, M. Parra, J. Namson, D. Stockli, A. Almendral, W. Robles, and B. Ghorbal, 2014. Kinematic restoration of contractional basement structures using thermokinematic models: A key tool for petroleum system modeling. AAPG Bulletin, dio:10.1306/04281411108

Mosolf, J. G., B. K. Horton, M.T. Heizler, and R. Matos, 2011. Unroofing the core of the Central Andean Fold-thrust belt during the focused late Miocene exhumation; evidence from the Tipuani-Mapiri wedge-top basin, Bolivia, Basin Research, 23, 346-360, doi: 10.1111/j.1365-2117.2010.00491.x.

Mount V. S., 2014. Structural style of the Appalachian Plateau fold belt, north-central Pennsylvania, Journal of Structural Geology 69, 284-303.

Müller, J.P., J. Kley, and V. Jacobshagen, 2002. Structure and Cenozoic kinematics of the Eastern Cordillera, southern Bolivia (21°S). Tectonics 21. doi:10.1029/2001TC001340.

Murray, B. P., B. K. Horton, R. Matos, M. T. Heizler, 2010. Oligocene-Miocene basin evolution in the northern Altiplano, Bolivia: Implications for evolution of the central Andean backthrust belt and high plateau, Geologic Society of America Bulletin 122, 9/10, 1443-1462.

Ninomiya, Y., and B. Fu, 2010. Regional scale lithologic mapping in western Tibet using ASTER thrmal infrared multispectral data, International Archives of the Photogrammetry, Remote Sensing and Spatial Information Science 38, 8, 454-458.

Norton, K., and F. Schlunegger, 2011. Migrating deformation in the Central Andes from enhanced orographic rain-fall, Nature Communications 2, 584.

Oncken, O., D. Hindle, J. Kley, E. Kirsten, P. Victor, P., and K. Schemmann, 2006. Deformation of the Central Andean Upper Place System – Facts, Fiction, and Constraints for Plateau Models, *In:* The Andes Active Subduction Orogeny, O. Oncken, G. Chong, G. Franz, P. Giese, H. Gotze, V. Ramos, M. Strecker, and P. Wigger (Eds.), 3-27, Springer 2006.

Painter, C.S., B. Carrapa, P.G. DeCelles, G.E. Gehrels, and S.N Thomson, 2013, exhumation of the North American Crodillera revealed by multi-dating of Upper Jurassic-Upper Cretaceous foreland basin deposits, Geological Society of America Bulletin 126, 11/12, 1439-1464 dio:10.1130/B30999.1

Rajendran, S., and S. Nasir, 2014. ASTER spectral sensitivity of carbonate rocks – Study in Sultanate of Oman, Advances in Space Research 53, 656-673.

Robinson, D.M, N. McQuarrie, 2012, Pulsed deformation and variable slip rates within the central Himalayan thrust belt, Lithosphere 4, 5, 449-464.

Rockwell, B.W., and A.H. Hofstra, 2008. Identification of quartz and carbonate minerals across northern Nevada using ASTER thermal infrared emissivity data—Implications for geologic mapping and mineral resource investigations in well-studied and frontier areas, Geosphere 1, 2018-246

Safran, E. B., A.E. Blythe, and T. Dunne, 2006. Spatially variable exhumation rates in orogenic belts: An Andean example, Journal of Geology 114, 665-681, doi:10.1086/507613.

Scheuber, E., D. Mertmann, H. Ege, P. Silva-Gonzalez, C. Heubeck, K.-J. Reutter, V. Jacobshagen, 2006. Exhumation and basin development related to formation of the central Andean plateau, 21°S. *In*: The Andes Active Subduction Orogeny, O. Oncken, G. Chong, G. Franz, P. Giese, H. Gotze, V. Ramos, M. Strecker, and P. Wigger (Eds.), 3-27, Springer 2006.

Sempere, T., G. Herail, J. Oller, and M.G. Bonhomme, 1990. Late Oligocene–early Miocene major tectonic crisis and related basins in Bolivia. Geology 18, 946-949.

Sempere, T., 1995. Phanerozoic evolution of Bolivia and adjacent regions, *In:* Petroleum basins of South America, Edited by A.J. Tankard, S.R. Suarez, and H.J. Welsink, AAPG Memoir 62, 227-230.

Sheffels, B., 1990. Lower bound on the amount of crustal shortening in the central Bolivian Andes. Geology 18, 812–815.

Stolkmal, G. S., C. Beaumont, M. Nguyen, and B. Lee, B., 2007. Mechanics of thin-skinned fold-and-thrust belts: Insights from numerical models. *In:* Whence the Mountains? Inquiries into the Evolution of Orogenic Systems: A Volume in Honor of Raymond A. Price, Edited by W. J. Sears, T. A. Marms, and C.A. Evenchick: Geologic Society of America Special Paper 433, 63-98, doi: 10.1130/2007.2433(04).

Sobolev, S.V., and A.Y. Babeyko, 1994. Modeling of mineralogical composition, density and elastic velocities in anhydrous magmatic rocks. Surveys in Geophysics 15, 5, 515-545.

Strub, M., G. Harail, J. Darrozes, R. Garcia-Duarte, and G. Astorga, 2005. Neogene to present tectonic and orographic evolution of the Beni Subandean Zone, 6th international symposium on Andean Geodynamics, Extended Abstracts, 709-713.

Tassara, A, 2005. Interaction between the Nasca and South American Plates and formation of the Altiplano-Puna plteau: Review of a flexural anasysis along the Andean margin (15°-34°S)

Uba, C.E., C. Heubeck, C. Hulka, 2006, Evolution of the late Cenozoic Chaco foreland basin, southern Bolivian Basin Research 18, 145-170.

Ward, K. M., R.C. Porter, G. Zandt, S.L. Beck, L.S. Wagner, E. Minaya, and H. Tavera, 2013. Ambient noise tomography across the Central Andes, Geophysical Journal International, 196, 2, 1264-1265.

Watts, A. B., S.H. Lamb, J.D. Fairhcad, and J.F. Dewey, 1995. Lithospheric flexure and bending of the Central Andes, Earth and Planetary Science Letters 134, 195, 9-21.

Whipp, D.M., Jr., T.A. Ehlers, J. Braun, and C.D. Spath, 2009, Effects of exhumation kinematics and topographic evolution on detrital thermochronometer data, Journal of Geophysics Research 114, F04021, doi:10.1029/2008JF001195

Whipple, C., and N. Gasparini, 2014. Tectonic control of topography, rainfall patterns, and erosion during rapid post-12 uplift of the Bolivian Andes, Lithosphere, doi:10.1130/L325.1

Wilson, E. C., 1990. Permian Corals of Bolivia, Journal of Paleontology 64, 1, 60-78.

Yan, S., S. Menjun, Liu, F. Hong, S. Fang, 2010. Oil and Gas Accumulation in the Foreland Basins, Central and Western China, Acta Geologica Sinica (English Edition) 84, 2, 382-405. 5

Zubieta Rossetti, D., P. Baby, and J. L. Mugnier, 1996. Cenozoic evolution of the Andean foreland basin between 15°30′ and 22°00′ S, *In:* Extended abstracts, Third International Symposium on Andean Geodynamics, St. Malo, France: Paris, ORSTOM, 529-532.